NPS-PH-94-002

NAVAL POSTGRADUATE SCHOOL
MONTEREY, CALIFORNIA

AD-A276 739

THESIS
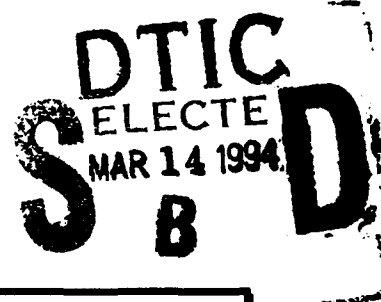
DTIC
ELECTE
MAR 14 1994
S
B
D

A TECHNIQUE FOR MULTIPLEXING 3x3-COUPLER
TERMINATED INTERFEROMETRIC FIBER-OPTIC
SENSORS

by

Gregory John Reid

December 1993

Thesis Advisors: David A. Brown
John P. Powers

Approved for public release; distribution is unlimited.

"DESTRUCTION NOTICE-Destroy by any method that will prevent disclosure of contents or reconstruction of the document."

"Prepared for: Program Executive Office, Under Sea Warfare, ASTO"

94-08200

NAVAL POSTGRADUATE SCHOOL
Monterey, California 93943

Rear Admiral T.A. Mercer   H. Shull
Superintendent   Provost

Reproduction of all or part of this report is authorized.

Released by:

P.J. MARTO
Dean of Research

REPORT DOCUMENTATION PAGE

Public reporting burden for this collection of information is estimated to average 1 hour per response, including the time for reviewing instructions, searching existing data sources, gathering and maintaining the data needed, and completing and reviewing the collection of information. Send comments regarding this burden estimate or any other aspect of this collection of information, including suggestions for reducing this burden. To Washington Headquarters Services, Directorate for Information Operations and Reports, 1215 Jefferson Davis Highway, Suite 1204, Arlington, VA 22202-4302, and to the Office of Management and Budget, Paperwork Reduction Project (0704-0188), Washington, DC 20503

1. AGENCY USE ONLY (Leave blank)	2. REPORT DATE December 1993	3. REPORT TYPE AND DATES COVERED Thesis

4. TITLE AND SUBTITLE A Technique for Multiplexing 3x3 Coupler Terminated Interferometric Fiber-Optic Sensors	5. FUNDING NUMBERS FY93 RAZDB
6. AUTHOR(S) Gregory John Reid, Lieutenant Royal Australian Navy	

7. PERFORMING ORGANIZATION NAME(S) AND ADDRESS(ES) Naval Postgraduate School Code 33 Monterey, CA 93943-5000	8. PERFORMING ORGANIZATION REPORT NUMBER NPS-PH-94-002

9. SPONSORING / MONITORING AGENCY NAME(S) AND ADDRESS(ES) Program Executive Officer ASTO-G Under Sea Warfare Office 2521 National Center Building Washington, DC 20362-5169	10. SPONSORING / MONITORING AGENCY REPORT NUMBER

11. SUPPLEMENTARY NOTES

12a. DISTRIBUTION / AVAILABILITY STATEMENT Distribution unlimited	12b. DISTRIBUTION CODE A

13. ABSTRACT (Maximum 200 words)

This thesis investigates the multiplexing of Mach-Zehnder type 3x3 terminated fiber-optic sensors demodulated by either 'quadrature' or 'symmetric' methods using intensity modulation of the source. 3x3-couplers produce signals that permit unmodulated passive demodulation of interferometric signals. The theory is described and the results of a 2x1 element array optical demonstration are presented. Possible architectures using this demultiplexing technique are presented for several applications with different return line requirements. The technique was successfully demonstrated and warrants further investigation to increase the number of sensors and reduce the number of return lines for specific applications. The multiplexing technique presents the opportunity for possible cost savings over other phase generated carrier techniques, which require wavelength modulation of the source, and significant optical path differences in the interferometers, and are therefore constrained to presently very expensive sources. The technique presented uses compatible low coherent laser sources such as Compact Disc quality (830 nm) devices.

14. SUBJECT TERMS Multiplexing, Fiber-Optic, Interferometry, Sensors, Acoustic	15. NUMBER OF PAGES 108
	16. PRICE CODE

17. SECURITY CLASSIFICATION OF REPORT UNCLASSIFIED	18. SECURITY CLASSIFICATION OF THIS PAGE UNCLASSIFIED	19. SECURITY CLASSIFICATION OF ABSTRACT UNCLASSIFIED	20. LIMITATION OF ABSTRACT UNLIMITED

NSN 7540-01-280-5500

A TECHNIQUE FOR MULTIPLEXING 3x3-COUPLER TERMINATED INTERFEROMETRIC FIBER-OPTIC SENSORS

by

Gregory John Reid
Lieutenant, Royal Australian Navy
B.E.(Electronics), University of Western Australia, 1985

Submitted in partial fulfillment of the
requirements for the degrees of

Master of Science in Engineering Acoustics
and
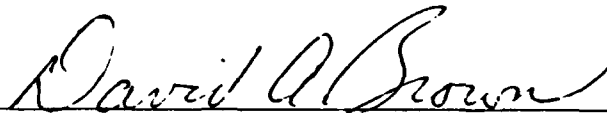**Master of Science in Electrical Engineering**

from the

NAVAL POSTGRADUATE SCHOOL
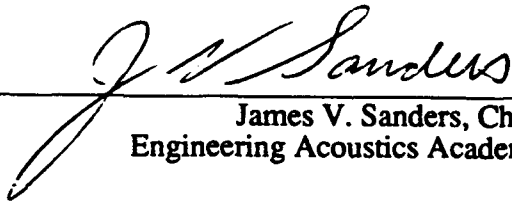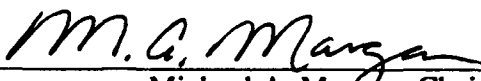December 1993

Author: _____
Gregory John Reid

Approved by: _____
David A. Brown, Thesis Advisor

_____
John P. Powers, Thesis Advisor

_____
James V. Sanders, Chairman
Engineering Acoustics Academic Committee

_____
Michael A. Morgan, Chairman
Department of Electrical and Computer Engineering

ii

ABSTRACT

This thesis investigates the multiplexing of Mach-Zehnder type 3x3 terminated fiber-optic sensors demodulated by either 'quadrature' or 'symmetric' methods using intensity modulation of the source. 3×3-couplers produce signals that permit unmodulated passive demodulation of interferometric signals. The theory is described and the results of a 2x1 element array optical demonstration are presented. Possible architectures using this demultiplexing technique are presented for several applications with different return line requirements. The technique was successfully demonstrated and warrants further investigation to increase the number of sensors and reduce the number of return lines for specific applications. The multiplexing technique presents the opportunity for possible cost savings over other phase generated carrier techniques, which require wavelength modulation of the source, and significant optical path differences in the interferometers, and are therefore constrained to presently very expensive sources. The technique presented uses compatible low coherent laser sources such as Compact Disc quality (830 nm) devices.

Accession For

NTIS GRA&I	☑
DTIC TAB	☐
Unannounced	☐
Justification

By
Distribution/
Availability Codes

| Dist | Avail and/or Special |

A-1

TABLE OF CONTENTS

TABLE OF SYMBOLS

Symbol	Definition
A	The sum of the squares of the two interfering electric fields and will be termed the dc bias value of the optical intensity.
B	Twice the product of the two interfering electric fields which reprents the amplitude of the cosinusoidally varying signal whose argument is the differential phase.optical intensity in the fiber, i.e., the maximum variation from the dc value.
C	The amplitude of the mixing sinusoidal signal.
C_n	The coupler ratio for coupler n. The coupler ratio is the power split ratio of a particular coupler as a fraction of the total input power, i.e., a percentage or equivalent fraction.
F	The number of return lines for a given array architecture.
G	Gain factor.
J_n	The Bessel function of order n.
k	The wave number in a vacuum defined as $k = 2\pi / \lambda$, where λ is the wavelength in meters unless stated otherwise.
L	The physical length of optical fiber in meters unless stated otherwise.
L_c	The coherence length of a laser, defined as the distance over which the amplitude modulation falls off to an arbitrarily determined fraction of the complete modulation value [Reference 6, page 46].
M	The number of lasers in an array of sensors.
m	The modulation index, a measure of the amount of modulation as a fraction of the total available, having a value between 0 and 1.

Symbol	Definition
N	The number of sensors per laser in an array of sensors.
n	The refractive index of a particular medium where the refractive index is defined as the ratio of the speed of light in a vacuum to the speed of light in the medium.
P	P_o denotes the output power from a particular laser. Subscripts are used to denote the power from a particular coupler in an array, e.g., P_N the power transmitted by the Nth coupler. P' denotes the power normalized to P_o.
ϕ	The differential phase shift in the arms of the interferometer. In general ϕ is a time dependent quantity, $\phi(t)$, however the time dependent notation is dropped for compactness. It is often used with various subscripts to denote the origin of the phase shift e.g., $\phi_{drift}(t)$ denotes the phase shift due to factors other than the signal of interest. ϕ_s denotes the amplitude of the sinusoidal signal of interest.
ϕ_m	The amplitude of wavelength modulation which occurs at the modulation frequency.
S	The total number of sensors for a given array.
θ, ω_s	The frequency of the phase shift in the interferometer, either in Hertz or Radians respectively.
u, v, and w	The light intensity of each of the three legs of a 3x3 terminated Mach-Zehnder interferometer. Each is phase shifted 120° relative to the other two.

ACKNOWLEDGMENTS

I would like to acknowledge several people for their assistance with this thesis. Firstly I would like to thank my principal advisor, Professor David Brown, for all his help and encouragement. His enthusiasm, experience and expertise enabled me to be able to present my thesis at the SPIE 1993 Boston conference, which was a learning experience and opportunity that I had not anticipated when embarking on this work. Many thanks must go to Professors David Gardner and Robert Keolian for their invaluable assistance in the laboratory. Their experience, expertise and willingness to give up their valuable time was especially important. I would also like to thank Professor John Powers for his technical advice and valuable assistance in the writing of this thesis. The experience and enthusiasm of these people taught me more about scientific research and writing than they will ever know. Finally I would like to thank my wife, Jane, and daughter, Elise (born January 1993), for their support and providing the overriding motivation.

I. INTRODUCTION

A. MOTIVATION

The United States Navy is seeking to take full advantage of fiber optic technology, in particular, the bringing together of fiber optic communications technology and fiber optic sensor technology. Fiber optic communications systems have many advantages over other methods of data communication. These include high bandwidth, low power consumption, security, electromagnetic interference (EMI) protection, electromagnetic pulse (EMP) protection, light weight, low loss, and low cost. Optical fiber sensors based on interferometry have been designed with high sensitivity and dynamic range. Various demodulation and multiplexing schemes are feasible for use with these interferometric sensors [References 1, 2, 3, 4, and 5]. For example it has been demonstrated that 3x3-coupler terminated interferometric sensors with quadrature [Reference 6] and 'symmetric' demodulation yield particular advantages [References 7, 8, and 9]. An array of these optical fiber sensors in an optical architecture has the potential to accommodate both the benefits of the interferometric sensors and optical communications systems. An all-optical system removes the need for outboard electronics and thus has the potential for great weight and cost savings. Such an optical system using 3x3 couplers and 'symmetric' demodulation is demonstrated in this thesis.

B. GOAL

This thesis demonstrates that the use of 3x3-coupler terminated interferometric sensors and either quadrature or 'symmetric' demodulation enables the use of amplitude

modulation (AM) frequency-division-multiplexing (FDM) techniques where the laser intensity is the quantity that is amplitude modulated.

The theory and performance of such a multiplexing scheme is investigated with sensor demonstrations using both analog electronics and optical fiber interferometric sensors. On the basis of this research a design for an array of M x N sensors is presented which may provide large cost savings with improved system performance.

C. BACKGROUND

1. Interferometric Sensors

Interferometry is a technique used to measure differential phase shifts. The optical phase delay generated in a physical length of fiber L is:

$$\phi = knL, \tag{1.1}$$

where n is the refractive index of the fiber core and k is the wave number in a vacuum ($k = 2\pi/\lambda$). Neglecting birefringence from the two orthogonal polarizations supported by the fiber, the fractional variation in phase can be expressed as:

$$\frac{d\phi}{\phi} = \frac{dk}{k} + \frac{dn}{n} + \frac{dL}{L}, \tag{1.2}$$

where the changes in n and L are related to a particular measurand (e.g., pressure, temperature, magnetic field, or other environmental changes).

Various techniques have been demonstrated to selectively enhance the change in phase in the fiber for a particular measurand (e.g., acoustic waves), while reducing changes in phase due to unwanted effects (e.g., acceleration). Mach-Zehnder interferometric sensors use two-beam interferometry as illustrated in Figure 1.1. It has been shown that by using both legs as signal legs, in push-pull configurations, improved

2

sensitivity and, through design, highly favorable properties (e.g., acceleration canceling) can be obtained.
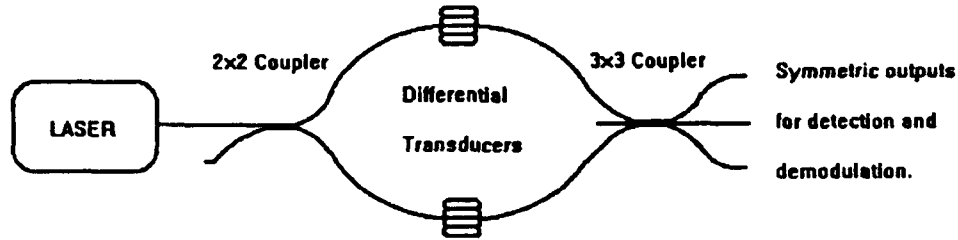

Figure 1.1. Schematic diagram of a Fiber Optic Mach-Zehnder Interferometric Sensor

An ideal 3x3-coupler provides three signals of equal amplitude, each with a relative phase difference of 120°. The intensities of each output leg of the 3 x 3-coupler are:

$$u = A + B\cos\left[\phi(t) + \phi_{drift}(t)\right],\qquad(1.3)$$

$$v = A + B\cos\left[\phi(t) + \phi_{drift}(t) + 120°\right],\qquad(1.4)$$

$$w = A + B\cos\left[\phi(t) + \phi_{drift}(t) - 120°\right],\qquad(1.5)$$

where A is the value of optical intensity from the fibers (analogous to a dc offset), B is the peak value of the intensity and $\phi_{drift}(t)$ is the static phase shift resulting from the difference in optical path length between the two signal legs. This quasi-static (or slowly varying compared to the signal of interest) phase also includes the phase shift due to environmental effects (hydrostatic pressure, temperature, etc.) as well as the physical difference in the length of the legs. Examples of these types of signals are shown in Appendix A. The signal of interest $\phi(t)$ is assumed to be of the form;

$$\phi(t) = \phi_s \sin(\omega_s t).$$ (1 6)

Using the trigonometric identity:

$$\cos(\alpha + \beta) = \cos(\alpha)\cos(\beta) + \sin(\alpha)\sin(\beta),$$ (1.7)

the intensity, equation (1.3), can be rewritten as:

$$u = A + B\cos\left[\phi_s \sin(\omega_s t)\right]\cos\left[\phi_{drift}(t) + \phi_c\right]$$
$$- B\sin\left[\phi_s \sin(\omega_s t)\right]\sin\left[\phi_{drift}(t) + \phi_c\right].$$ (1.8)

Similar expressions for v and w with phase shifts of $\pm120°$, as appropriate, also can be written. This equation is of the form of a Bessel function generating function. The generating function and associated series from Reference 10 (page 361, equations 9.1.42 and 9.1.43) are reproduced below:

$$\cos(z \sin \theta) = J_0(z) + 2\sum_{k=1}^{\infty} J_{2k}(z) \cos(2k\theta)$$ (1.9)

$$\sin(z \sin \theta) = 2\sum_{k=0}^{\infty} J_{2k+1}(z) \sin\left[(2k+1)\theta\right].$$ (1.10)

The intensity, equation (6), can therefore be written as a series of Bessel weighted sine and cosine functions as follows:

$$u = A + B\cos(\phi_{drift}(t))\left[J_0(\phi_s) + 2\sum_{k=1}^{\infty} J_{2k}(\phi_s)\cos(2k\omega_s t)\right]$$
$$- E\sin(\phi_{drift}(t))\left[2\sum_{k=0}^{\infty} J_{2k+1}(\phi_s)\sin\left[(2k+1)\omega_s t\right]\right].$$ (1.11)

Thus the frequency spectrum consists of components at multiples of ω_S which are in turn weighted by Bessel function terms and the drift term, $B\cos(\phi_{drift}(t))$. Appendix A plots

4

the lower order Bessel functions and the frequency spectrum of Equation 1.11 for typical $\phi(t)$ and $\phi_{drift}(t)$.

2. Symmetric Demodulation

The technique of symmetrically demodulating the outputs was developed by Professor Robert M. Keolian of Naval Postgraduate School and is detailed in References 7, 8, and 9. A schematic of the scheme is shown in Figure 1.2. Modifications and performance specifications of the symmetric analog demodulator of Reference 9 are detailed in Appendix B.
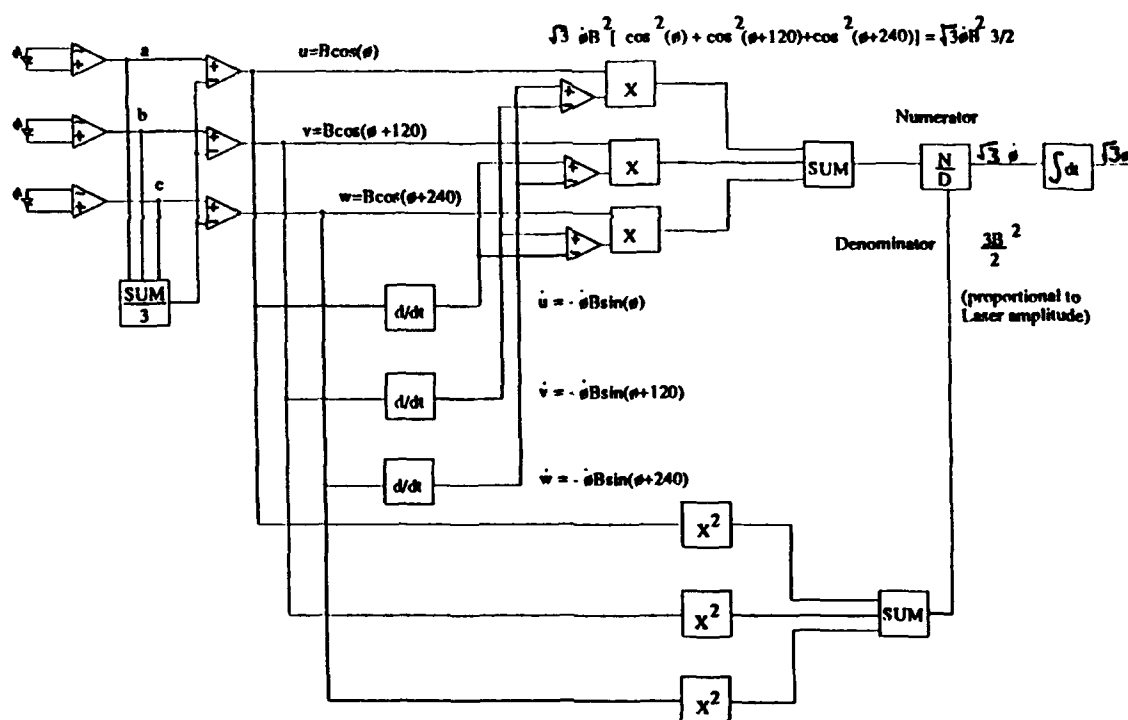

Figure 1.2. Passive Symmetric Demodulation Scheme (adapted from Reference 8).

The demodulation scheme is based upon the following expression:

$$\phi(t) \quad \propto \quad \int \frac{u(\dot{v} - \dot{w}) + v(\dot{w} - \dot{u}) + w(\dot{u} - \dot{v})}{(u^2 + v^2 + w^2)} \, dt, \qquad (1.12)$$

where $\phi(t)$ is the signal of interest to be recovered and the dots above a variable indicate a time derivative. The implementation detailed in Reference 9 is outlined below for continuity.

The output intensity of each leg of the interferometer is as previously defined:

$$u \quad = \quad A \quad + \quad B\cos\left[\phi(t) + \phi_{drift}(t)\right], \qquad (1.13)$$

with similar expressions for v and w. After photodetection and amplification by low-noise transimpedance amplifiers, the symmetric voltages are added together and scaled by a factor of $-1/3$ to produce $-A$. This average dc content signal is then summed to each of the symmetric, interferometric voltage signals to remove the average dc component, A. These interferometric signals, with the average dc component removed are denoted again by u, v, and w, where

$$u \quad = \quad B\cos\left[\phi(t) + \phi_{drift}(t)\right]$$
$$v \quad = \quad B\cos\left[\phi(t) + \phi_{drift}(t) + 120°\right] \qquad (1.14)$$
$$w \quad = \quad B\cos\left[\phi(t) + \phi_{drift}(t) - 120°\right].$$

These three symmetric interferometric signals are cross multiplied by the difference of the 'complimentary' derivatives to yield:

$$u(\dot{v}-\dot{w}) = B\cos(\phi)\left[B\dot{\phi}\sin(\phi-120°)+B\dot{\phi}\sin(\phi+120°)\right]$$

$$v(\dot{w}-\dot{u}) = B\cos(\phi-120°)\left[B\dot{\phi}\sin(\phi+120°)+B\dot{\phi}\sin(\phi)\right] \qquad (1.15)$$

$$w(\dot{u}-\dot{v}) = B\cos(\phi-120°)\left[B\dot{\phi}\sin(\phi+120°)+B\dot{\phi}\sin(\phi)\right].$$

It can be shown by trigonometric identities or with phasor diagrams that the first equation of (1.16) can be simplified to:

$$u(\dot{v}-\dot{w}) = \sqrt{3}B^2\dot{\phi}\cos^2(\phi). \qquad (1.16)$$

By noting:

$$\cos^2(x)+\cos^2(x+120°)+\cos^2(x-120°) = \tfrac{3}{2}, \qquad (1.17)$$

the sum of the three equations in (1.16) can be shown to result in:

$$\dot{\phi}B^2\left[\cos^2(\phi)+\cos^2(\phi+120°)+\cos^2(\phi-120°)\right] = \tfrac{3}{2}\sqrt{3}B^2\dot{\phi}. \qquad (1.18)$$

The factor of B^2 varies as a function of laser intensity, temperature, and the polarization angle of the light in the fiber. This dependence is removed by summing the squares of each of the interferometric signals (with the dc component removed), resulting in:

$$u^2+v^2+w^2 = \tfrac{3}{2}B^2, \qquad (1.19)$$

and using this result as a normalizing division factor, the ratio of Equation 1.18 to Equation 1.19 is then integrated to produce $\phi(t)$.

Unity scale factors have been assumed on all the operators (summers, dividers, etc.) in presenting the demodulation technique.

Following on from the background of interferometry and demodulation, the theory and demonstration of multiplexing interferometric sensors using intensity modulation of the source is introduced.

II. MULTIPLEXING OF INTERFEROMETRIC SENSORS

The proposed multiplexing scheme uses 'Optical Fiber Subcarrier Multiplexing' (OSCUM) [Reference 1, pages 544-5, and Reference 3, pages 167-8] although this approach has not previously been demonstrated with interferometric sensors. Reference 2 (section 4.5, pages 167-8) details the use of this multiplexing technique with intensity sensors.

A. THEORY

The theory will be presented using Figure 2.1 and applying subscripts to the equations which relate to the numbered 'position' in the Block Diagram.
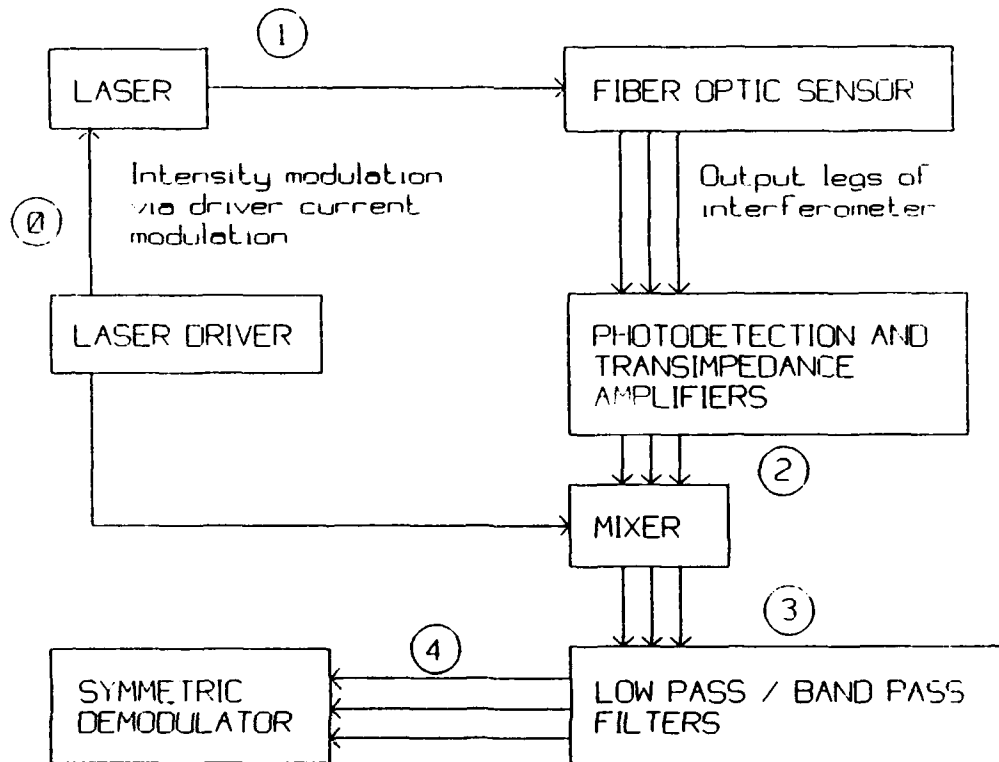

Figure 2.1. Multiplexing/Demultiplexing Block Diagram: Circled numbers relate to subscripts in Equations 2.1 - 2.9.

The laser is driven with an AM modulation current given as:

$$A_0(t) = A_0[1 + m\sin(\omega_m t)],$$ (2.1)

and the resulting light intensity from the laser $I_1(t)$ is then:

$$A_1(t) = A_1[1 + m\sin(\omega_m t)].$$ (2.2)

The electrical signal from the output of the sensor, at point 2, is then given as:

$$
\begin{aligned}
I_2(t) &= [A + B\cos(\phi)][1 + m\sin(\omega_m t)] \\
&= A + B\cos(\phi) + mA\sin(\omega_m t) + mB\cos(\phi)\sin(\omega_m t),
\end{aligned}
$$ (2.3)

where the notation of Reference 11 has been used. Here ϕ denotes our signal of interest and includes the drift and coupler terms, given as:

$$\phi = \phi(t) + \phi_{drift}(t) + \phi_c = \phi_s \sin(\omega_s t) + \phi_{drift}(t) + l(120°),$$ (2.4)

where $l = 0, +1,$ or -1. Using the trigonometric identity:

$$\sin(\alpha)\cos(\beta) = \tfrac{1}{2}\sin(\alpha - \beta) + \tfrac{1}{2}\sin(\alpha + \beta),$$ (2.5)

the signal at point 2 can then be rewritten as:

$$v_2(t) = A + B\cos(\phi) + mA\sin(\omega_m t) + \frac{mB}{2}[\sin(\omega_m t - \phi) + \sin(\omega_m t + \phi)],$$ (2.6)

where the gain as a result of the transimpedance amplifier and fiber losses are all encompassed in the amplitudes of each term. An example of a computer generated spectrum of the signal represented by Equation 2.6 is shown in Figure 2.2. The peak signal phase modulation $\phi_S = \pi$ radians, the drift phase term is zero, the signal frequency is 1 kHz and the modulation frequency is 30 kHz, and the intensity modulation depth $m = 0.75$. Figure 2.2 clearly shows the baseband and modulated portions of the signal.
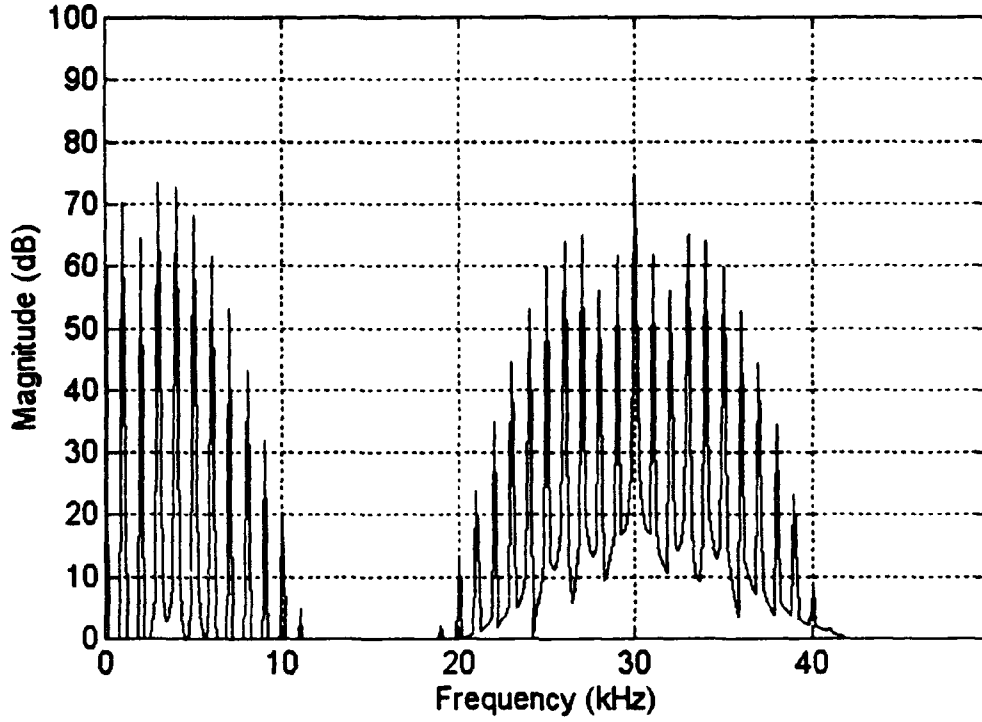
10

Figure 2.2. Frequency spectrum of an interferometric output phase modulated π radians peak, at 1 kHz, and amplitude modulated at 30 kHz.

The signal $v_2(t)$, given by Equation 2.6, is now mixed with a scaled voltage proportional to the laser drive current modulating signal. This mixing signal has no dc term and is defined as:

$$v_0(t) = C \sin(\omega_m t). \tag{2.7}$$

Thus the signal at point 3 becomes:

$$v_3(t) = AC \sin(\omega_m t) + BC \sin(\omega_m t) \cos(\phi)$$
$$+ mAC \sin^2(\omega_m t) + mBC \sin^2(\omega_m t) \cos(\phi), \tag{2.8}$$

which can be rewritten as:

11

$$v_3(t) = \frac{mAC}{2} + \frac{mBC}{2}\cos(\phi)$$
$$+ AC\sin(\omega_m t) + \frac{BC}{2}\left[\sin(\omega_m t + \phi) + \sin(\omega_m t - \phi)\right] \qquad (2.9)$$
$$+ \frac{mAC}{2}\cos(2\omega_m t) + \frac{mBC}{4}\left[\cos(2\omega_m t - \phi) + \cos(2\omega_m t + \phi)\right],$$

where the top and bottom lines of Equation 2.9 represent the modulated portion of Equation 2.6 (or Figure 2.2) frequency translated to baseband and twice the carrier frequency, respectively. The second line of Equation 2.9 represents the baseband portion of Equation 2.6 (or Figure 2.2) translated to the carrier frequency. Using our previous example (Figure 2.2) and mixing with a signal of frequency of 30 kHz ($C = 1$ from Equation 2.7), the spectrum shown in Figure 2.3 is obtained. Figure 2.3 clearly shows the translation caused by mixing and how subsequent recovery of our signal of interest by low pass filtering can be achieved. It will be shown later that this mixing or heterodyning is necessary because the modulated signals will overlap in the baseband, precluding their recovery by simple filtering.

The other two legs (relatively phase shifted by 120° from each other) are similarly mixed and filtered and can then be demodulated using the passive symmetric demodulation scheme previously described.
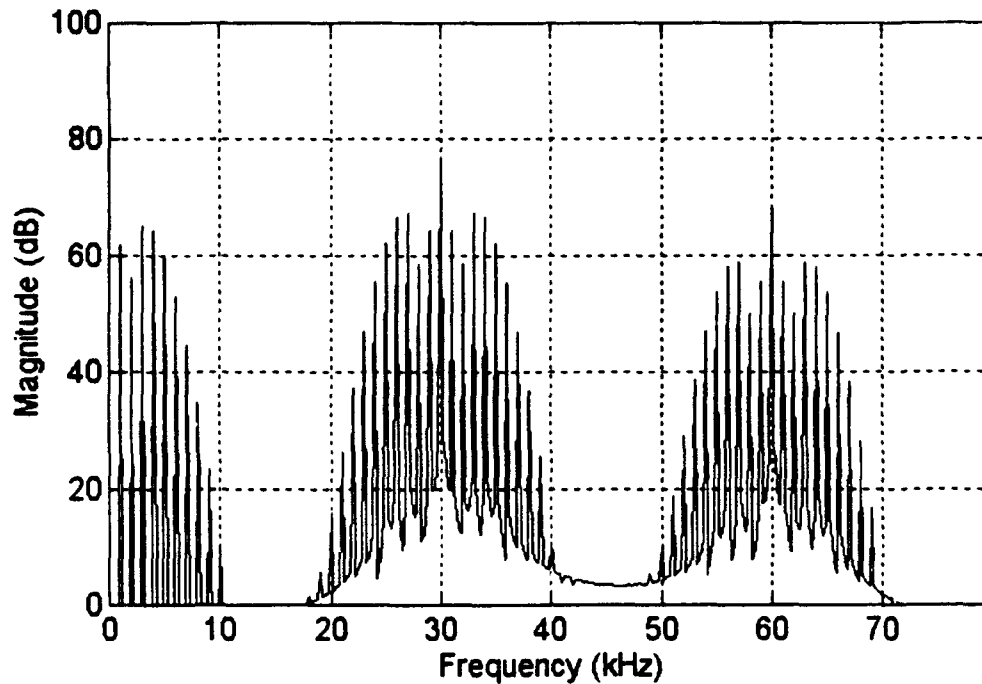
Figure 2.3. Spectrum of signal of Figure 2.2 mixed with a signal, phase and frequency locked to the laser modulating signal at 30 kHz.

B. DEMONSTRATION WITH OPTICAL SYSTEM

It was verified that the ratio of components in the baseband was the same as the modulated band (neglecting the DC and carrier components) by use of an analog electronic simulation of the optical components and signals. This indicated that the static phasing ϕ_c would be preferred with this approach. Appendix C describes this demonstration and contains all the significant results obtained. The essential result of the demonstration was the verification of the computer generated simulation of Figure 2.2. Once this demonstration was successfully completed, a two-laser, two-sensor optical demonstration was tested; the schematic is shown in Figure 2.4. Two lasers are amplitude modulated at two different frequencies f_{m1} and f_{m2}, respectively. The two sensors

13

interrogated by these lasers are then coupled together before photodetection, demultiplexing, filtering and demodulation.
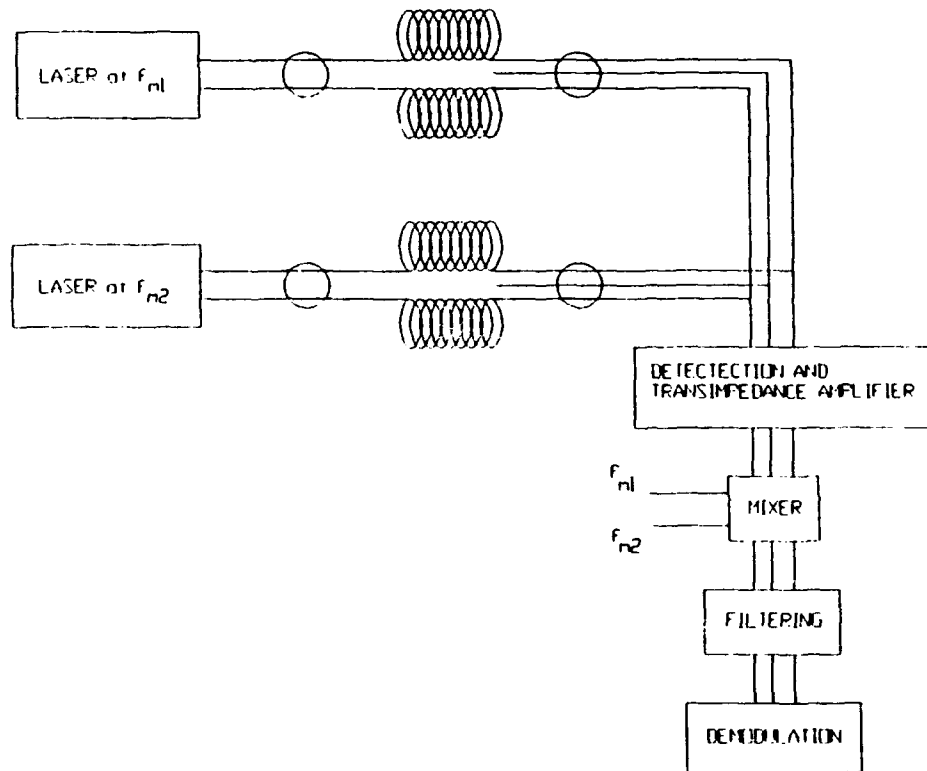

Figure 2.4. Schematic for Optical Demonstration.

A computer simulation example of two sensor signals and two modulation (subcarrier) frequencies is shown in Figures 2.5 and 2.6. They follow directly from the derivation of the previous section but highlight the potential for overlap of sideband

signals and the heterodyning technique used to recover the signal of interest. This example represents the multiplexing and demultiplexing of the interferometric signals from one of the three legs shown in Figure 2.4. Figure 2.5 shows two modulated interferometric signals with the following characteristics: subcarrier modulation frequency f_{m1} = 40 kHz, sensor signal amplitude ϕ_{s1} = 1.5π radians, sensor signal frequency f_{s1} = 1 kHz, bias angle ϕ_{d1} = 45°, and f_{m2} = 60 kHz, ϕ_{s2} = π radians, f_{s2} = 600 Hz, ϕ_{d2} = 0°. The amplitudes and bias angles of the two sensor signals were specifically chosen to be different to highlight the overlap at baseband.
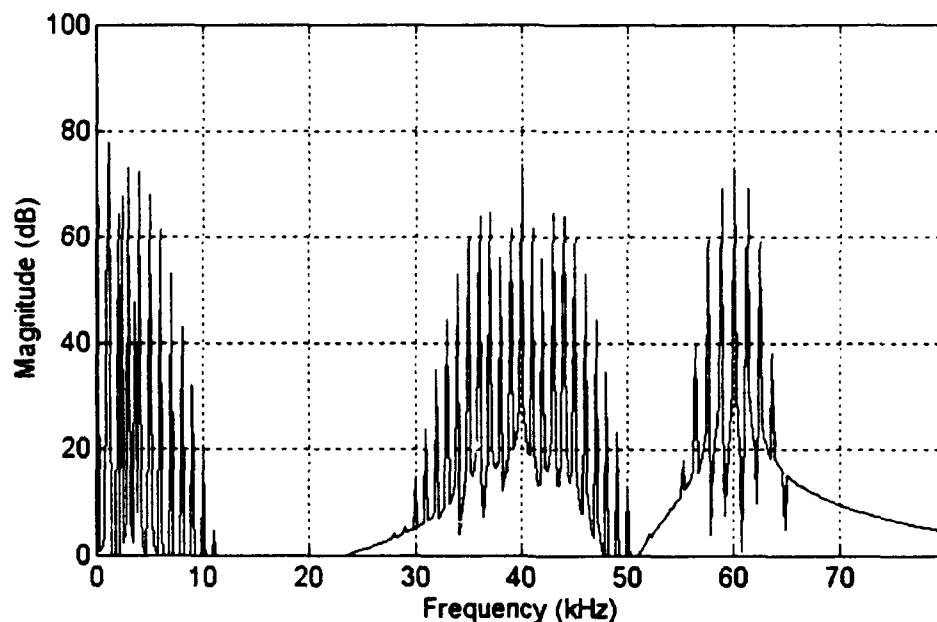

Figure 2.5. Example of two modulated interferometric signals.

Figure 2.6 shows the signal of Figure 2.5 after heterodyning with modulating signal at frequency f_{m1}. The overlapped baseband signals have been translated to f_{m1} (40 kHz) and the interferometric signals of interest can be recovered by lowpass and bandpass filtering. The recovered interferometric signals from each of the three legs can then be demodulated. The filtering must provide the same phase response to each of the three legs

15

(ideally constant over the frequency range of interest) so that the interferometric signals can be accurately demodulated.
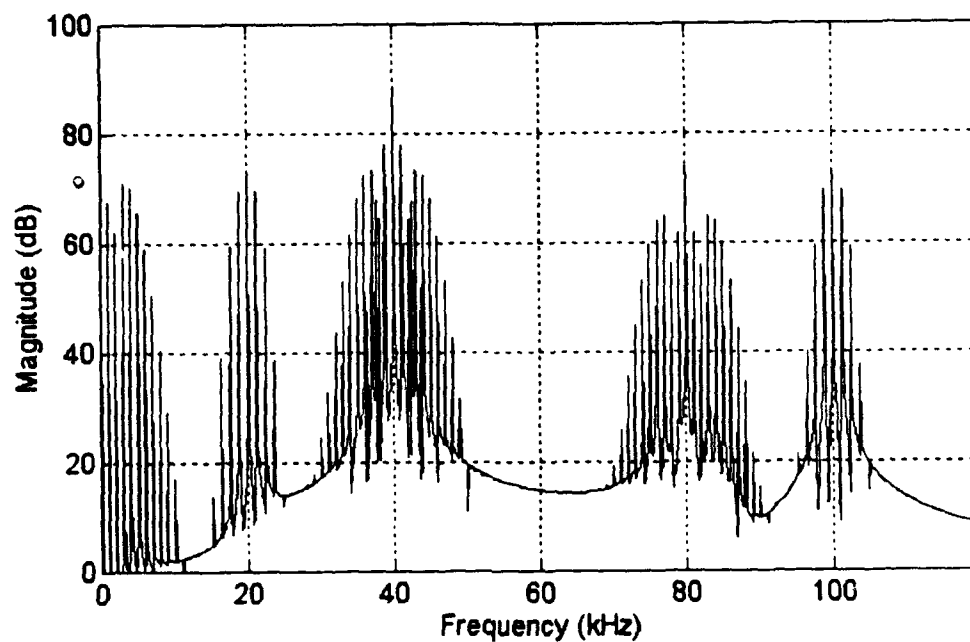

Figure 2.6. Signal represented in Figure 2.5 heterodyned with modulating signal at frequency f_{m1} (40 kHz).

1. Experimental Setup

The equipment setup for the optical demonstration is shown in Figure 2.7.
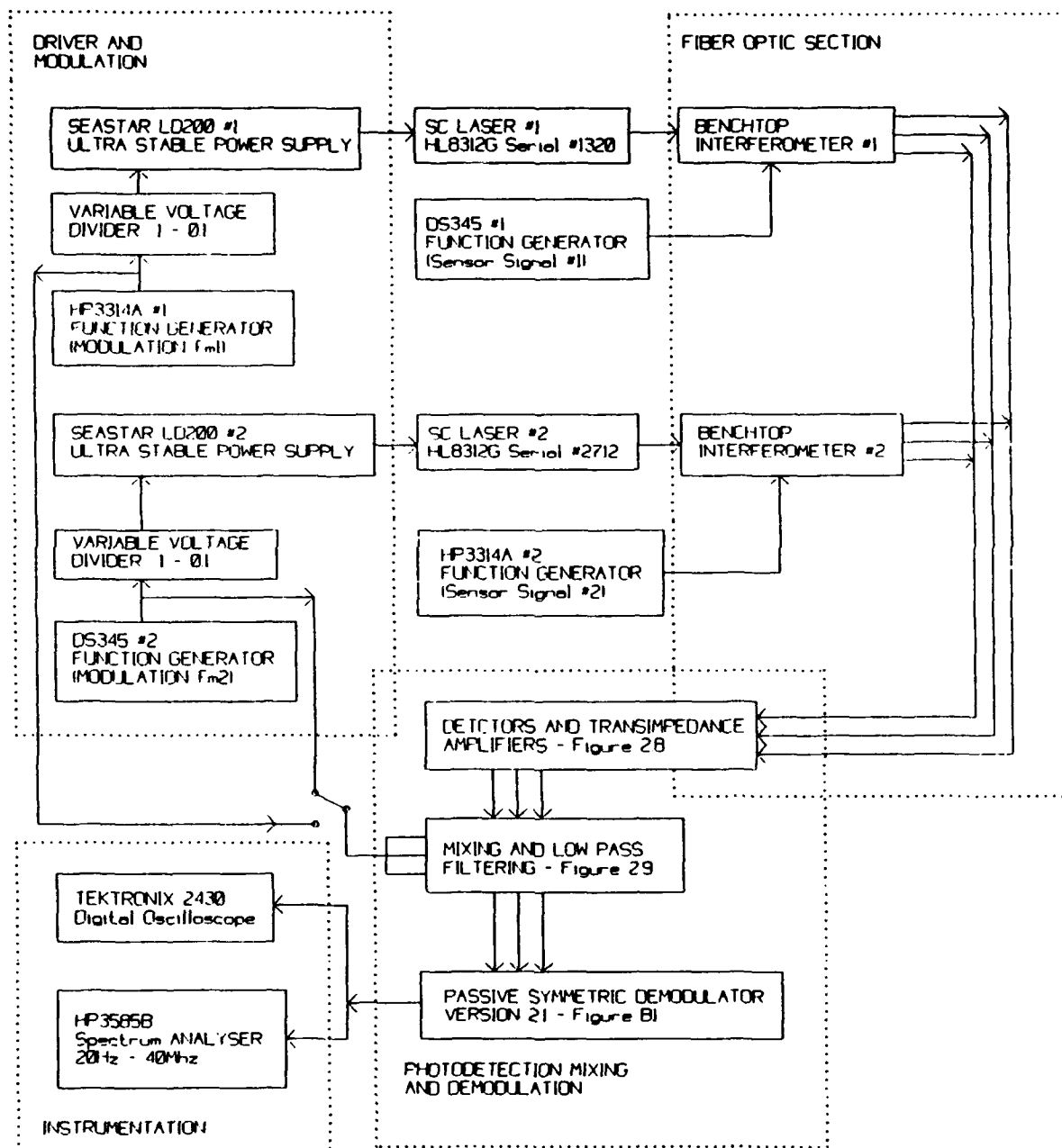

Figure 2.7. Optical Demonstration Experimental Setup.

The driver and modulation section uses the Seastar LD200 Ultra Stable Power Supply to drive the semiconductor lasers. This driver can modulate the intensity up to a frequency of about 1 MHz. The optical power output starts to drop off at about 800 kHz. The variable voltage divider in Figure 2.7 is required because of the conflicting requirements of the AD633 multiplier and the external modulation input of the LD200. The external modulation input of the LD200 converts a voltage input to a laser drive current output. The ratio of the driving voltage to resulting drive current is 10 mV to 1 mA [Reference 12]. Thus a voltage of the order of 50 to 100 mV$_{pp}$ is required to provide the required drive current modulation levels. The AD633 multiplier chip, on the other hand, prefers to see the largest signal possible (up to 10 V); so, by use of the divider, a phase matched signal can be simultaneously provided to the LD200 (50-100 mV$_{pp}$) and the AD633 (10 V$_{pp}$).

Figure 2.8 shows the detection, transimpedance amplifier, and amplification for one of the three legs. The two gain stages are included to amplify the signal before mixing so that a reasonable level signal (comparable to the laser modulating signal) is seen by the multiplier in the mixing stage. The amplifiers remove the DC component of the signal and each provide a noninverted gain of 20. The 20 kΩ resistor in the amplifier input path is required to provide a return to ground for the very small input current [Reference 14, section 3.05, page 95]. The noise up to this stage and introduced by the amplification will also be amplified, i.e., there will be no increase in signal to noise ratio (SNR). This was not considered an issue in this demonstration of the multiplexing technique but would have to be addressed in an actual sensor system demonstration.

Figure 2.9 shows the mixing and low pass filtering circuit where THB292 is an active filter integrated into a single package [Reference 13, page 118] with a 3 dB cutoff at 22 kHz. The filter has a frequency response as shown at Appendix D. This low cost

18

integrated package ($12.85 each) was chosen to simplify the implementation. In a practical system the cutoff required may well be far greater than 22 kHz. A rule of thumb, developed by Dr. David A. Brown and extensively verified by experience, gives the interferometric signal bandwidth as a function of signal frequency and amplitude as:

$$f_{sb} = 5\phi_s f_s, \qquad (2.10)$$

where the subscript sb denotes *significant bandwidth*. This estimate is considered conservative but, nevertheless, provides a reasonable estimate of the maximum frequency, signal level, or combination of both that can be demodulated by the system if we designate the cutoff frequency of the low pass filter as f_{sb}.
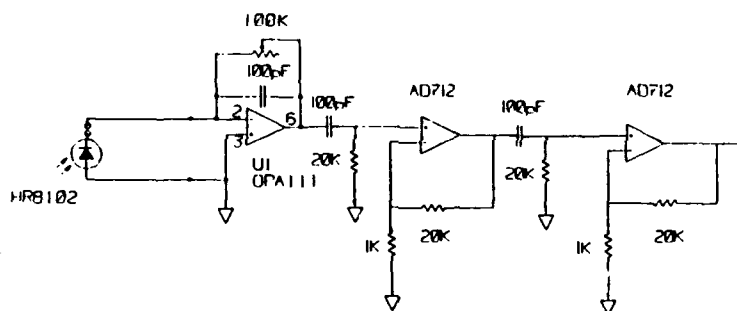

Figure 2.8 Detection and Transimpedance Amplifier Stage.

For example, a system with a dynamic range of 100 dB at 20 kHz with an assumed minimum detectable signal of 5 μrad/$\sqrt{Hz}$ and a maximum of 4% THD (a typical value using Demodulator Version 2.1 [Appendix B]) would tolerate a maximum signal calculated as follows:

$$20\log\left(\frac{\phi_s \ \mu\text{rad} / \sqrt{\text{Hz}}}{5 \ \mu\text{rad} / \sqrt{\text{Hz}}}\right) = 100 \ \text{dB re 1mrad} / \sqrt{\text{Hz}} \text{ at 20 kHz} \tag{2.11}$$

$$\phi_s = 0.5 \ \text{rad},$$

and a lowpass filter cutoff above f_{sb} :

$$f_{sb} = 5 \times 0.5 \times 20 \times 10^3 = 60 \ \text{kHz}. \tag{2.12}$$

This cutoff frequency then allows for a maximum signal at 100 Hz, and a maximum of 4% THD, of:

$$\phi_s = \frac{f_{sb}}{5f_s} = \frac{50 \times 10^3}{500} = 100 \ \text{radians}, \tag{2.13}$$

or a dynamic range of:

$$\frac{100}{5 \times 10^{-6}} = 20 \times 10^{-6} = 146 \ \text{dB re } 1\mu\text{rad} / \sqrt{\text{Hz}} \text{ at 100 Hz}, \tag{2.14}$$

assuming the same noise floor.

The benchtop interferometers of Figure 2.7 are described in detail at Reference 9, pages 60-66 (see also Appendix D). The purpose of the benchtop interferometer is to provide a signal from a push-pull optical sensor that can be easily adjusted by a function generator connected to the benchtop interferometer. The three outputs of the circuit of Figure 2.9 are connected to the 9207 resistor of the analog symmetric demodulator, version 2.1, described in detail in Appendix B. This allows the transimpedance amplifier of the demodulator to be reconfigured as a voltage amplifier and saves having to rewire or reconstruct the demodulator front end, depending on whether or not the demodulator is being used with the demultiplexing scheme or the direct demodulation of interferometric

20

sensor signals. This stage of amplification is still used to ensure that the three signals have the same ac amplitude, just as in the direct demodulation configuration [Appendix B].
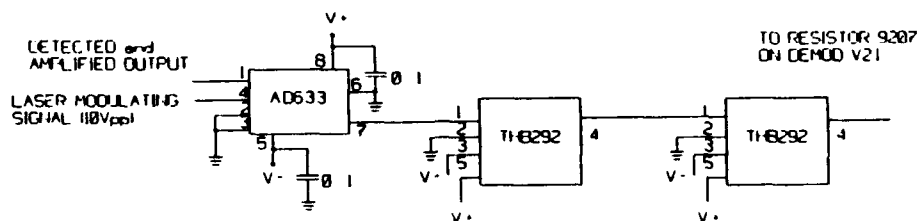

Figure 2.9. Circuit of the mixing and low pass filtering stage of Figure 2.7.

2. Results

Prior to coupling the two benchtop interferometers together, each was tested separately. A modulation signal was applied to the appropriate laser and then the sensor signal was demultiplexed and demodulated. Figures 2.10 and 2.11 show the demultiplexed demodulated outputs for inputs to both channels prior to coupling together.

CH1_   IV AC   BWL   A 200us -577mV EXT1
CH2_   IV AC

CH1gnd —

CH2gnd —

CHI

CH2
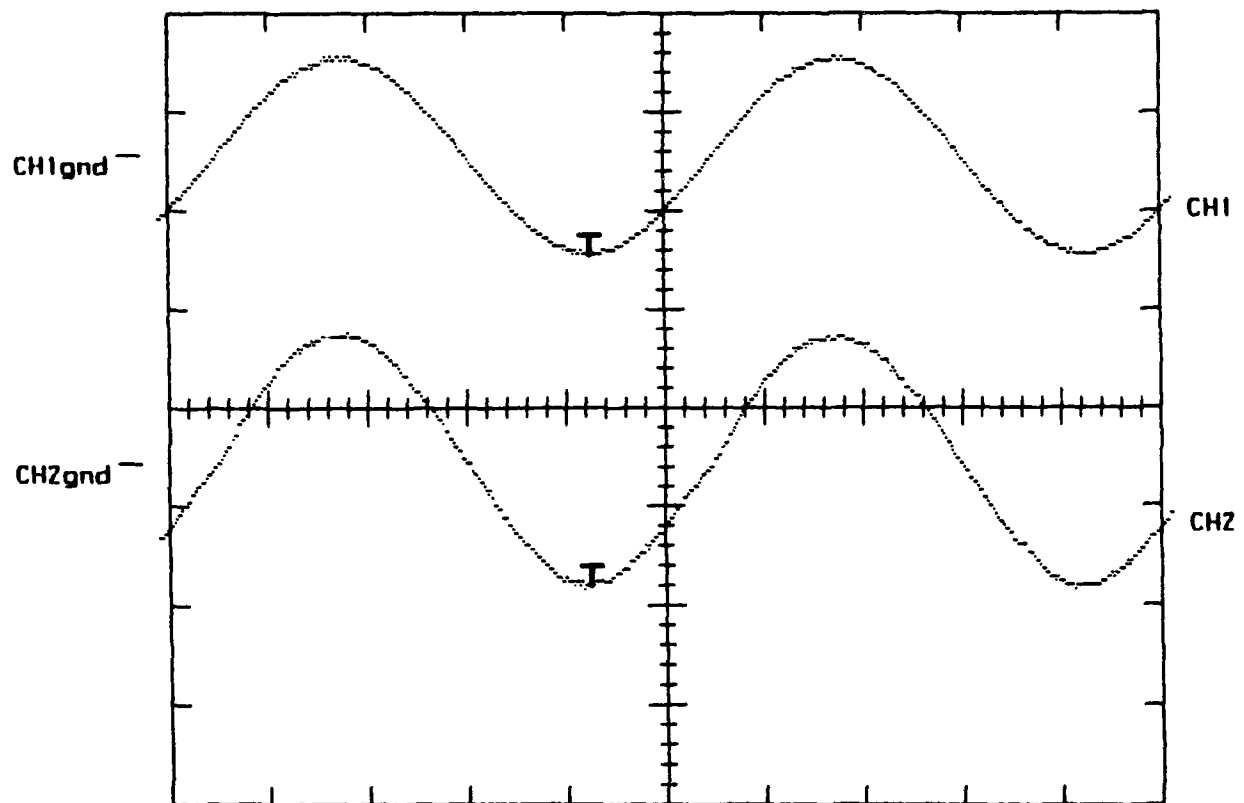
200 μsec/div.

Figure 2.10. The upper signal represents the input to benchtop interferometer #1
(ϕ_{s1} = π radians amplitude) while the lower signal represents the
demultiplexed/demodulated output (f_{m1} = 80 kHz).

CHI_ 2V AC BWL A 500us -577mV EXT1
CH2 2V AC

CHI gnd —

CH2 gnd —

CHI

CH2
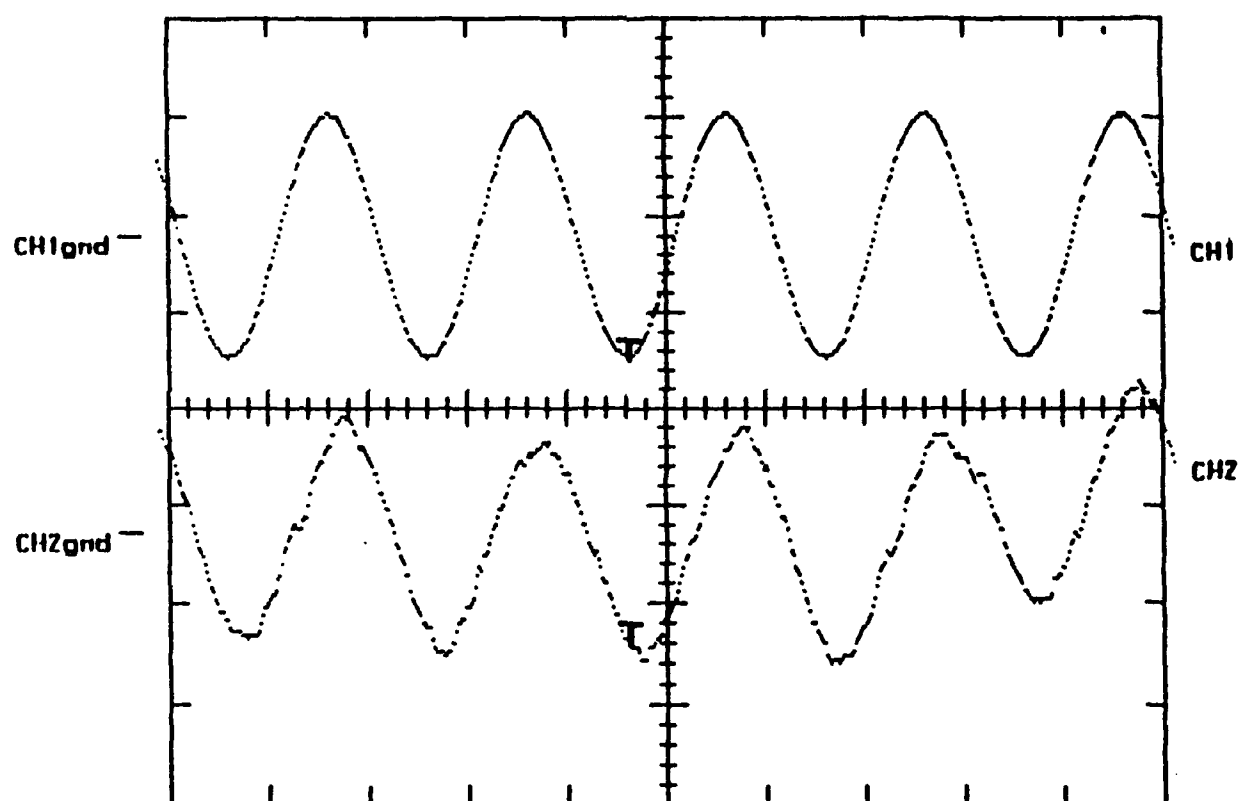
500 µsec/div.

Figure 2.11. Upper signal represents the input to benchtop interferometer #2
(ϕ_{s2} = 2.5 π radians amplitude) while the lower signal represents the
demultiplexed/demodulated output (f_{m2} = 120 kHz).

23

After connecting the two benchtop interferometers, with a 50/50 coupler, the simulated acoustic signals for each interferometer were again demultiplexed and demodulated. The outputs for two different inputs to each of the benchtop interferometers are shown in Figures 2.12 and 2.13.

CH1   2V AC   FUL   A 500us   -577mV   EXT1
CH2   2V AC

500 μsec/div.

Figure 2.12. Interferometers 1 and 2 coupled together. The upper signal represents the input to benchtop interferometer #1 (ϕ_{s1} = 2.5 π radians amplitude) while the lower signal represents the demultiplexed/demodulated output (f_{m1} = 80 kHz).
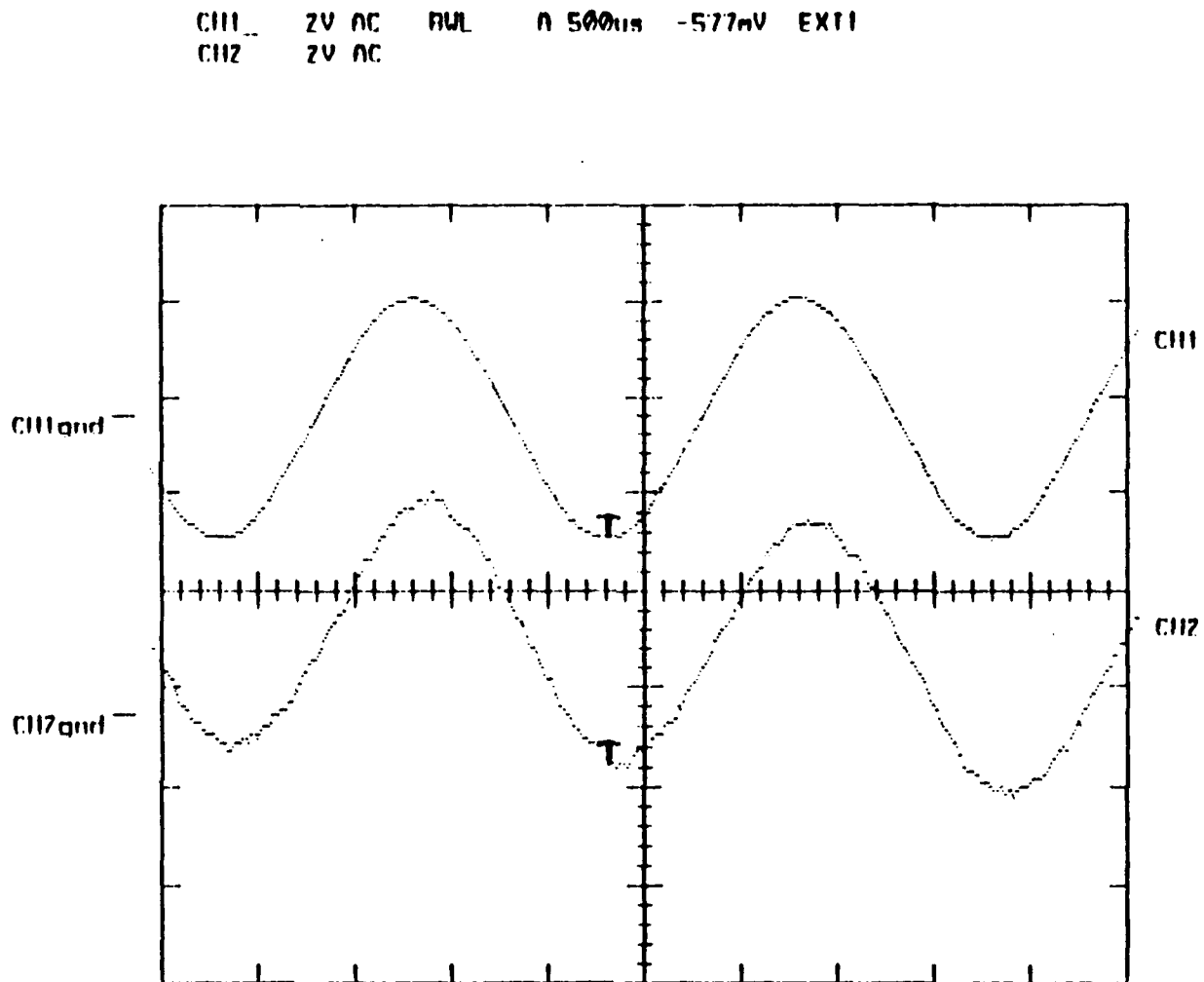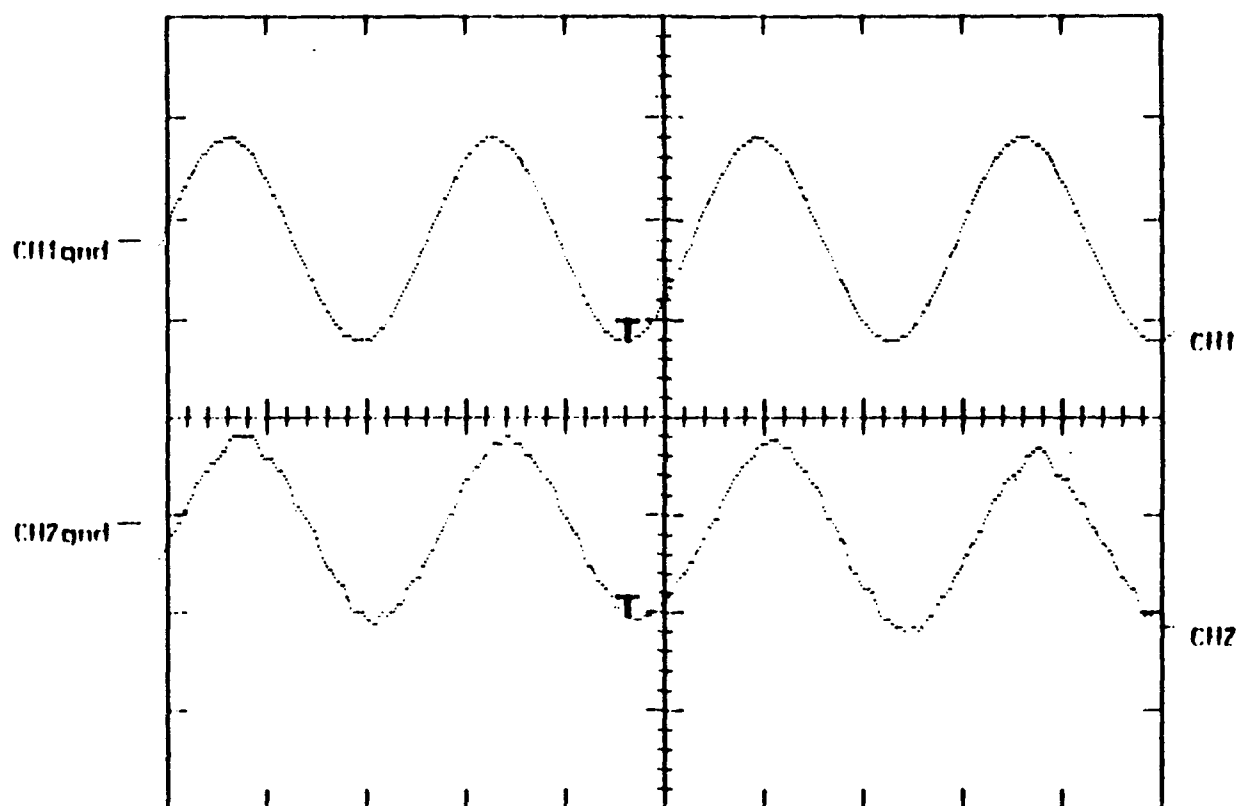
24

CH1   2V DC   BWL   A 500min   -577mV7 EXT1
CH2   2V DC

CH1 gnd —

                                                              CH1

CH2 gnd —

                                                              CH2

500 μsec/div.

Figure 2.13. Interferometers 1 and 2 coupled together. The upper signal represents the input to benchtop interferometer #2 ($\phi_{s2} = 2\pi$ radians amplitude) while the lower signal the demultiplexed/demodulated output ($f_{m2} = 120$ kHz).

25

Figure 2.14 shows the demultiplexed and demodulated output for a triangular wave benchtop interferometer input (2.5 V at ~1350 Hz). Even though the frequency spectrum of triangle wave has numerous components above its fundamental (1350 Hz) and the low pass filter cutoff frequency is 22 kHz, the demodulator is able to demodulate the band-limited demultiplexed system. This figure was chosen to highlight the robustness but ultimate limitations of the technique.

CHI_   IV nC   BWL   n 500us   -577mV   EXT1
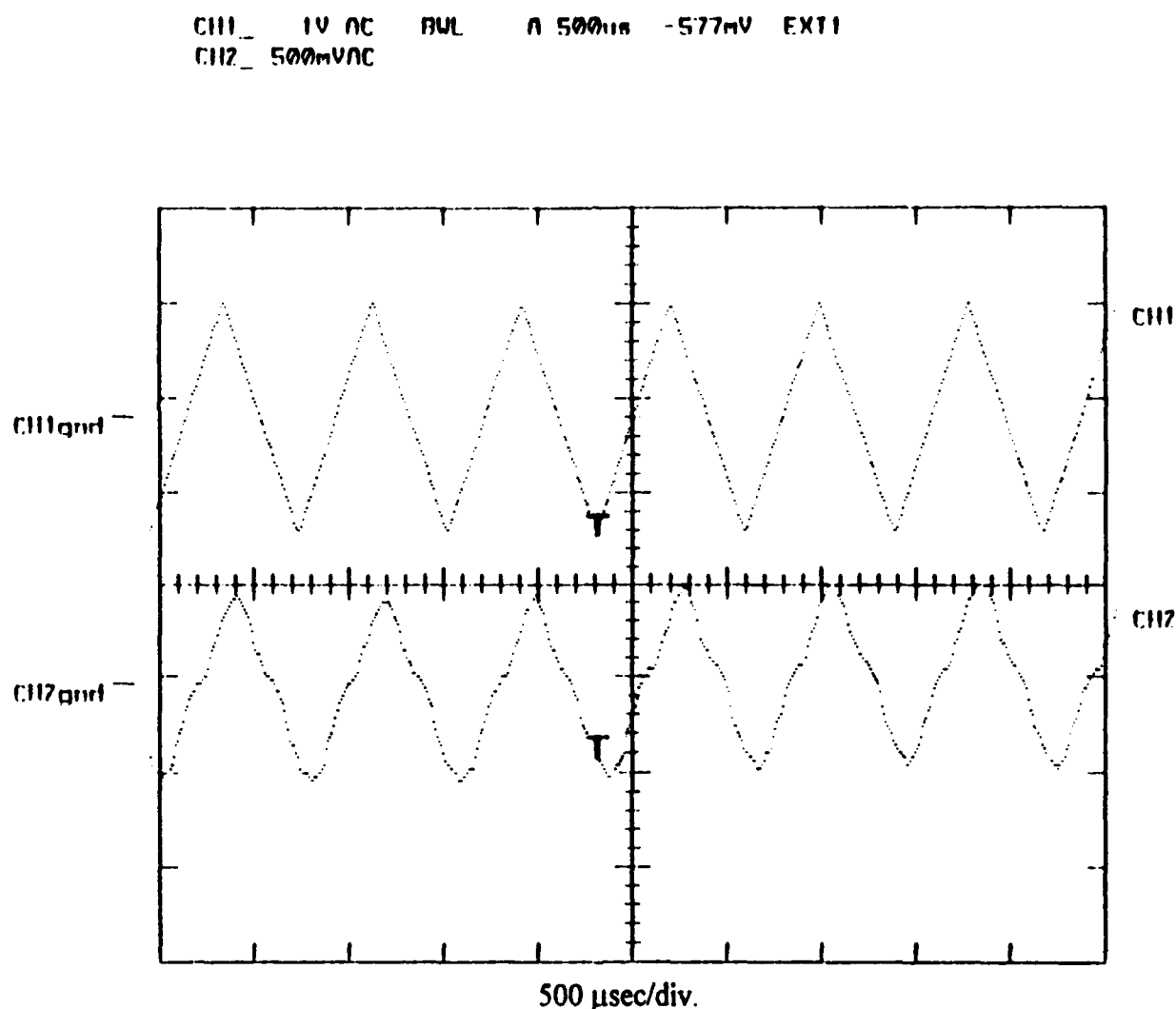CH2_ 500mVnC

500 μsec/div.

Figure 2.14. Interferometers 1 and 2 coupled together. The upper signal represents the input to benchtop interferometer #1 while the lower signal represents the demultiplexed/demodulated output (f_{m1} = 80 kHz).

26

Figures 2.15 and 2.16 show the baseband and demultiplexed signals, respectively, for a 500 Hz benchtop interferometer signal. The ratios of the components of the signals appear to be in the same ratio but Table 2.1 shows they are not. The reader is reminded that this was not the case when the multiplexing scheme was tested with analog electronics. This difference in the ratios of the components may be due to a number of causes (or a combination thereof). These include the phase response of the low-pass filter not being constant over the entire passband, the optical path difference (OPD) in the interferometer legs and the drift angle change that occurred between plots. Independent of the reason for the change in ratios of components, the change is the same in all three legs of the interferometer and does not affect the ability of the demodulator to correctly demodulate the signal. This would tend to indicate that the cause is due to the OPD in the interferometer or the change in drift angle, rather than the phase response of the filters. Further investigation of the cause of this change was not carried out since it was always the same in all three legs and essentially amounted to a drift angle change between the baseband and demultiplexed signal.

Although Figures 2.15 and 2.16 do not show the noise floor, the measured difference between noise floors in the baseband spectrum (−114 dB re 1 V/√Hz at 5 kHz) and the demultiplexed spectrum (−98 dB re 1 V/√Hz) was 16 dB at 5 kHz (see Appendix D, Figures D8 and D9). A noise floor of −98 dB re 1 V/√Hz equates to minimum detectable signal of 13 μrad/√Hz. This is a large difference but is seen to be due to the electronics since the optical crosstalk between sensors was less than 60 dB. The crosstalk was measured by mixing with f_{m1} and measuring the size of the known spectral components due to interferometer #2. The electronics for this demonstration was assembled on a bread board with many leads to and from the demodulator. This preliminary measurement of the noise floor is considered only an estimate of the system

noise floor. The increase in noise floor and hence detectability threshold due to the multiplexing scheme should not be more than about 3-4 dB as a result of the modulation losses and demultiplexing electronics.
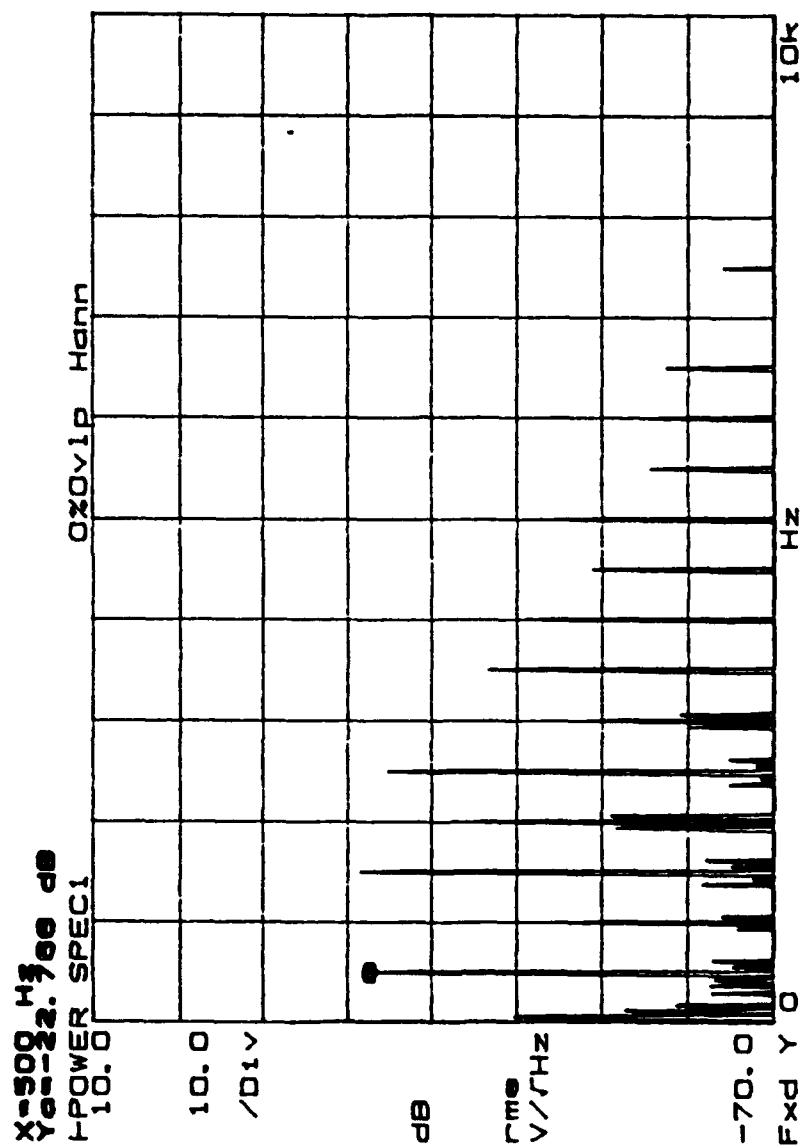

Figure 2.15. Baseband spectrum of 500 Hz benchtop interferometer signal (Note 60 Hz noise) prior to multiplexing, $\phi_s = 0.6$ radians.
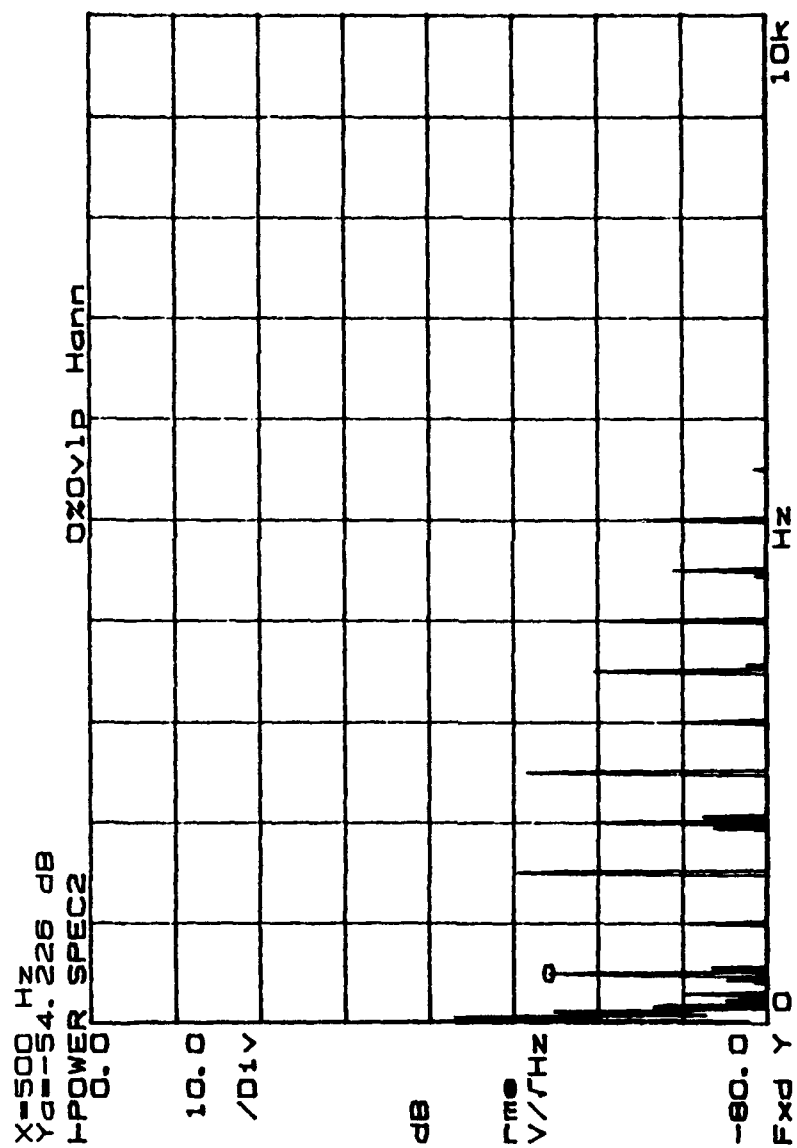
Figure 2.16. Spectrum of signal in Figure 2.15 after demultiplexing.

Table 2.1 Frequency component ratios for Figures 2.15 and 2.16.

Frequency	Baseband	Demultiplexed
f_1	−22.766	−54.226
f_2	−45.435	−70.73
f_3	−21.513	−50.376
f_4	−35.356	−59.4
f_5	−24.844	−51.565
f_6	−48.356	−68.673
f_7	−36.783	−59.632
f_8	−41.099	−61.404
f_9	−48.912	−68.99
f_{10}	−44.572	−65.533
f_{11}	−55.738	−
f_9/f_1	−26.15	−14.764
f_7/f_1	−14.02	−5.41
f_5/f_1	−2.10	2.66
f_3/f_1	1.26	3.85
f_{10}/f_2	0.86	5.20
f_8/f_2	−4.34	9.33
f_6/f_2	2.92	2.06
f_4/f_2	10.01	11.33

C. PRACTICAL LIMITATIONS

As a result of the optical demonstration several important practical limitations of the multiplexing scheme became evident. These considerations did not have any significant effect on the demonstration of the technique but would be important considerations in a complete system demonstration. The most important of these is semiconductor laser diode characteristics and the subsequent system bandwidth limitations.

1. Semiconductor Laser Diode Characteristics

A plot of the optical power output versus input drive current curve for an ideal laser diode would indicate that the maximum amplitude modulation and corresponding bias point utilize the complete linear range of laser operation [Figure 2.17]. Figure 2.18 shows an operating curve that has been exaggerated to highlight the nonlinearities and power saturation curvature.
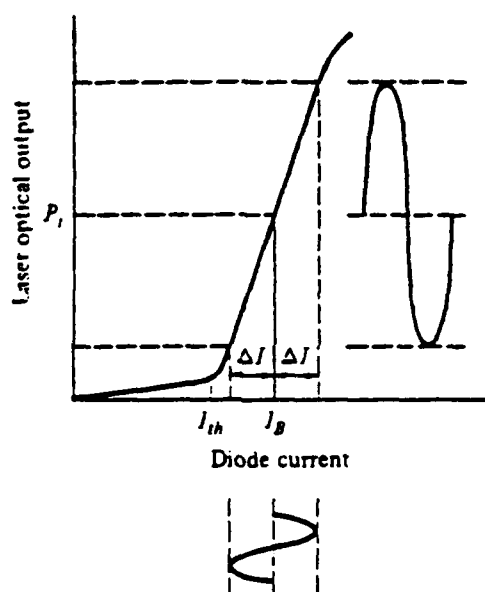

Figure 2.17. Bias point and amplitude modulation range for a laser diode (after Reference 16).

The 'kinks' or nonlinearities in the operating region are a result of inhomogeneities in the active region and power switching between different lateral modes of the laser. The downward curvature at the upper end of the operating curve, or power saturation, is attributed to active layer heating [Reference 16, page 105].
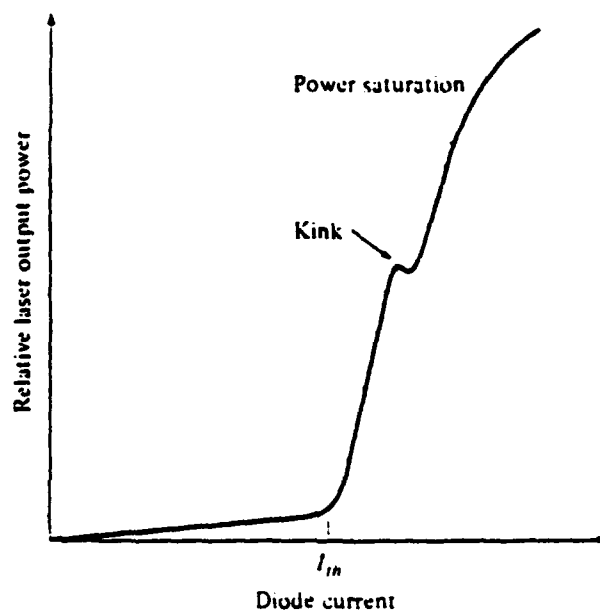
Figure 2.18. Example of kinks and power saturation in laser diode operating curve (after Reference 16).

Details of the causes and methods to reduce these nonlinearities is well documented (e.g., Reference 1, chapter 5; Reference 5, chapter 3; and Reference 16, chapter 4). Operating curves for all the lasers used in the demonstration are included (Appendix D) but are far too crude to appreciate the significance of these nonlinearities. These nonlinearities cause higher harmonics of the modulation frequency. Modulation of sensor information at higher harmonics of the carrier represents lost energy that cannot be recovered by the demultiplexing and demodulation process.

The nonlinearities can be better quantified by measuring the frequency spectrum of the optical output of an intensity modulated laser and comparing this to the frequency spectrum of the modulating drive current. Figure 2.19 shows the frequency spectrum of the HP3314A function generator used to generate the intensity modulation of the lasers shown in Figures 2.20 and 2.21. The spectrum of the HP3314A is within specifications [Reference 17, page 74].

The two lasers shown are typical of semiconductor laser diodes with the second harmonic approximately 20-30 dB down from the fundamental being the typical range stated in several of the references. One of the best traditional techniques to reduce this harmonic distortion to 30-40 dB involved the circuit technique of quasi-feedforward compensation [Reference 18] but this technique has been superseded with the advent of special purpose highly linear devices. The linearity of such devices is measured in terms of the third harmonic intercept (TOI) [see Appendix D, Figure D7]. These lasers are more expensive ($750-$1200 US) but may be required depending on the complete system requirements. It should also be noted that these lasers can only be obtained in the 1300 and 1550 nm wavelengths.

Also, if less expensive sources are used, the higher order harmonics of the carrier impose a bandwidth limitation on the system. Modulation of different sources has to be carried out in one of two ways; either at frequencies between the lowest carrier and its second harmonic, or at carriers separated from each other by more than twice the frequency of the next lower carrier frequency. The latter method can be used since the third and higher harmonics are generally negligible. Both these methods impose a stricter limit on the number of possible sensors than with the use of highly linear sources where higher order carrier components are negligible.
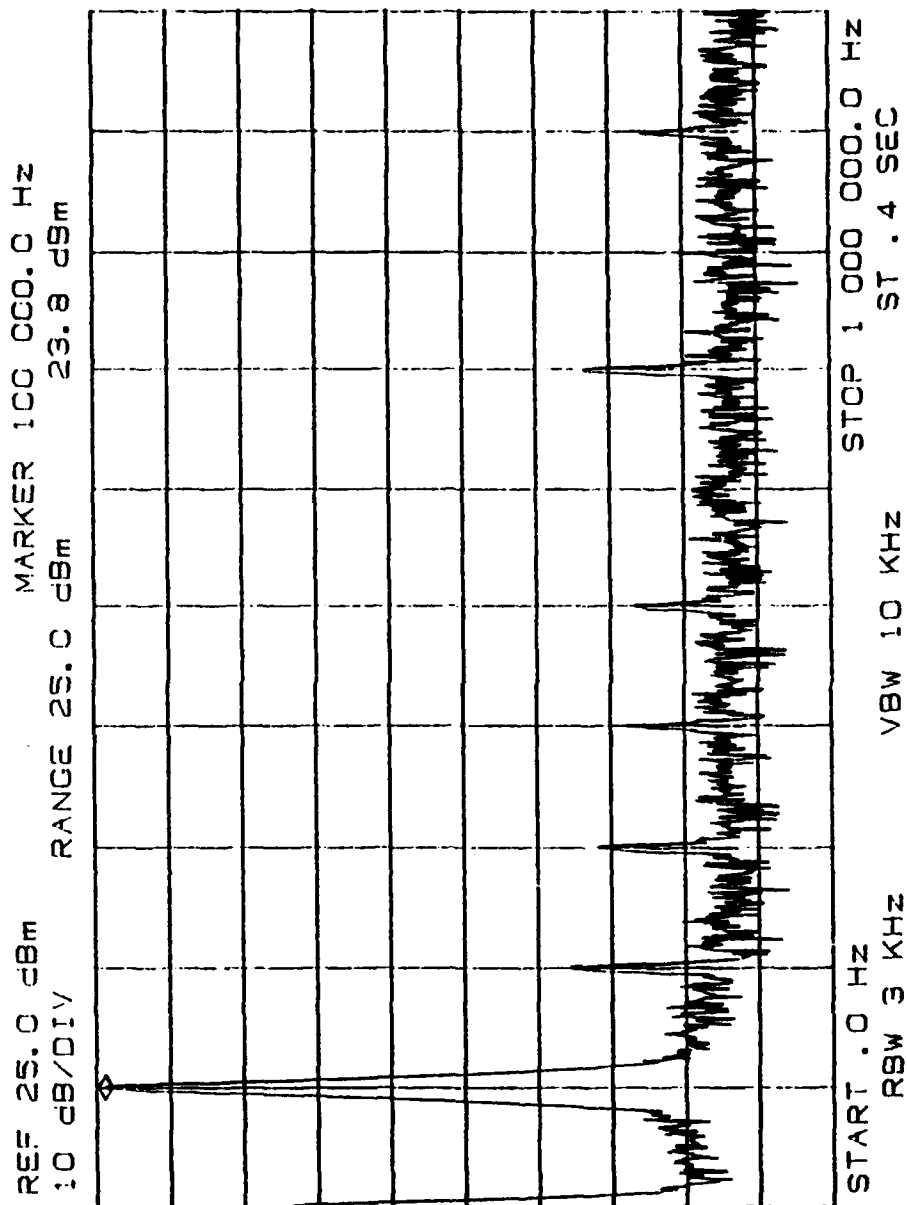
Figure 2.19. Frequency Spectrum of HP3314A Function Generator for desired output of 10 V$_{pp}$ at 100 kHz used to drive lasers of Figures 2.20 and 2.21.
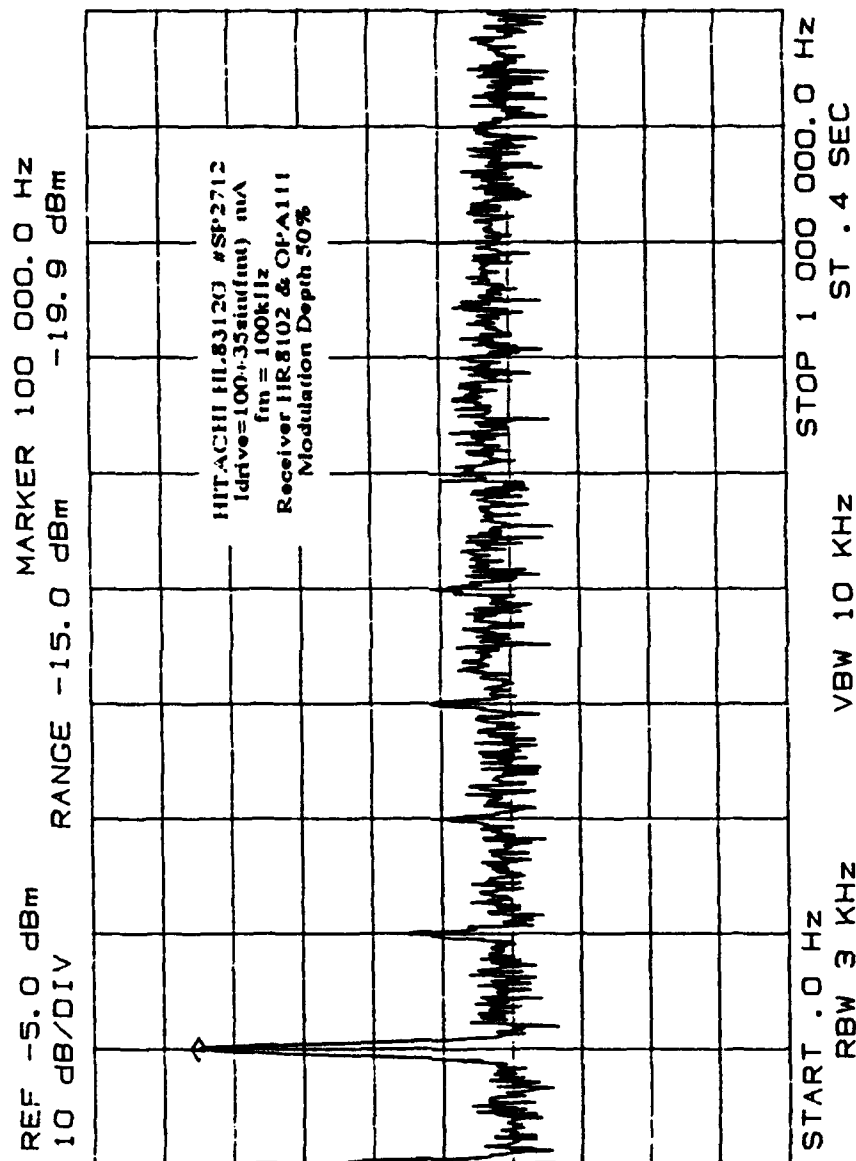
Figure 2.20. Frequency Spectrum of Hitachi HL8312G #SP2712 laser driven by Seastar LD200 power supply fed by signal of Figure 2.19.

35

MARKER 500 000.0 Hz
-60.7 dBm

RANGE 5.0 dBm

SHARP LT015MDO #SP2676
Idrive=100+50sin(fmt) mA
fm = 100kHz
Receiver UDT-020D
Modulation Depth 63%

REF 5.0 dBm
10 dB/DIV

CENTER 500 000.0 Hz
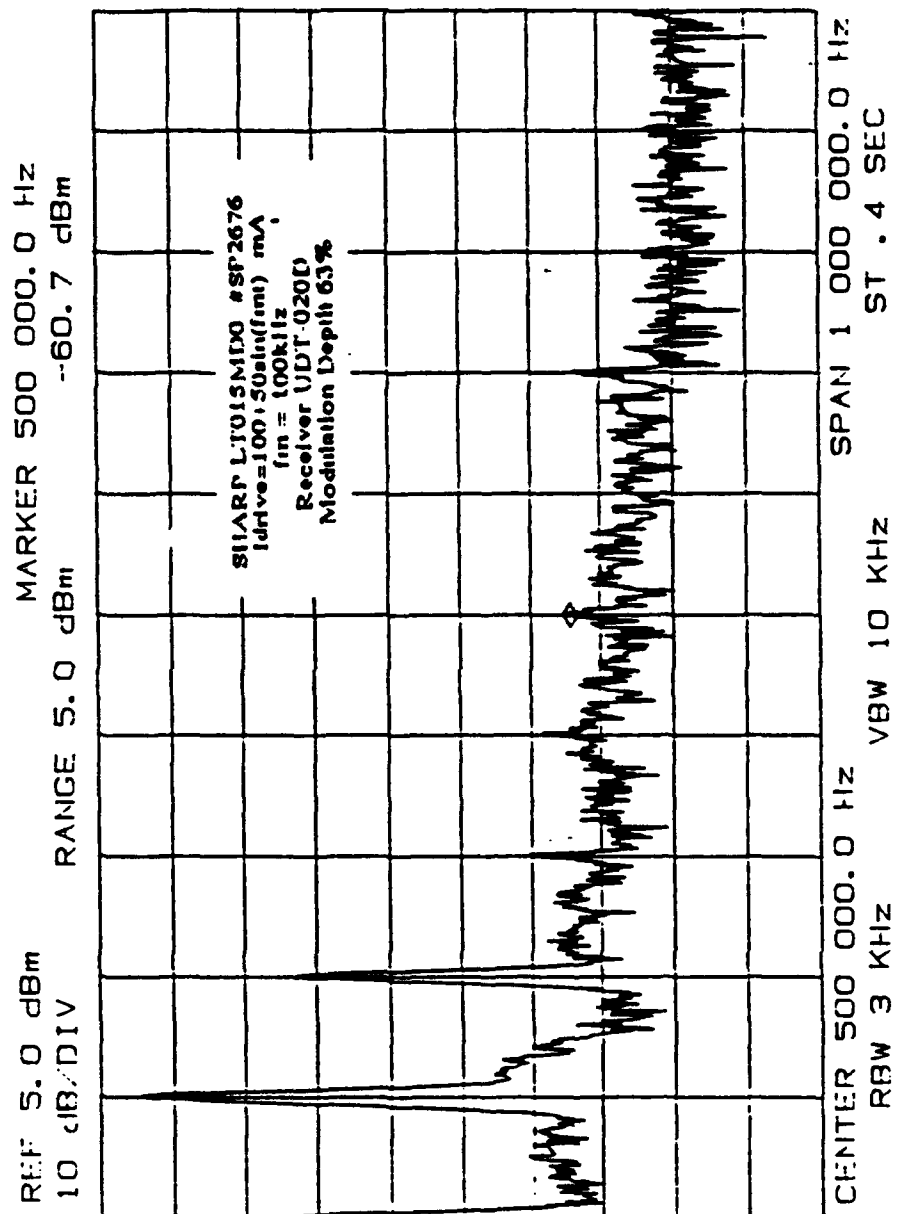RBW 3 KHz   VBW 10 KHz

SPAN 1 000 000.0 Hz
ST .4 SEC

Figure 2.21. Frequency Spectrum of Sharp LT015MDO #SP2676 laser driven by Seastar LD200 power supply fed by signal of Figure 2.19.

2. Aging and Coherence Length Considerations

The coherence length of the laser must be greater than the optical path difference in the interferometer legs. Using the typical data shown at Reference 19, page 65, a coherence length L_c of approximately 7 mm could be inferred. This was calculated using a full line width $d\lambda$ of 0.1 nm (estimated from Reference 19) and an operating wavelength of 830 nm from:

$$L_c = \frac{c}{df} = \frac{\lambda^2}{d\lambda}. \tag{2.11}$$

This L_c of 7 mm was presumed to be close to the optical path difference of the benchtop interferometer. The causes and effects of aging of semiconductor laser diodes are well documented [Reference 1, Volume I, section 5.3.3.4, Reference 5, page 56, and Reference 16, section 4-5]. One cause is related to the drive current level. The laser had been operated at high drive levels and this may have possibly reduced the coherence length of the laser. The laser was replaced with a Hitachi HL8312G which was presumed to have a longer coherence length (i.e., greater than the OPD in the interferometer), if only because it was new. The fringe visibility returned. This problem highlighted the importance of coherence length and optical path difference considerations and, especially, their relationship as a function of aging due to high drive current levels, high temperature operation, or any other aging mechanism which will change the operating characteristics of the laser diode.

3. Operating Wavelength Considerations.

The choice of 830 nm as the operating wavelength for the optical demonstration of this thesis was motivated by the inexpensive CD type semiconductor laser sources available at this wavelength. It is, however, very important to consider the overall cost of the various system components and the direction in which the optical fiber

communications industry and technology are moving. Fiber for 1300 nm sources is now cheaper than that for 830 nm. The highly linear source described earlier are only available in the 1300 and 1550 nm ranges. Optical amplifiers, which may be a consideration in multiplexing (considered later), are presently only available in the 1550 nm range.

All these cost and component availability issues need to be considered when choosing the operating wavelength for an all optical sensor array. It may well be that the developments of the communications industry will determine the most economical operating wavelength. In either case this multiplexing technique provides a less expensive source option. This technique indicates the possibility for use with inexpensive CD type sources at 830 nm ($150-350 US), or relatively inexpensive, highly linear sources similar to those for cable television applications at 1300 or 1550 nm ($750-1500 US). These sources are both inexpensive compared to the highly coherent sources required by other presently used PGC FDM techniques involving wavelength modulation of the source [e.g., Reference 2, pages 170-172], in which sources typically cost $10,000-15,000 US. This cost saving is significant enough to warrant further research into applying the technique to larger arrays at RF frequencies. With the present cost of the sources, fiber, demodulator and demultiplexing, the most expensive component in the system is the 3×3-coupler in each sensor which presently cost $400-750 US each, while 2×2-couplers cost on the order of $100 US.

III. DESIGN OF AN M X N ARRAY

A. MULTIPLEXING ARCHITECTURE FOR AN M × N ARRAY

The multiplexing technique demonstrated optically and described in Section II B, utilizing two lasers and two sensors, can be extended to an $M \times N$ sensor element array. Figure 3.1 shows a possible implementation topology for a 3×4 element array. Each of the bold vertical lines connecting a stave of sensors (or vertical column in Figure 3.1) actually represents three separate fibers and has only been drawn as one for clarity in the figure. The three interferometric signals obtained for each stave contain the sensor information from all the sensors in that stave. To reconstruct the individual sensor information the three interferometric lines must be demultiplexed once and low-pass or band-pass filtered as appropriate before demodulation. Alternatively each sensor's interferometric signals could be demultiplexed and low-pass filtered prior to demodulation. For either approach to demultiplexing, a demodulator is required for each sensor in the array if all are to be required to be interrogated simultaneously.

This is not considered to detract from the technique since the cost of parts of each demodulator [Appendix C] is approximately $150 US [Reference 21] and can be made cheaper with dedicated integrated circuits. This is a significant cost reduction over an earlier version of the demodulator [Reference 9, page 204] which quoted the cost as $270 US. This cost could possibly be reduced further by several means, including large quantity manufacture, special purpose digital signal processing (DSP) cards, or special purpose DSP chips. The approach of a specific DSP card follows on from the Naval Postgraduate School research conducted by Lt. Brian R. McGinnis, USN, and is presently being undertaken as a thesis project by LCDR David W. Brenner, Canadian Armed Forces.
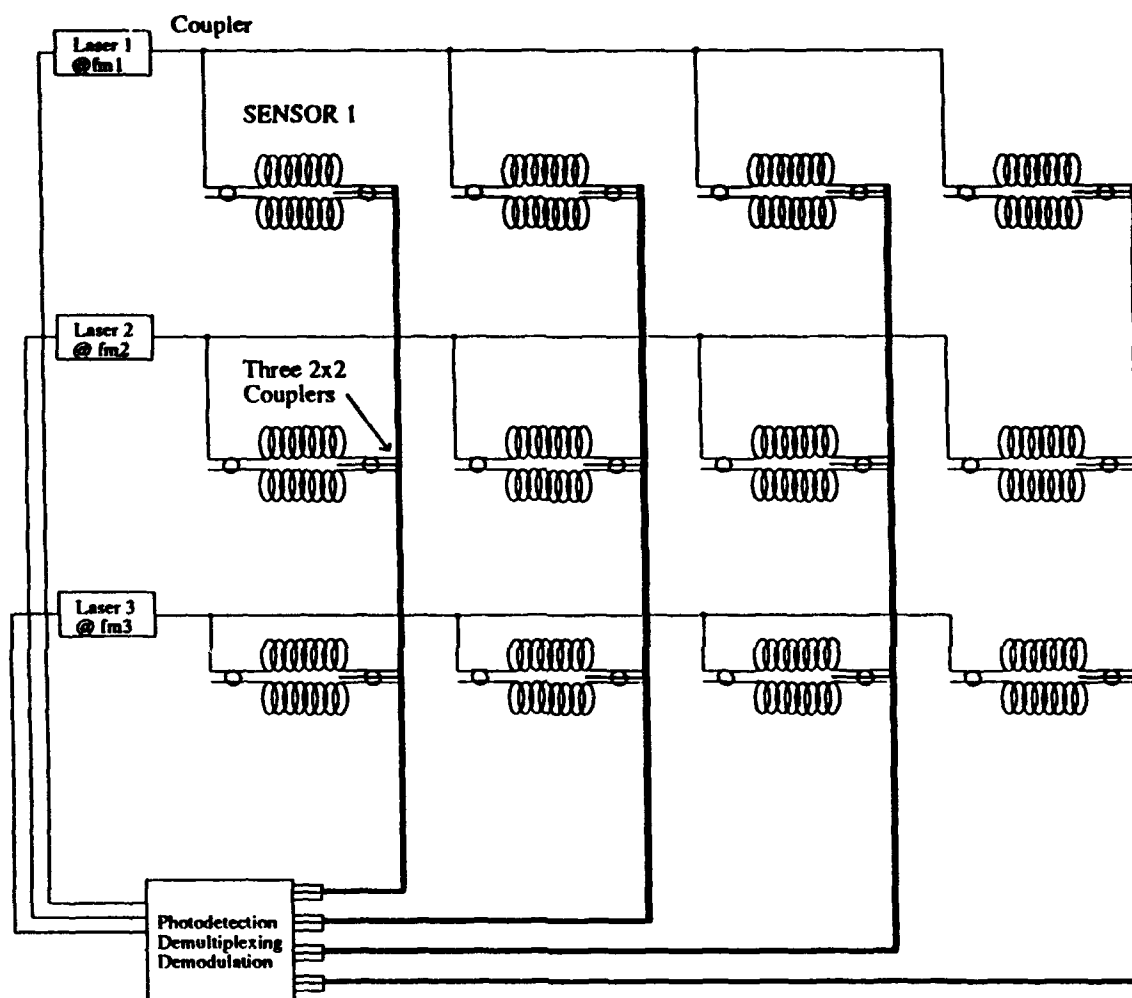
39

Coupler

Laser 1
@fm1

SENSOR 1

Laser 2
@ fm2

Three 2x2
Couplers

Laser 3
@ fm3

Photodetection
Demultiplexing
Demodulation

Figure 3.1 Multiplexing Architecture for a 3 × 4 Sensor Array.

The possibility of reducing the number of demodulators by a system of time division multiplexing (TDM) of sensor information is also an option. The added complexity and cost of incorporating TDM may be greater than that of the extra demodulators.

40

Similarly, the relatively low cost of optical fiber for short length systems, i.e., those where sensor, source, and receiver separation is of the order of tens of meters, has not made the reduction in the number of return lines a critical design parameter. There may be, however, an operational requirement to reduce the number of return lines. A deployable array or remotely operated vehicle (ROV) transmitting data to a remote location are possible examples where such a design consideration may be essential. Methods to achieve significant reduction in return lines are considered later.

An analysis of the topology of the architecture proposed in Figure 3.1 can be conducted to demonstrate the savings and costs associated with the multiplexing technique. The ratio of sensors to channels (number of optical fibers) represents a measure of the saving due to multiplexing that can easily be quantified. Using the architecture of Figure 3.1, the number of lasers is denoted by M and the number of sensors per laser by N. The number of fiber lines F is then given as the number of lasers plus three times the number of staves or return lines;

$$F = M + 3N.$$ (3.1)

Thus for the 3 × 4 array of Figure 3.1 we find the number of sensors S and number of fiber lines as:

$$S = M \times N = 12,$$ (3.2)

$$F = M + 3N = 15,$$ (3.3)

and

$$\frac{S}{F} = \frac{M \times N}{M + 3N} = 0.8 \text{ sensors / channel}.$$ (3.4)

41

For a 10×10 array:

$$S = M \times N = 100, \qquad (3.5)$$

$$F = M + 3N = 40, \qquad (3.6)$$

and

$$\frac{S}{F} = \frac{100}{40} = 2.5 \text{ sensors / channel}. \qquad (3.7)$$

Thus as the number of sensors increases the sensor-to-channel ratio increases and a multiplexing gain is realized.

Table 3.1 Number of fiber lines, F, for $M \times N$ array

Sensors/laser N	Number of lasers M								
N	2	3	4	5	6	7	8	9	10
2	8	9	10	11	12	13	14	15	16
3	11	12	13	14	15	16	17	18	19
4	14	15	16	17	18	19	20	21	22
5	17	18	19	20	21	22	23	24	25
6	20	21	22	23	24	25	26	27	28
7	23	24	25	26	27	28	29	30	31
8	26	27	28	29	30	31	32	33	34
9	29	30	31	32	33	34	35	36	37
10	32	33	34	35	36	37	38	39	40

It should also be noted that this system would work with the NRL quadrature demodulation approach [Reference 6] which uses two of the three lines.

1. Power Budget Requirements.

The limitation on the number of sensors possible is a function of the laser power available, the number of couplers required, and the bandwidth or frequency separation between modulation frequencies. The most efficient power split ratio for each coupler can be determined from its location in the array. The coupler ratio required for each coupler in a chain (horizontal row in Figure 3.1) from any laser can be calculated using Figure 3.2 as follows (neglecting intrinsic losses):

$$P(n) = (P_o - P_N)(1 - \frac{n}{N}) + P_N \tag{3.8}$$

where $P(n)$ is the power transmitted by coupler n to the next coupler, P_o the output power of the laser, and P_N the (constant) power transmitted to each sensor. The coupler ratio C_n is then defined as the ratio of the transmitted power, $P(n)$, to the input power, $P(n-1)$, and is given by:

$$C_n = \frac{P(n)}{P(n-1)} = 1 - \frac{P_N}{P(n-1)} = \frac{1}{N+1-n} \quad \text{for} \quad n = 0,1,\ldots,N-1. \tag{3.9}$$

Normalizing these calculations for a given laser output power of P_o. Equation 3.8 becomes:

$$P'(n) = \frac{P(n)}{P_o} = (1 - \frac{1}{N})(1 - \frac{n}{N}) + \frac{1}{N}, \tag{3.10}$$

where $P'(n)$ in Equation 3.10 represents the fraction of the total laser power available at coupler n.
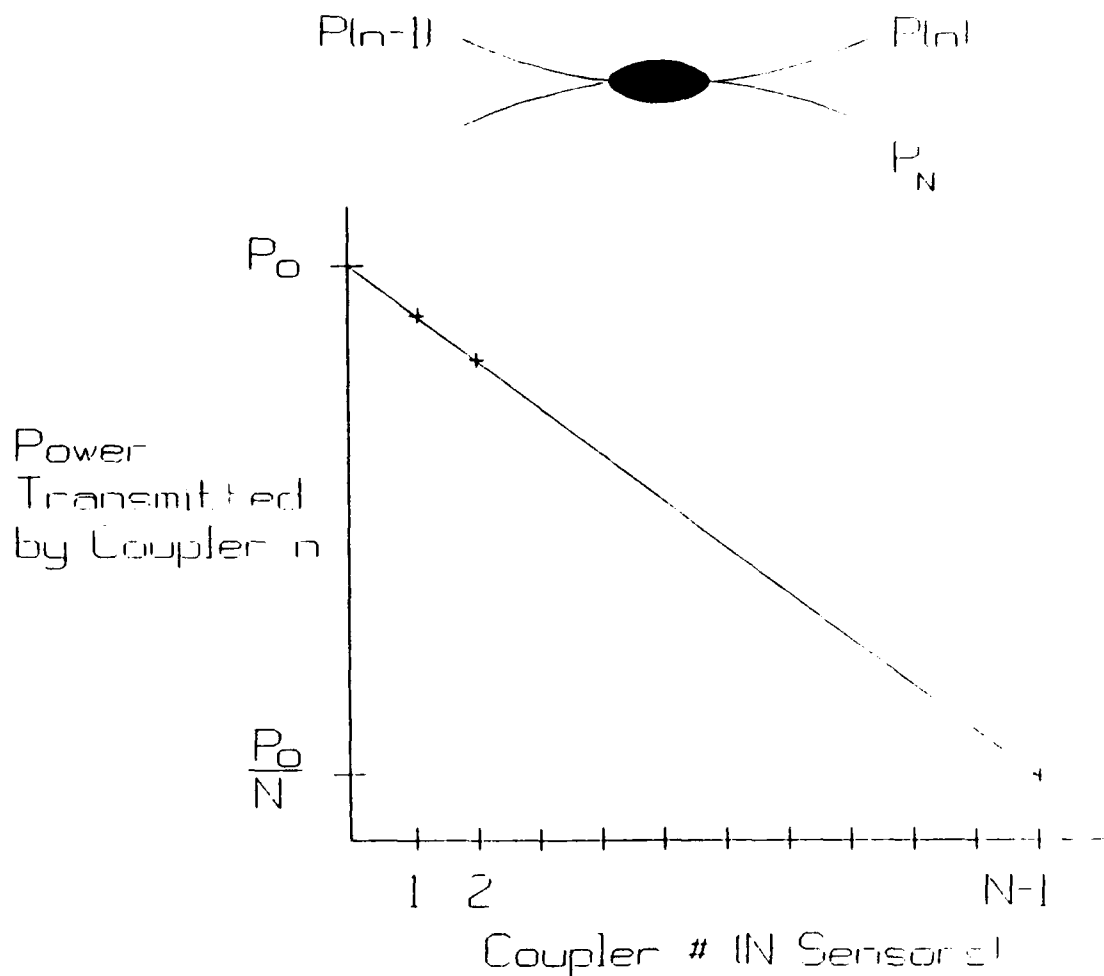
43

Figure 3.2 Power Transmission Curve for Equal Power to Each Coupler.

The calculations for the coupler power split ratios in of the return lines of each stave (vertical column of sensors in Figure 3.1) can be calculated by using the formulas from the previous calculations for the coupler ratios in a laser chain but for M sensors. These coupler ratios must then be implemented in reverse order down a stave. Thus the first or

top couplers in a stave of sensors will have a coupling ratio of 0.5 while the last or bottom couplers will have a coupler ratio of $1/M$.

In a particular laser chain, power is not wasted in the sense that light is either coupled to a sensor or transmitted to sensors further along the chain. The only losses in the chain are splice, coupler, and fiber losses. In contrast the couplers in a stave each have one leg of wasted power. The most efficient use of optical power therefore will maximize N and minimize M. The compromise is that the sensor-to-channel ratio is reduced for larger N and smaller M. A compromise between the two design parameters of maximum optical power per sensor and maximum sensor-to-channel ratio must be made based on the application requirements.

A MATLAB™ routine [Appendix D] was written to calculate the maximum output power from each sensor for any given array size, $M \times N$. This routine takes into account the system losses based on the following estimates of the individual losses. These estimates are based on the typical losses for those components used in the 2×1 optical demonstration. Loss estimates are assumed as follows:

- loss/coupler (single mode)   0.5 dB

- loss/splice (single mode fiber)   0.2 dB

- fiber loss @ λ = 830 nm   3.0 dB/km

- fiber length/sensor   80 m [Reference 22]

- typical laser output power(at $1m$ pigtail)   3 mW or 4.8 dBm

- typical noise floor at receiver   −110 dBV re 1 μrad/√Hz

- fiber length between sensors   30 m (e.g., for 50 Hz array)

Thus the loss per sensor can be calculated as:

$$2 \times 0.5(\text{coupler}) + 4 \times 0.2(\text{splice}) + 3 \times 0.08\text{km}(\text{sensor fiber}) = 2.04 \text{ dB}/\text{sensor}, \quad (3.11)$$

45

and the loss per coupler including the fiber loss between couplers as:

$$0.5 + 3 \times 0.03 \text{km(fiber loss)} = 0.59 \text{ dB}. \qquad (3.12)$$

The loss per coupler (0.59 dB) and loss per sensor (2.04 dB) have been included in the MATLAB™ routine.

Examples are shown below for different values of M and N for both the fraction of laser power available and an estimated power of 3 mW, based on data for the HL8312G Hitachi source [Reference 23]. By comparing the calculations for a 4×25 element array and a 10×10 element array, the compromise between optical power and number of return lines for these two implementations of a 100 element array can be seen. Figures 3.3 and 3.4 compare the fractional power transmitted to a particular coupler n in a laser chain for the two cases. Figures 3.5 and 3.6 compare the coupler ratios for couplers in a particular laser chain for the two arrays. The reason that the last coupler is not exactly one half in each case is due to the estimated losses included in the calculations. Figures 3.7 and 3.8 show the power from each sensor in a laser chain for the two cases. There is approximately 2.7 dBm more power delivered to each sensor in the case for $N = 10$.
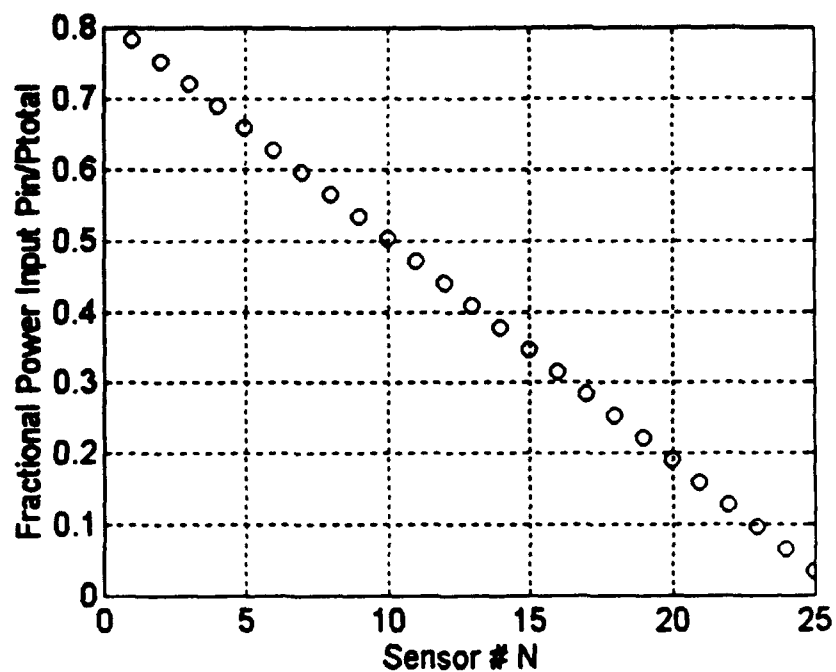
46

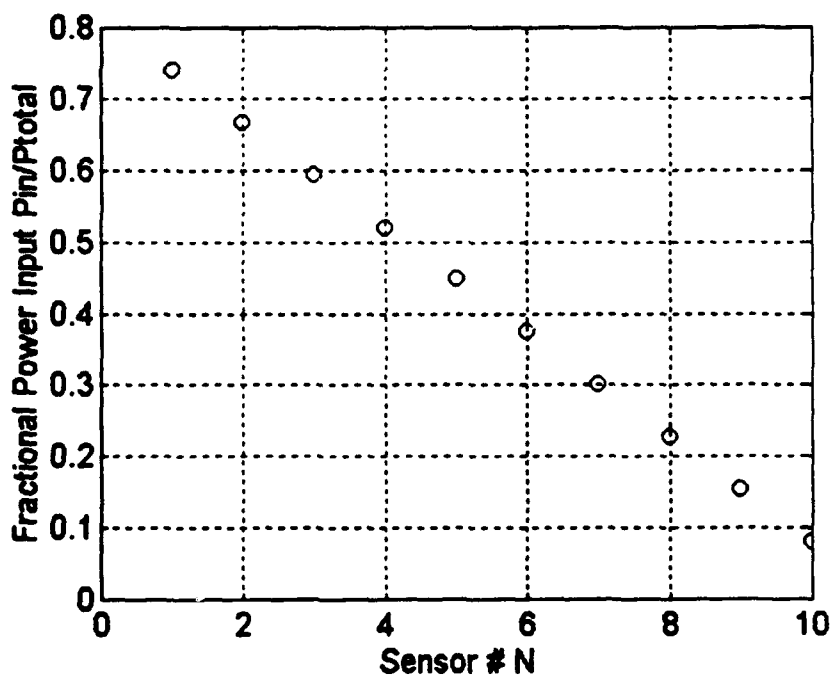**Figure 3.3. Fractional power transmitted for couplers from a particular laser for a 25 element chain.**

Figure 3.4. Fractional power transmitted for couplers from a particular laser for a 10 element chain.
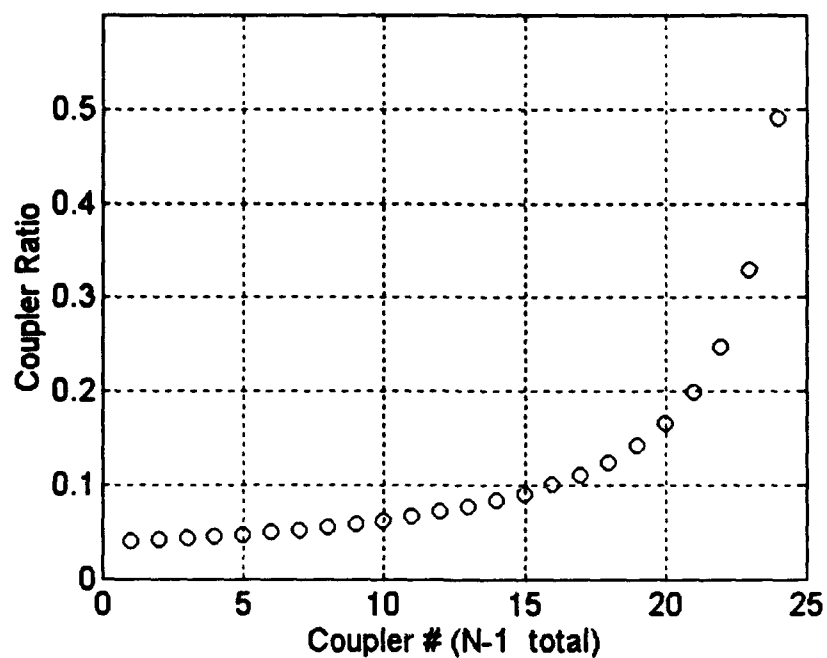
47

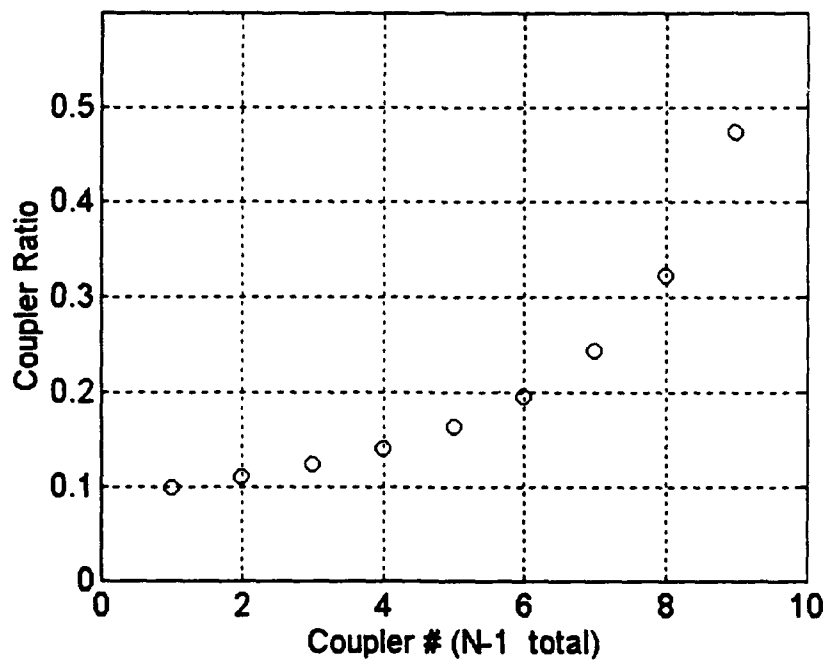**Figure 3.5. Coupler ratios in a particular laser chain for 25 element chain.**

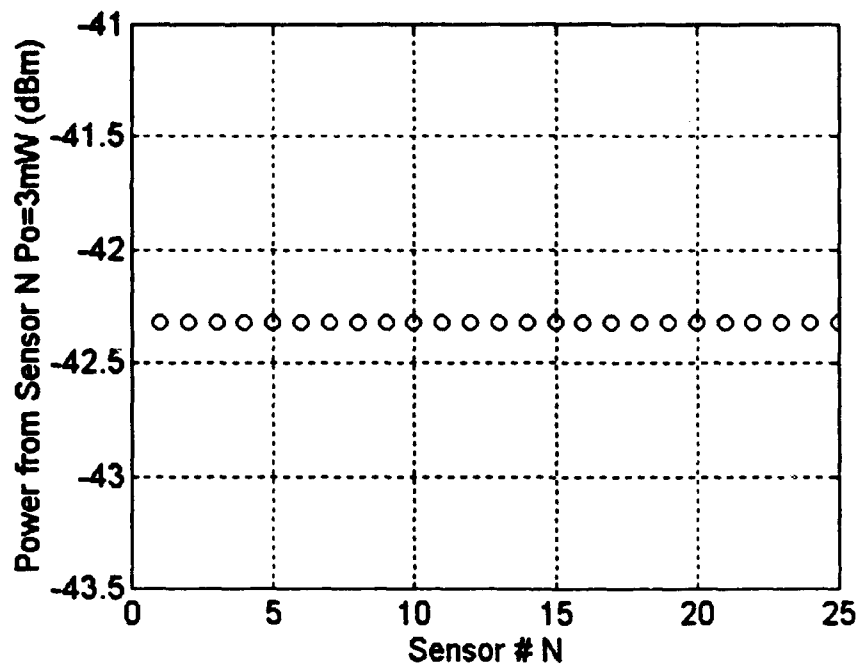**Figure 3.6. Coupler ratios in a particular laser chain for 10 element chain.**

48

Figure 3.7. Estimated power coupled to each sensor in chain for Hitachi HL8312G laser (3 mW at 1 m pigtail), including estimated losses, N = 25.
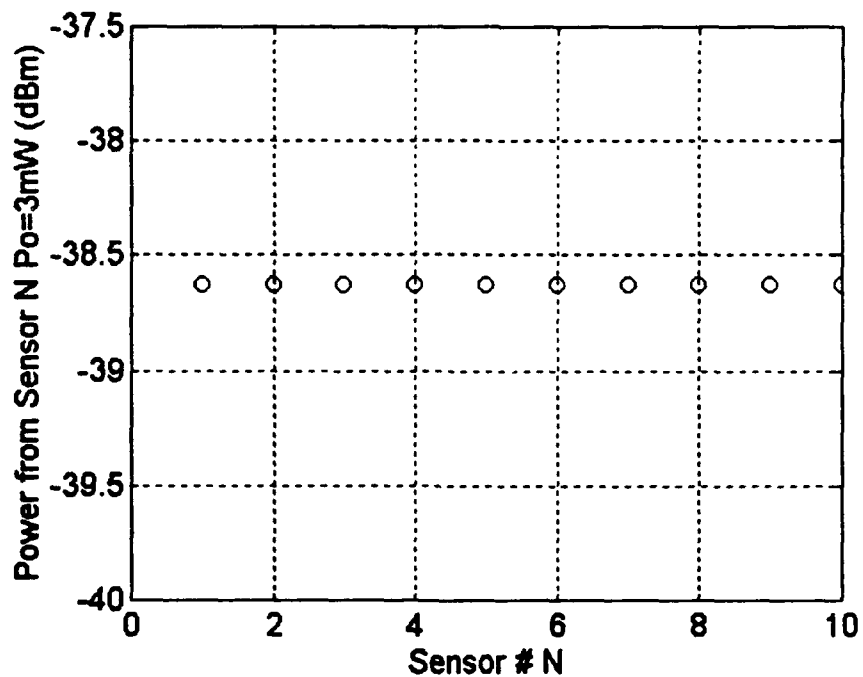

Figure 3.8. Estimated power coupled to each sensor in chain for Hitachi HL8312G laser (3 mW at 1 m pigtail), including loss estimation, N = 10.

Figures 3.9 and 3.10 show the coupler ratios for each coupler down a stave (or column in Figure 3.1). Again the first coupler is not exactly equal to one half as a result of the losses. The most important results of this analysis are shown in Figures 3.11 and 3.12 where the estimated optical power for each sensor down a stave are compared for the two cases. The power for the last sensor in the stave represents the power coupled from each leg of each sensor in the array that is received at the photodetector. It can be seen that for the 10 × 10 array the power lost as a result of the lost (unused) power from each coupler in every stave is so significant that there will insufficient power at the photodetector. The estimated system noise floor is expected to be approximately −90 to −110 dBm. The 4 × 25 array, on the other hand, is able to deliver approximately −58 dBm, which is on the order of 50 dB above that for the 10 × 10 array.
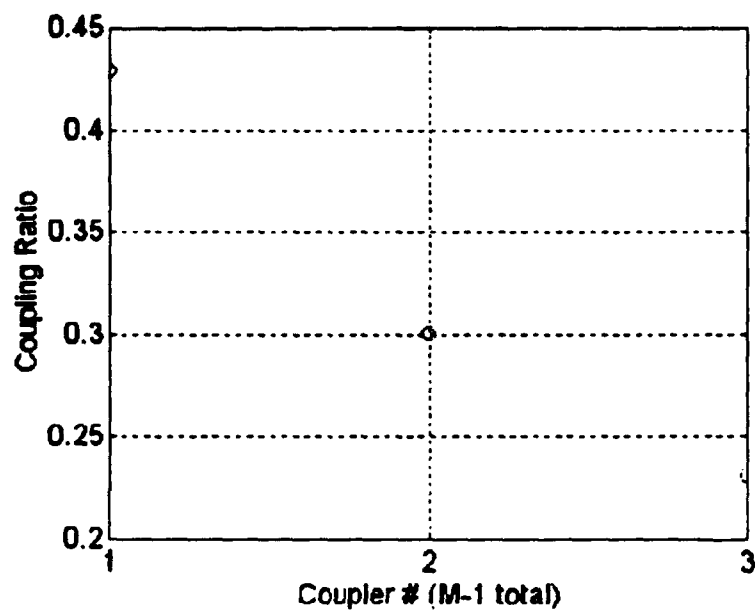
Figure 3.9. Coupler ratio for couplers in each stave (column in Figure 3.1) for 4 × 25 element array.
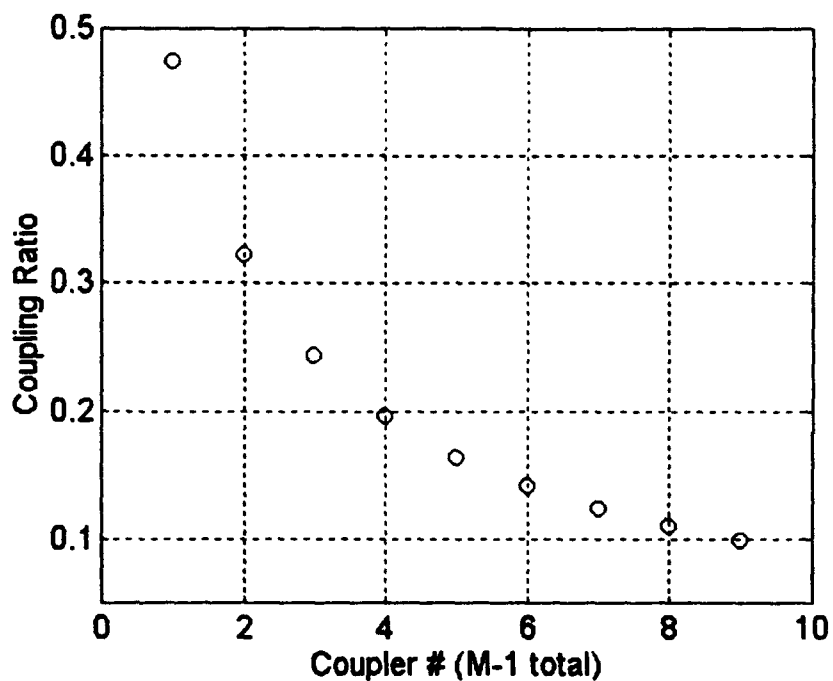

Figure 3.10. Coupler ratio for couplers in each stave (column in Figure 3.1) for 10 × 10 element array.
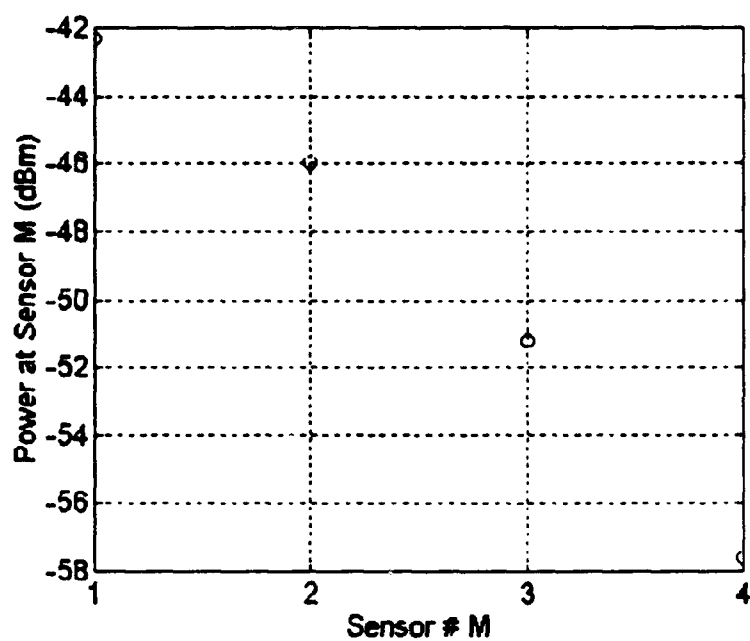
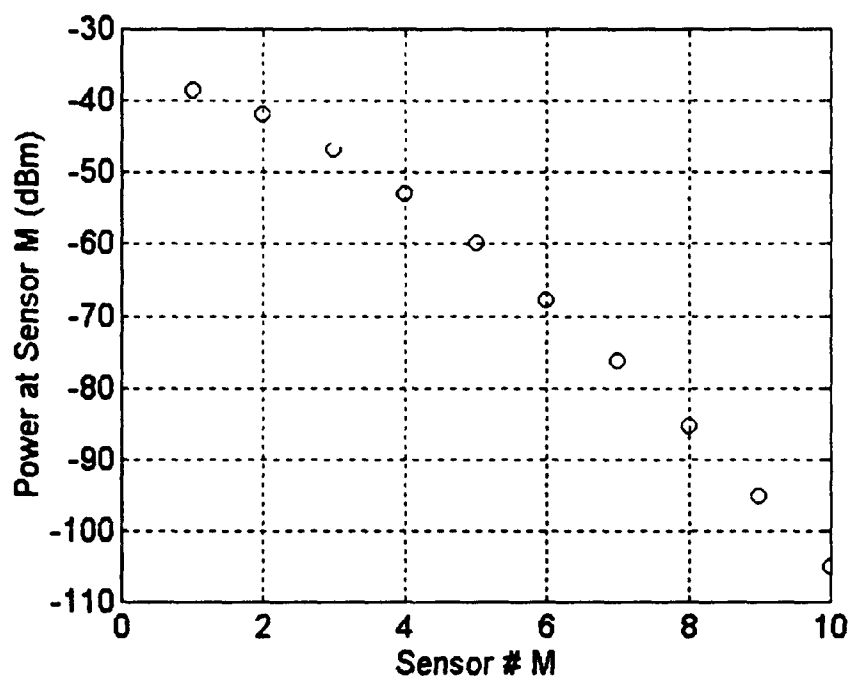Figure 3.11. Power coupled down a stave for 4 × 25 element array.

Figure 3.12. Power coupled down a stave for 10 × 10 element array.

52

An optical sensor array topology is not only different from present piezoelectric with twisted pair, or coaxial lines, but may vary depending on the specific application. A hull mounted array, for example, may best be implemented with no multiplexing in either one laser per sensor, or a shared laser topology as shown in Figure 4.1. The savings in size and weight realized by an optical system over those presently available may preclude the requirement for multiplexing.
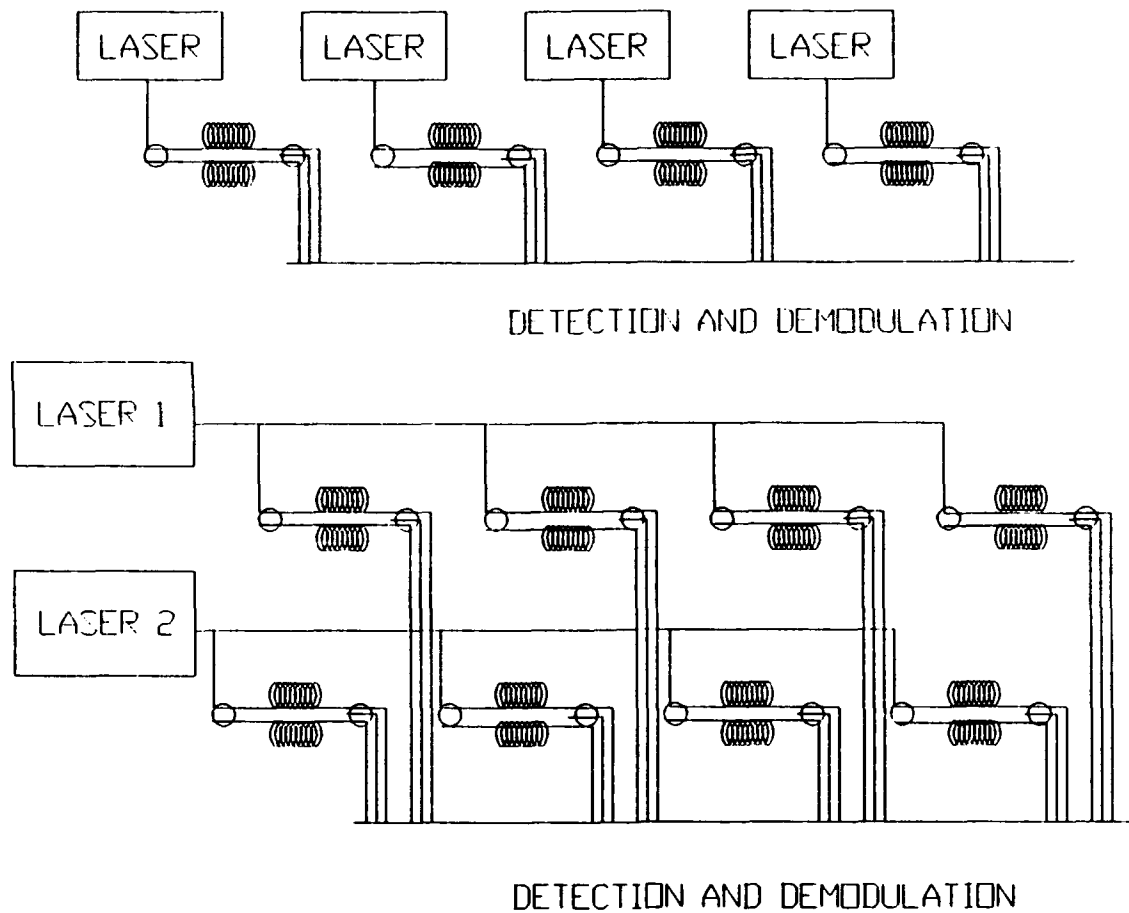

DETECTION AND DEMODULATION

DETECTION AND DEMODULATION

Figure 3.13. Array topologies for a hull mounted optical array: one sensor per laser (upper) and shared laser chain (lower).

2. Bandwidth Limitations

Consider a system of M lasers with the lowest modulation frequency f_{m1} at 20 MHz. Let the upper design limit of 20 kHz be the maximum acoustic frequency with a dynamic range of 140 dB at 100 Hz. Using Equation 2.10, and assuming similar noise floor and maximum acceptable distortion levels, this gives the significant bandwidth of the interferometric signal as:

$$f_{ab} = 5\phi_s f_s = 5 \times (0.5 \times 10^{-6} \times 10^{140/20}) \times 20 = 500 \, \text{kHz}. \qquad (3.13)$$

With the fact that we have both upper and lower sidebands, a 1 MHz frequency separation is required between laser modulation frequencies. For f_{m1} at 20 MHz this represents an upper limit of 20 sensors that can be accommodated before the second harmonic of the lowest carrier f_{m1}.

Investigation of an $M \times N$ array reveals that the optical power restrictions imposed by coupling sensors in a stave and the subsequent lost or wasted power at every coupler is a far more stringent design consideration than bandwidth limitations.

B. REDUCTION IN THE NUMBER OF RETURN LINES.

An application such as a deployable array or remotely operated vehicle (ROV) may require significant reduction in the number of return lines. The number of return lines may be required to be reduced beyond that shown in Figure 3.1 or even down to a single return line. The cost of additional optical fiber may be greater than that of the extra couplers and processing required in a system with reduced return lines. This is the case in systems where the distance between sensors and/or receivers and/or sources become too large. At approximately 50 mil to the gallon (container), fiber is far cheaper and more compact than copper.

A simple method for reducing the number of return lines utilizing 3×3-coupler terminated sensors and symmetric demodulation is a combination of OSCUM detailed earlier and time division multiplexing (TDM). TDM has been successfully demonstrated with intensity based sensors [e.g., Reference 2, pages 165-6, and Reference 4, page 95] and interferometric sensors [e.g., Reference 2, page 172-176, Reference 3, pages 82-84, and Reference 4, pages 96-100].

The discussion of Reference 3, page 83, in which TDM with Mach-Zehnder sensors terminated with 2×2-couplers is presented, can be adapted to the case for 3×3-coupler terminated sensors and symmetric demodulation. Such a scheme is shown in Figure 3.14. The demultiplexing of the pulses would have to be carried out prior to demodulation. Each input pulse generates one pulse per sensor on each of the three output lines. These output pulses must be appropriately gated to relate them to their respective sensor. In order to correctly determine which pulse is associated with which sensor and to ensure that there is no overlap of pulses, the pulse duration must be less than the propagation delay between any two sensors, and the time between pulses must be greater than the propagation delay difference between the shortest and longest paths.

The power output per sensor can be maximized in a fashion similar to the previous section by choosing the coupling ratios of the couplers appropriately. There is, however, an additional power loss in a TDM system due to the duty cycle of the source.
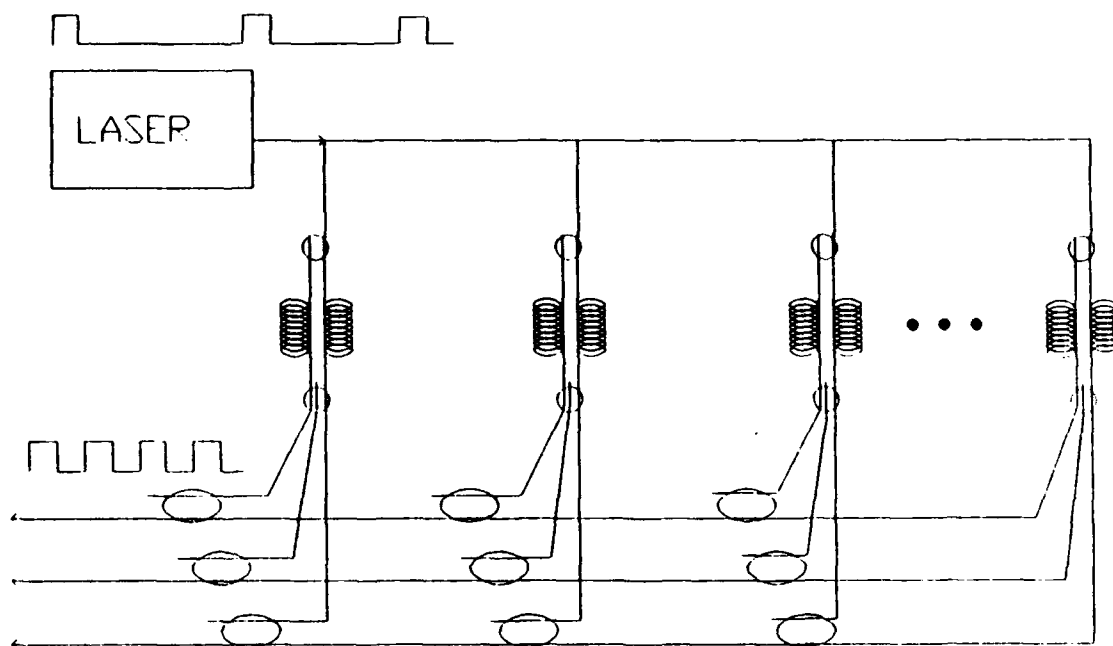
Figure 3.14. TDM with 3×3-coupler terminated sensors for symmetric demodulation (adapted from Reference 3).

The number of return lines of the complete array could be reduced to a single line by TDM of the individual sensor legs. This introduces further losses and demultiplexing complexity. A combination of OSCUM and TDM could be employed to improve the optical power per sensor (equivalently the SNR of each sensor). A scheme incorporating a single return line and a combination of OSCUM and TDM is proposed in Figure 3.15. The loop diameters indicate relative differences in path length delays.
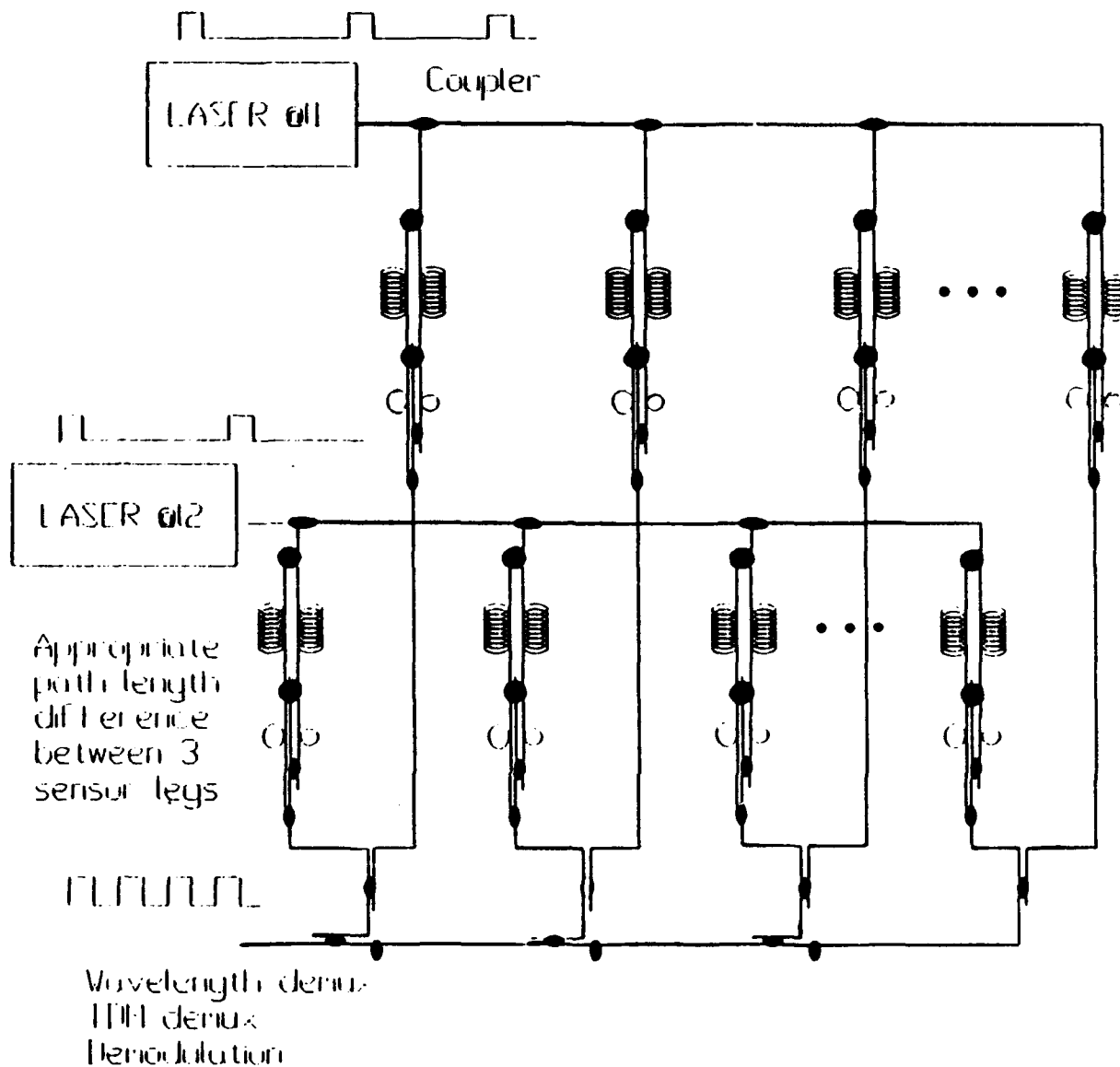
Figure 3.15. Single return architecture incorporating OFSUM and TDM.

It should also be noted that a system with a reduced number of return lines is not as robust in the sense that the loss of a single fiber or coupler leads to a much larger or total loss of sensor information while this loss is reduced for the case of more return lines. Again the application will dictate the costs and benefits involved. References 3, 4, and 5

57

provide an overview of the techniques presently used with a variety of other types of sensors and demodulation techniques. Further research is required to apply these techniques to 3×3-coupler terminated Mach-Zehnder sensors with symmetric demodulation.

IV. CONCLUSIONS

The technique of 'optical fiber subcarrier frequency multiplexing' has been successfully demonstrated with a 2 × 1 element array. This is the first time that this multiplexing technique has been known to be demonstrated with interferometric sensors.

The architecture for a particular array is very application specific with the requirements of the particular application dictating the multiplexing technique to be utilized. This occurs as a result of the large power budget trade-offs incurred when optical signals are recombined through couplers. The development and introduction of low cost optical amplifiers may provide a solution to this problem.

The following list details some of the follow-on work recommended to further the goal of all optical sensor systems for a wide variety of applications.

- Demonstration of the technique at RF frequencies with a larger number of sensors (or simulated sensors), possibly with highly linear sources similar to those described in Chapter II, section B.2.

- Investigation of a method to digitally implement the multiplexing scheme to further reduce costs and hardware complexity.

- Investigation and demonstration of techniques to reduce the number of return lines for specific applications.

- A less expensive 3×3-coupler, or alternative to the 3×3-coupler that presently terminates the sensors developed at NPS.

REFERENCES.

1.   Dakin, J. and Culshaw, B., *Optical Fiber Sensors: Principles and Components (Volumes I and II)*, Artech House, Norwood MA, 1989.

2.   Kersey, A. D., "Multiplexed Fiber Optic Sensors," *Proceedings of Distributed and Multiplexed Fiber Optic Sensors II*, SPIE (Vol. 1797), pages 161-186 Bellingham WA, 1992.

3.   Wagoner, R. E. and Clark, T. E., "Overview of Multiplexing Techniques for All-fiber Interferometric Sensor Arrays," *Proceedings of Fiber Optic and Laser Sensors IV*, SPIE (Vol. 718), pages 80-91, Bellingham WA, 1986.

4.   Kersey, A. D. and Dandridge, A., "Fiber Optic Multisensor Networks," *Proceedings of Fiber Optic and Laser Sensors VI*, SPIE (Vol. 985), pages 90-104, Bellingham WA, 1988.

5.   Udd, E., *Fiber Optic Sensors: An Introduction for Scientists and Engineers*, Wiley, New York, 1991.

6.   Koo, K.P., Tveten, A.B., and Dandridge, A., "Passive Stabilization Scheme for Fiber Interferometry Using (3x3) Fiber Directional Couplers," *Applied Physics Letters*, **41**, 616, 1982.

7.   Cameron, C. B., Keolian, R. M., and Garrett, S. L., "A Symmetric Analog Demodulator for Optical Fiber Interferometric Sensors," *Proceedings of Mid West Symposium on Circuits and Systems* (Volume 2 pages 666-671), IEEE, Piscatawy NJ, May 1991.

8.   Brown, D. A., Cameron, C. B., Keolian, R. M., Gardner, D. L., and Garrett, S. L., "A Symmetric 3x3 Coupler Based Demodulator for Fiber Optic Interferometric Sensors," *Proceedings of Fiber Optic and Laser Sensors IX* (Volume 1585 pages 328-335), SPIE, Bellingham WA, 1991.

9.   Cameron, C. B., *Recovering Signals from Optical Fiber Interferometric Sensors*, PhD dissertation, Naval Postgraduate School, Monterey CA, June 1991.

10.   Abramowitz M. and Stegun I. A., *Handbook of Mathematical Functions With Formulas, Graphs, and Mathematical Tables*, US Department of Commerce, National Bureau of Standards Applied Mathematics Series 55, Tenth Printing 1972.

11.   Reid, G.J. and Brown D.A., "Multiplex Architecture for 3x3 Coupler Based Fiber Optic Sensors," Presented at SPIE, Distributed and Multiplexed Fiber Optic Sensors III, Boston, September 1993 (Proceedings to be published in December 1993).

12.   Seastar Optics, *LD200 Ultra Stable Laser Diode Driver Operator's Manual*, November 1988.

13.   Digi-Key Corporation, Catalog No. 933, May-June 1993.

14.   Horowitz, P. and Hill, W., *The Art of Electronics*, Cambridge University Press, New York, 1984.

15.   Reid, G.J., *Thesis Laboratory Notebooks 1 and 2 (Spanagel - 011)*, Physics Department Naval Postgraduate School, Monterey CA, February - November 1993.

16.   Keiser, G., *Optical Fiber Communications*, McGraw Hill, New York, 1983.

17.   Hewlett Packard, *3314A Function Generator Operating Manual*, 1982.

18.   Patterson, R.E., Straus, J., Blenman, G., and Witkowicz, T., "Linearization of Multichannel Analog Optical Transmitters by Quasi-feedforward Compensation Technique," *IEEE Trans. Comm.*, COM-27, pages 582-588, Piscatawy NJ, March 1979.

19.   Sharp, *Laser Diode User's Manual*, September 1986.

20.   French A.P., *Vibrations and Waves*, Norton, New York, 1971.

21.   Interview between Professor David Gardner PhD., Physics Department Naval Postgraduate School, Monterey CA, and the author, 25 October 1993.

22.   Interview between Greg Netzorg, Physics Department Naval Postgraduate School, Monterey Ca., builder of the most recent design of fiber optic sensors developed at the Naval Postgraduate School, and the author, 29 October 1993.

23.   Hitachi, *Optoelectronic Devices Data Book*, March 1988.

APPENDIX A. SPECTRUM OF AN INTERFEROMETRIC SIGNAL

The interferometric signal output from a 3x3 terminated Mach-Zehnder interferometer with input signal $\phi(t)$ (Equation A1), expanded into a Bessel weighted series, is given by equation A2:

$$
\begin{aligned}
I(t) &= A + B\cos(\phi(t)) \\
\phi(t) &= \phi_s \sin \omega_s t,
\end{aligned}
\tag{A1}
$$

$$
\begin{aligned}
I(t) = A + B\cos\big(\phi_{drift}(t)\big)\left[J_0(\phi_s) + 2\sum_{l=1}^{\infty} J_{2l}(\phi_s)\cos(2l\omega_s t) \right] \\
- B\sin\big(\phi_{drift}(t)\big)\left[2\sum_{l=0}^{\infty} J_{2l+1}(\phi_s)\sin\big[(2l+1)\omega_s t\big] \right],
\end{aligned}
\tag{A2}
$$

where $\phi_{drift}(t)$ is the slowly varying (compared to the signal of interest) or drift phase term which includes the phase shift due to environmental effects (hydrostatic pressure, temperature, etc.) as well as the physical difference in the length of the legs and the phase shift due to the coupling region of the interferometer.

Thus, for a given $\phi_{drift}(t)$ (assumed to be a constant over the time scale of the signal of interest $2\pi/\omega_s$) the ratio of the spectral components of odd or even harmonics of the signal of interest will be determined by the ratio of the Bessel functions. This property can be used to determine the operating point, i.e., the magnitude of ϕ_s, by measuring these ratios of components and relating them to the equivalent Bessel function ratios (i.e., J_2/J_4, J_3/J_5, etc.) [Reference 9, page 28]. This is especially useful for determining the operating point in the 'sub-fringe' range. Figure A1 shows the lower order Bessel functions and Table A1, the component ratios for $\phi_s = \pi$ radians amplitude, which can be used to verify

the examples of $\phi_s = \pi$ radians amplitude and drift angles $\phi_{drift} = 0°, 90°, 120°,$ and $240°$, shown in Figure A2.

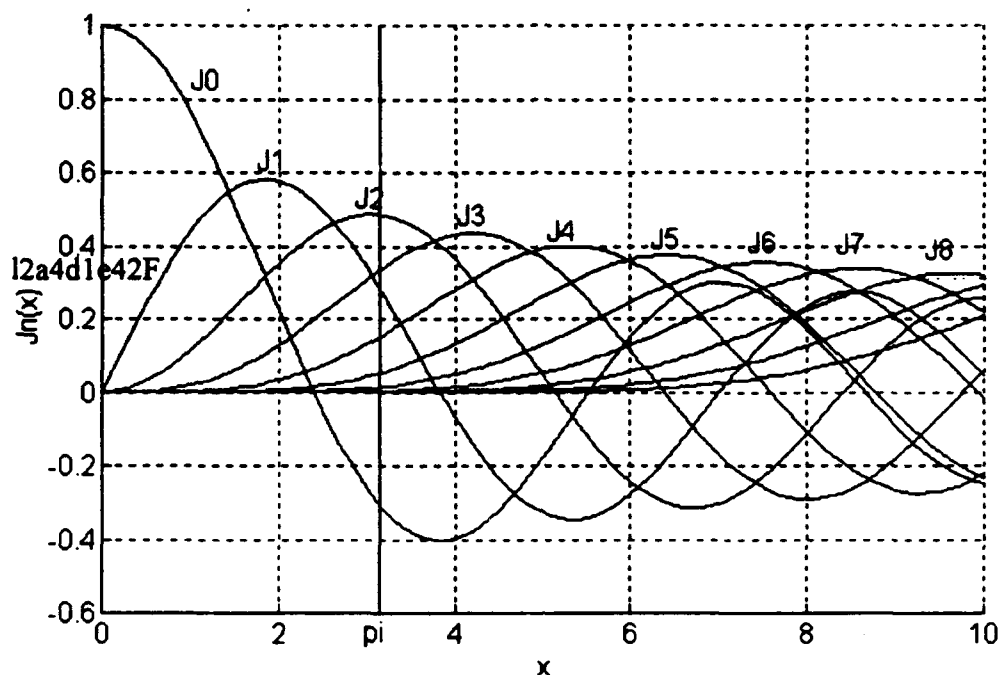**Figure A1. Bessel Functions J_0 through J_{10} up to argument 10.**

Table A1. Bessel Function Values and Ratios for $\phi_s = \pi$ radians.

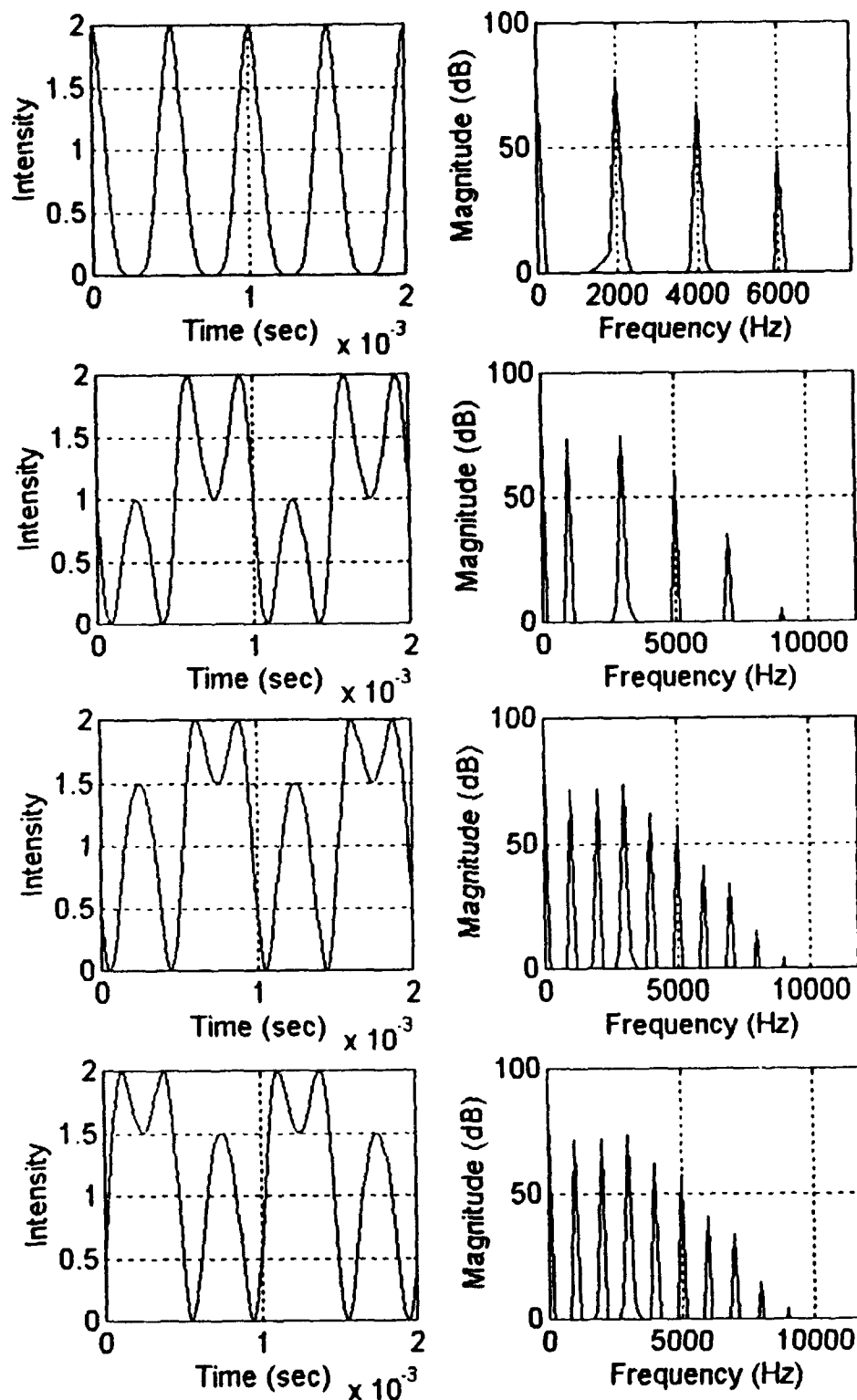| Bessel Fn.	Value	Ratio	Value
J0	-0.3042	J3/J1	1.17182
J1	0.2846	J5/J1	0.183064
J2	0.4854	J5/J3	0.156222
J3	0.3335	J7/J1	0.011947
J4	0.1514	J7/J3	0.010195
J5	0.0521	J7/J5	0.065259
J6	0.0145		
J7	0.0034		
J8	0.0007	J4/J2	0.311908
J9	0.0001	J6/J4	0.095773
J10	0	J6/J2	0.029872

Figure A2. Time waveform (left) and spectrum (right) for $\phi_s = \pi$ radians for (top to bottom) (a) $\phi_{drift} = 0°$, (b) $\phi_{drift} = 90°$, (c) $\phi_{drift} = 120°$, (d) $\phi_{drift} = 240°$.

APPENDIX B. SYMMETRIC ANALOG DEMODULATOR VERSION 2.1

Reference 9 details the first implementation of the symmetric demodulation scheme using analog electronics. The analog implementation was redesigned by Dr. David L. Gardner with vastly improves the small-signal performance over the original implementation. Gardner's implementation was not previously documented and was used for the multiplexing demonstrations of this thesis.

The circuit schematic is shown at Figure B1. The algorithm is well documented [References 3, 4, 5, and 7] with version 2.1 described here being configured for lower noise floor and ease of component manipulation. The circuit description is divided into several distinct stages adapted from Dr. Gardner's notes. Performance results of version 2.1 are included.

A. INPUT STAGE

1. Photodiodes.

Three input choices are available as follows:

1. Three 1300 nm photodiodes are the lower row of bulkhead SMA connectors. Presently fitted are model UDT080 devices (with an active area of 0.08 mm^2). These devices are selected by opening the box and moving each of the three blue jumpers (adjacent to the edge connector) to the left-most position as one looks down on the board facing the edge connector. These small and, hence, fast diodes may present some difficulty in alignment. Both the fiber and diodes can be epoxied into position for field tests.

Figure B1. Symmetric Analog Demodulator Version 2.1 Circuit Schematic

2. **Three 830 nm photodiodes are the upper row of bulkhead SMA connectors.** Presently fitted are model HR8102 devices (with an active area diameter of 300 μm). These detectors are selected by opening the box and moving each of the three blue jumpers (adjacent to the edge connector) to the right-most position as one looks down on the board facing the edge connector. These also should be fixed into position with epoxy for field tests.

3. It is often convenient to use interferometric sensor simulators to test demodulators and conduct various other trials. Since the output from these simulators is a voltage, an input resistor has been installed to allow the demodulator to be used with the simulators. This will cause the input amplifier to be an inverting type rather than the transimpedance configuration required for the photodiodes. Three 9207 Ω resistors are precision type and can be used in conjunction with the fixed value feedback resistor to test the operation of the demodulator input. The box must be opened to gain access to these resistors. They are gray and installed vertically along the edge of the board adjacent to the connector. The long lead of the resistor is available for connection but, first, the blue jumpers must be removed.

2. Input Amplifiers.

Two options are available for gain control of the input amplifiers:

1. Fixed-value resistors - In the course of testing interferometric sensors, it is useful to determine the light power in each of the sensor fibers. The typical responsivity of the photodiodes is 0.5 A/W. Since the current-to-voltage ratio or conversion factor must be known to make such a measurement, 20 kΩ resistors have been installed. These resistors are selected by opening the box and moving the black jumpers, located along the left edge of the board as viewed facing the edge connector, to the leftmost position.

2. Potentiometer-controlled gain - The output power from each leg of a coupler is rarely uniform. Variations in the modulation depth, splice losses, bending losses and modulation losses all reduce the light emitted from each fiber. Since the demodulator algorithm assumes equal power from each leg, potentiometers have been installed to provide adjustment of the amplitude of the AC portion of each input signal. Adjustments of the DC portion may also be accomplished. The potentiometers are blue in color and are located just in from the left-hand edge of the board as viewed facing the edge connector. The output of each amplifier may be monitored by connecting an oscilloscope lead to the test point loops near the yellow jumpers and aligned with the transverse axis of the board. These test points are connected to pin 5 of the non-inverting amplifiers (ICs U4-U6 of Figure B1).

B. INTERMEDIATE AMPLIFIERS AND OUTPUT BUFFERS

1. Intermediate Amplifiers

The intermediate amplifiers have been included to permit adjustment of the signal level to the remainder of the circuit. The gains of these non-inverting amplifiers are selected via the yellow jumpers towards the left edge of the board, as viewed facing the edge connector. The gains permitted are 20, 30, and 40 dB, using pairs of jumper leads, right to left as viewed facing the edge connector. The signal levels at this point in the circuit may be monitored using the test loops adjacent to these intermediate amplifiers, aligned with the longitudinal axis of the board.

2. Output Buffer Amplifiers

For convenience in recording and monitoring requirements, the intermediate amplifier outputs are also connected via buffer amplifiers (U8A, U8B, and U8C in Figure B1) to the lower row of BNCs available on the front panel. These correspond to channel

numbers 1-3 (as numbered on the left hand edge of the board) from left to right, viewed facing the front panel.

C. MODULATION DEPTH ADJUSTMENT

The modulation depth detected in each fiber has been observed to vary slightly between legs. Adjustment of the AC portion for equal signal level between channels also changes the DC portion of the signal. A set of summing amplifiers has been included to remove the DC portion of the signal. This approach an alternative to high-pass filtering the input signal since sub-radian interferometric signals contain DC. This approach has proven successful, provided that the ratio of modulation depth variations between channels remains constant. Changes in the ratios of 3×3-coupler outputs seems to cause problems. Investigation of the demodulator performance is required to address interchannel variations.

The adjustment to remove the DC portion of the signal is made via the potentiometers (tan colored) near the middle of the board. The effect of this adjustment to each channel can be monitored using the test loops under the differentiator resistors (mounted on component towers in the middle of the board). The signals at these test points should be adjusted such that they have equal AC amplitudes and zero DC component. Adjustment to correct discrepancies should be performed using the input amplifier potentiometers (blue) first and then the modulation depth potentiometers (tan).

D. DIFFERENTIATOR ADJUSTMENT

The signal presented to the multiplier sections should be as large as possible without distortion (10 V). To this end the differentiator transfer function at the highest frequency of interest should be unity. The resistors mounted on the component headers permit adjustment of this transfer function. In this implementation 40.2 kΩ resistors are fitted,

69

corresponding to an upper frequency of interest of approximately 40 kHz, as computed in the following formula.

$$\frac{1}{2\pi RC} = \frac{1}{2\pi(40.2\ k\Omega)(100\ pF)} = 39.6\ kHz, \tag{B1}$$

E. PERFORMANCE

Reference 9, Chapter XI, details the performance of the first implementation of the symmetric analog demodulator (SAD); Reference 9 also details a digital implementation of an *Asymmetric* Digital Demodulator. Following the analysis of Reference 9, page 161, the analog interferometric simulators were used to provide inputs to the SAD V2.1. This removes the added noise due to laser phase and the wandering or drift of the polarization of the optical waves in the interferometer, the major cause of drift in amplitude of the interferometric signal. The *Scale Factor* of the demodulator is defined as the ratio of the demodulator output voltage modulation amplitude to the phase modulation amplitude of the input interferometric signals.

The phase noise for the demodulator at 5 kHz was measured as 6.33 μrad/$\sqrt{Hz}$. The average phase noise spectral density of the three analog interferometric simulators was measured at 1 kHz to be 0.48$\pm$0.005 μrad/$\sqrt{Hz}$ [Reference 15, book 1, page 19] and although not measured at 5 kHz is still far enough below the phase noise floor of the demodulator that it would not be of the order of the demodulator noise at 5 kHz. Thus the demodulator noise measurement can be mostly attributed to the demodulator itself. The dynamic range at 5 kHz was determined for maximum signal (4% THD) to be:

$$\frac{47\ rad}{6.33\ \mu rad} = 7.4 \times 10^6 \tag{B2}$$

$$\text{Dynamic Range at 5 kHz} = 20\log(7.4 \times 10^6) = 137\ dB.$$

APPENDIX C. DEMONSTRATION WITH ANALOG ELECTRONICS

Prior to an optical system demonstration a single channel demonstration of the multiplexing technique was attempted for proof of concept purposes. Since a demonstration with only a single interferometric output from the 3×3-coupler was attempted, the demodulation of the interferometric signals could not be carried out. The essence of this experiment was that if the ratios of the demultiplexed components of the interferometric signal and the original signal remained constant throughout the various steps of frequency translation, then one could conclude that the technique was feasible. That is to say, if the fundamental and significant higher order harmonics, which are greater than the noise floor, were in the same ratios as the original interferometric signal, demodulation would produce the same output phase modulation for both the baseband and the demultiplexed signals. Further, the demonstration did not quantify the effects of the loss of higher order harmonics (as a result of the multiplexing scheme). The effect would be extremely small but could be quantified in terms of the amount of energy lost between the baseband signal and the demultiplexed signal. This is easily computed from the fact that the energy contained in the interferometric signal that can be demodulated is the sum of the amplitude squared values of all of the components (Parseval's theorem). By calculating the energy before and after multiplexing, and the energy lost, a reasonable estimate of the effect of the distortion from the demodulated signal can be made. It will be shown later that this effect is small. For low level signals however, it provides a lower limit on the level of signal which can be demodulated, i.e., the minimum detectable signal. This analysis assumes that dispersion of the higher order harmonics is minimal, i.e., the higher order harmonics are integral multiples of the fundamental.

Another aspect of the demultiplexing technique not covered in this demonstration is the effect of filtering on the interferometric signal prior to demodulation. This was not considered since filter theory is well understood and documented, and the only requirements to ensure successful demodulation are constant gain and phase over the pass band of interest. This passband of interest is the interferometric signal significant bandwidth f_{sb} discussed earlier (section II B.1.).

The equipment setup for the demonstration is shown at Figure C1.
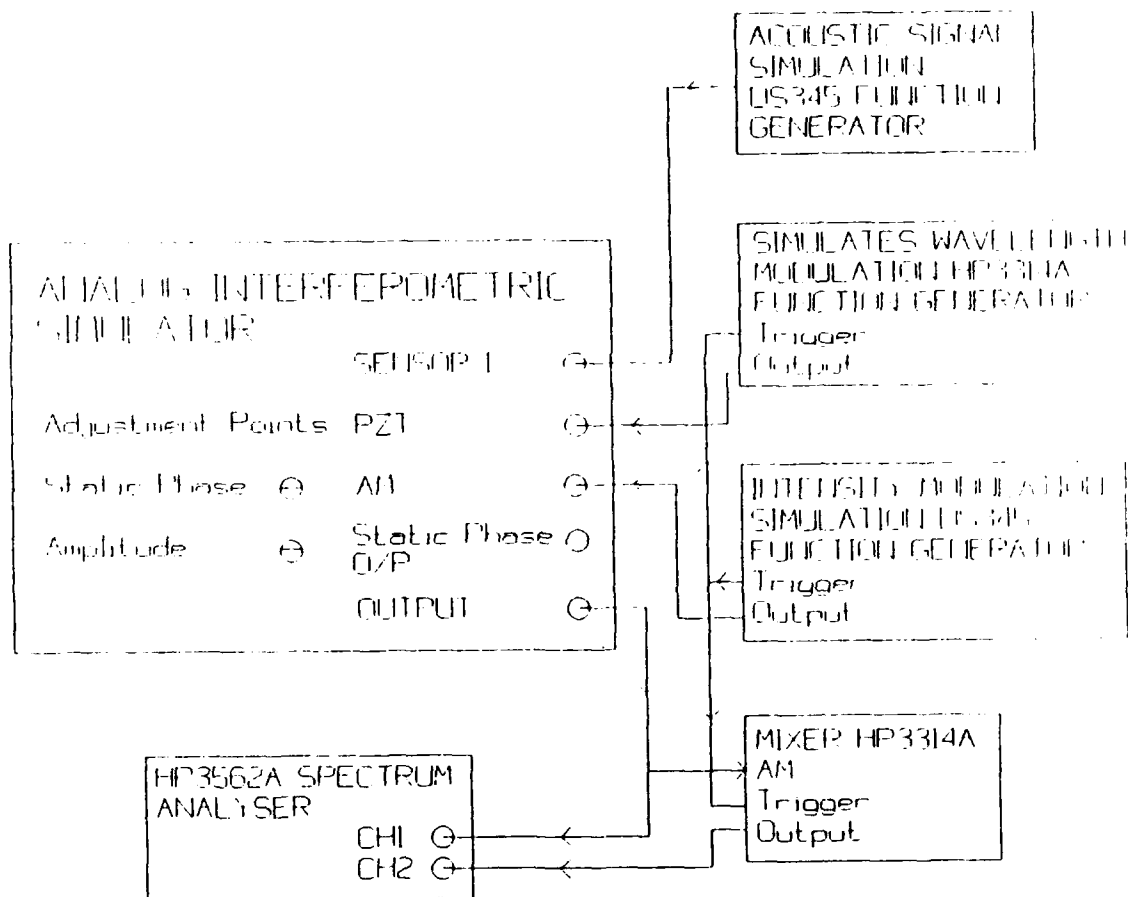
Figure C1. Equipment Setup for Analog Electronics Demonstration.

The setup has three separate function generators to simulate the acoustic signal from the sensor and wavelength and intensity modulation from the laser source. The wavelength modulation is phase and frequency locked to the intensity modulation of the source via appropriate operation of the triggers of the respective function generators. Another function generator is utilized as the demultiplexer or mixer by appropriate use the AM input. The outputs were monitored by a HP3562A spectrum analyzer.

A. ANALOG INTERFEROMETRIC SIMULATOR

The analog interferometric simulator is similar to that described at Reference 9, Appendix C. A modification was conducted so that the input previously labeled SENSOR 2 is now labeled STATIC PHASE O/P and provides an easier way to measure the static phase drift angle ϕ_{drift}. Previously this was determined using Lissajous figures [Reference 20, pages 30-39] and making appropriate measurements [Reference 9, Appendix C, section B, pages 301-2]. The drift angle term in the simulator is not time-varying as it would be in an actual system but a constant set on the front panel via the static phase adjustment.

The modified simulator block diagram is shown in Figure C2 while the circuit is shown in Figure C3. The static phase measurement calculations will be presented by isolating that part of the circuit involved; see Figure C4.

73
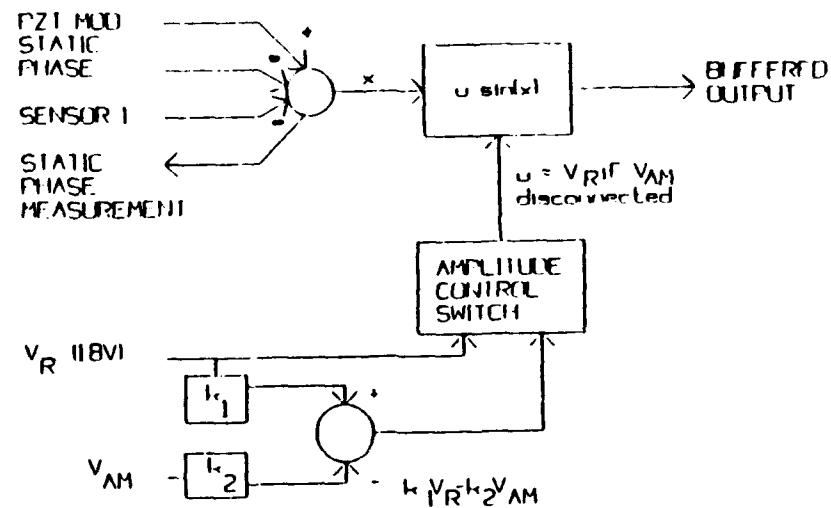
Figure C2. Modified Analog Interferometric Signal Simulator Block Diagram.
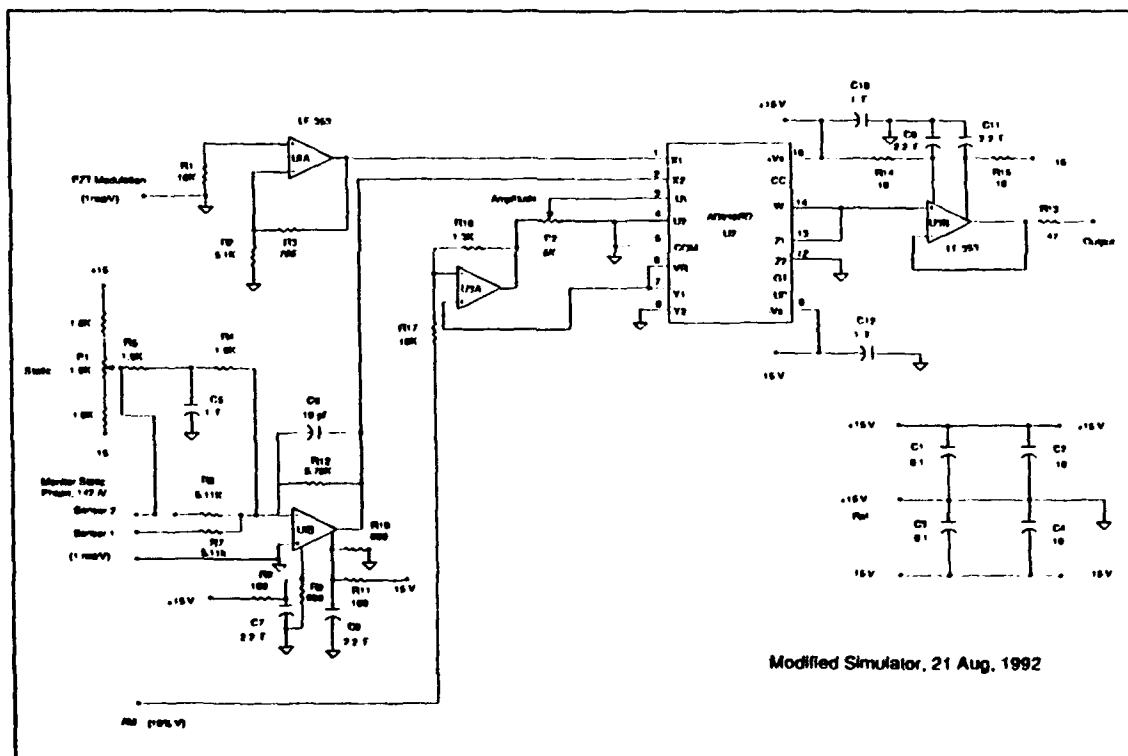

Figure C3. Modified Analog Interferometric Signal Simulator Circuit Diagram.

The Analog Devices AD639 Universal Trigonometric Function Converter is configured to produce the sine of its input. A one-volt input is equivalent to an input argument of 50°. Thus the gain G of the circuit of Figure C4 is:

$$G = \frac{5.7}{2} = 2.85. \qquad (C.1)$$

Thus the static phase adjustment input equates to:

$$2.85 \times 50°/\text{Volt} = 142°/\text{Volt}, \qquad (C.2)$$

so that, with one simulator adjusted to zero volts static phase output and the other two static phase outputs adjusted to ±0.845 V, we obtain our three interferometric signals symmetrically phase shifted 120° relative to each other.
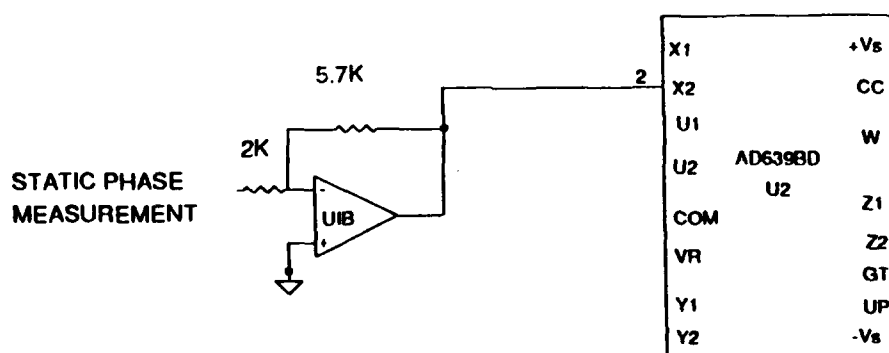
Figure C4. Circuit for Static Phase Measurement Calculations.

75

B. RESULTS

The first test verified that the modulated components were in the same ratio as the baseband components. The input labeled *PZT MOD* in Figures C1 and C2 was grounded to simulate the absence of wavelength modulation. The static phase was set at 120° (0.845V static phase output) to ensure that both even and odd harmonics would be present in the interferometric signal. A 1 kHz sine wave was applied to the *SENSOR 1* input to generate an interferometric type signal. The amplitude was varied and the ratios of baseband components and modulated components were observed to 'track' each other. A plot of a 4.2 V_{pp} amplitude ($\phi_s \cong 2.1$ radians from simulator scale factor of 1 rad/V) is shown at *Figure C5 with the upper waveform showing the baseband 'interferometric signal'* prior to multiplexing, and the lower signal showing the amplitude modulated and demultiplexed version.
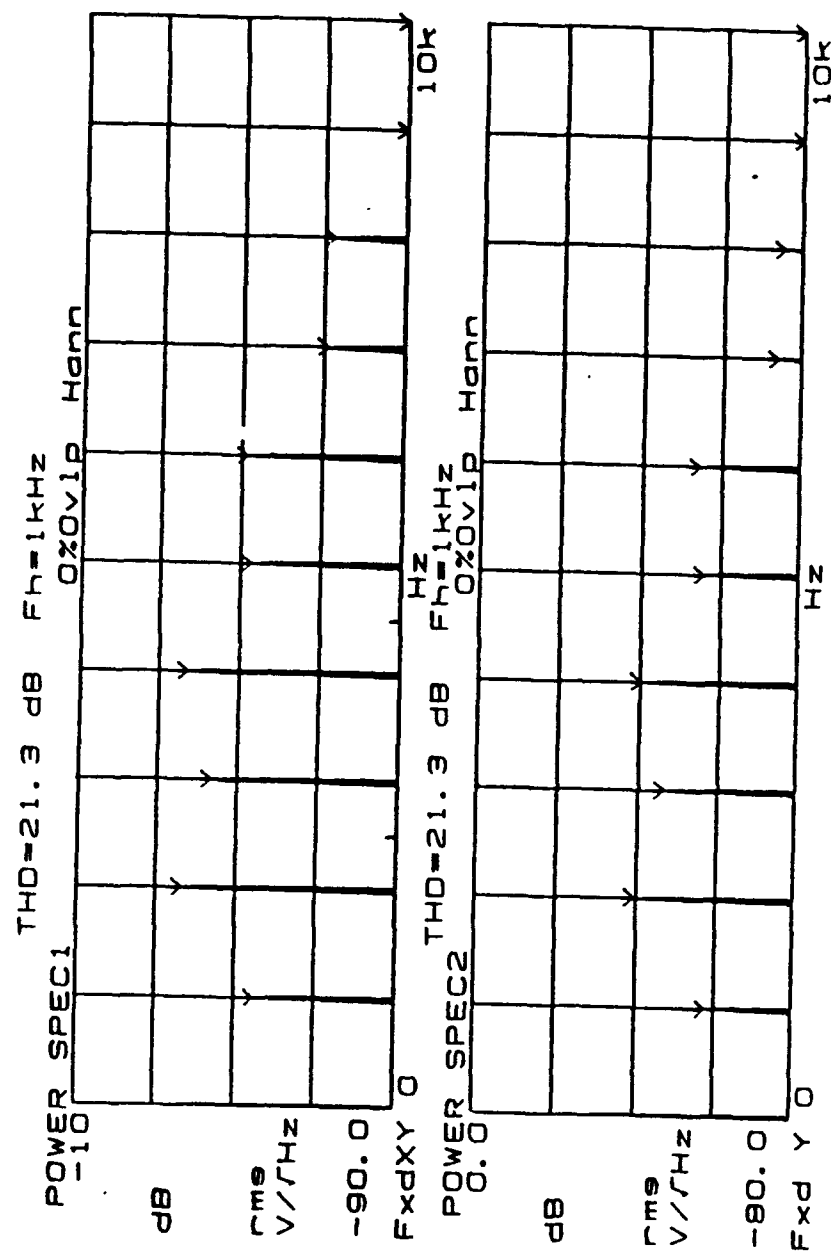
Figure C5. Spectrum of baseband simulated interferometric signal (top) and
spectrum of demultiplexed version of same interferometric signal
(bottom).

77

It can be seen that signal and demultiplexed components are indeed in the same ratios even though the amplitudes are different .

Figure C6 shows the Lissajous pattern for the demultiplexed output (x axis) and the simulated interferometric signal output (y axis) with no wavelength modulation (PZT MOD input grounded). This also verifies that the signals are in the same phase and of the same shape, i.e., the component ratios are the same. The closed ellipse or nearly straight line offset at 45° indicates a zero phase difference. The total harmonic distortion *THD* is the same for both waveforms. The THD together with Figure C5 also provides a crude measure of the ratios of components.

The HP3562A Spectrum Analyzer calculates the THD by calculating the ratio of energy in the fundamental component to the sum of the other components. Thus while it is possible to have the components in different ratios and the same THD, it is not possible to have them in different ratios and the same THD.
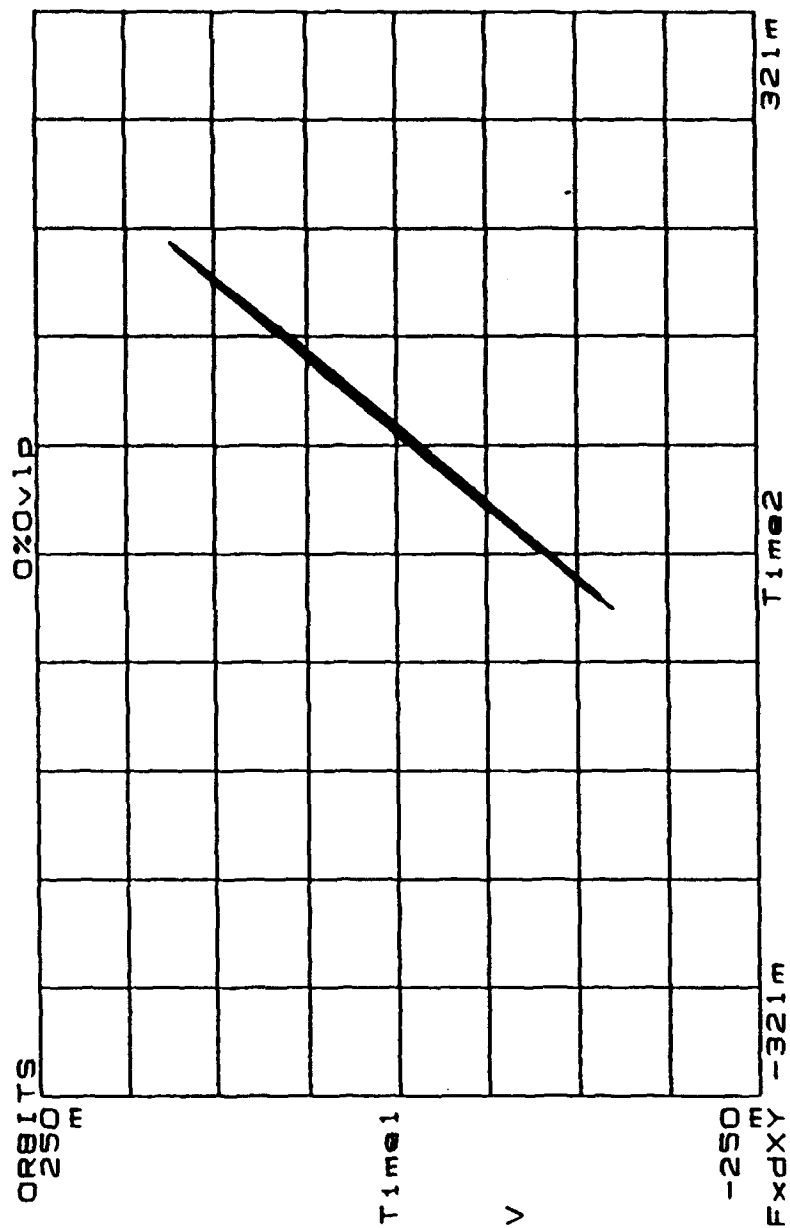
Figure C6. Lissajous pattern for demultiplexed output (x axis) and the modulated simulator output (y axis) with no wavelength modulation.

Wavelength modulation of the source is simulated by a variable amplitude signal locked in phase and frequency to the modulation frequency connected to the PZT MOD input. This wavelength modulation was not included in Equation 1.3 (where it was presumed negligible). Equation 1.3 is rewritten below with the wavelength modulation included.

$$u = A + B\cos\left(\phi(t) + \phi_{drift}(t) + \phi_c + \phi_m \sin \omega_m t\right). \tag{C.3}$$

Hence ϕ_m represents the amount of wavelength modulation. Figure C7 shows the Lissajous pattern for the case where $\phi_m = 0.42$ radians for an 'acoustic' signal of 2.12 radians amplitude at 1 kHz signal and a modulation frequency $f_m = 20$ kHz. This clearly shows that the two signals are no longer in phase (open ellipse) or the same shape (seen as the jagged shape of the outside of the ellipse). This is further highlighted by Figure C8 where the THD ratio and component ratio are no longer the same.

This change highlights the difference between this multiplexing scheme and the presently popular wavelength modulated frequency division multiplexing (WM-FDM). WM-FDM is more commonly referred to as phase generated carrier (PGC) [Reference 5, section 11.4.2.2, pages 360-2 and Reference 1, volume II, section 14.6.5, pages 564-5]. While WM-FDM seeks to maximize the wavelength modulation and to reduce the intensity modulation, our technique AM-FDM operates optimally with no wavelength modulation.

The analog electronics demonstration showed that the multiplexing technique will work provided that wavelength modulation is not significant. The extent to which the proposed multiplexing technique will work with increasing or decreasing wavelength

modulation has not been studied. When the amount of wavelength modulation, ϕ_m, is approximately 3% of the signal amplitude, ϕ_s, the Lissajous pattern starts to change from a line to form an open ellipse.
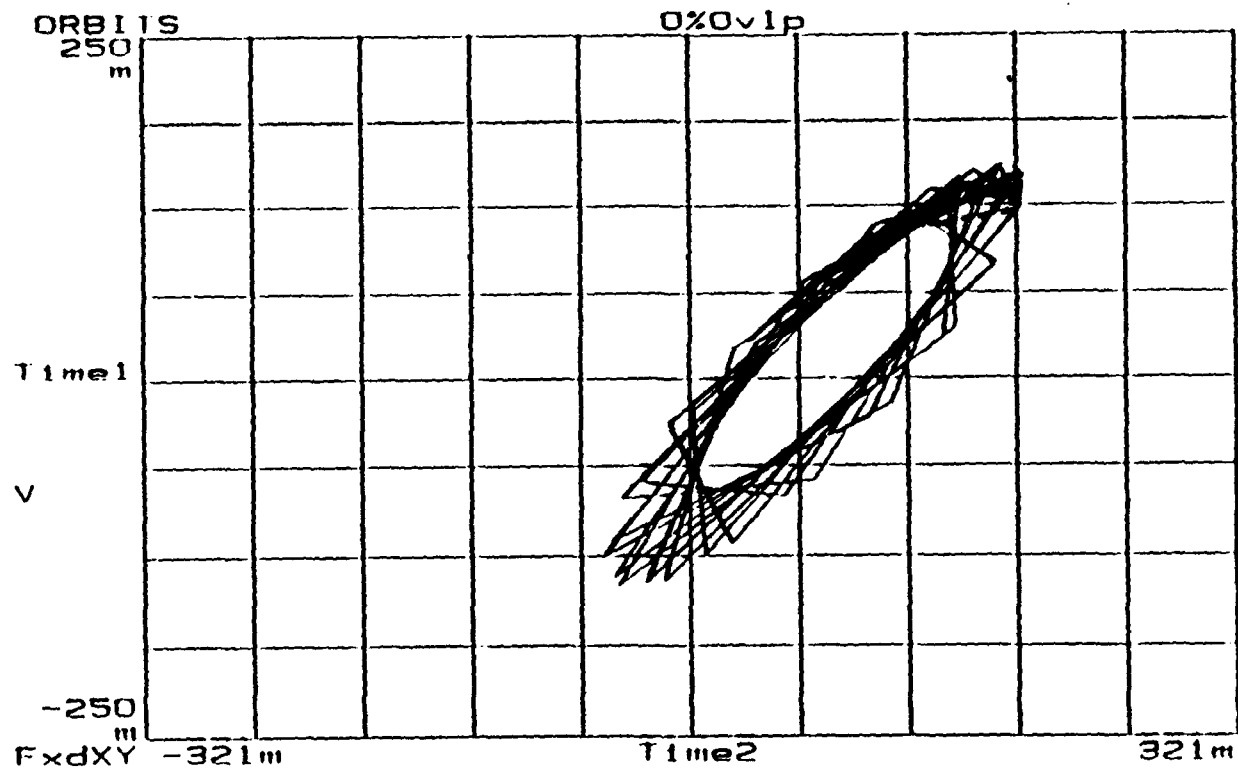

Figure C7. Lissajous pattern for same signal as Figures C5 and C6 with 30% wavelength modulation ($\phi_m = 0.300$ rad).
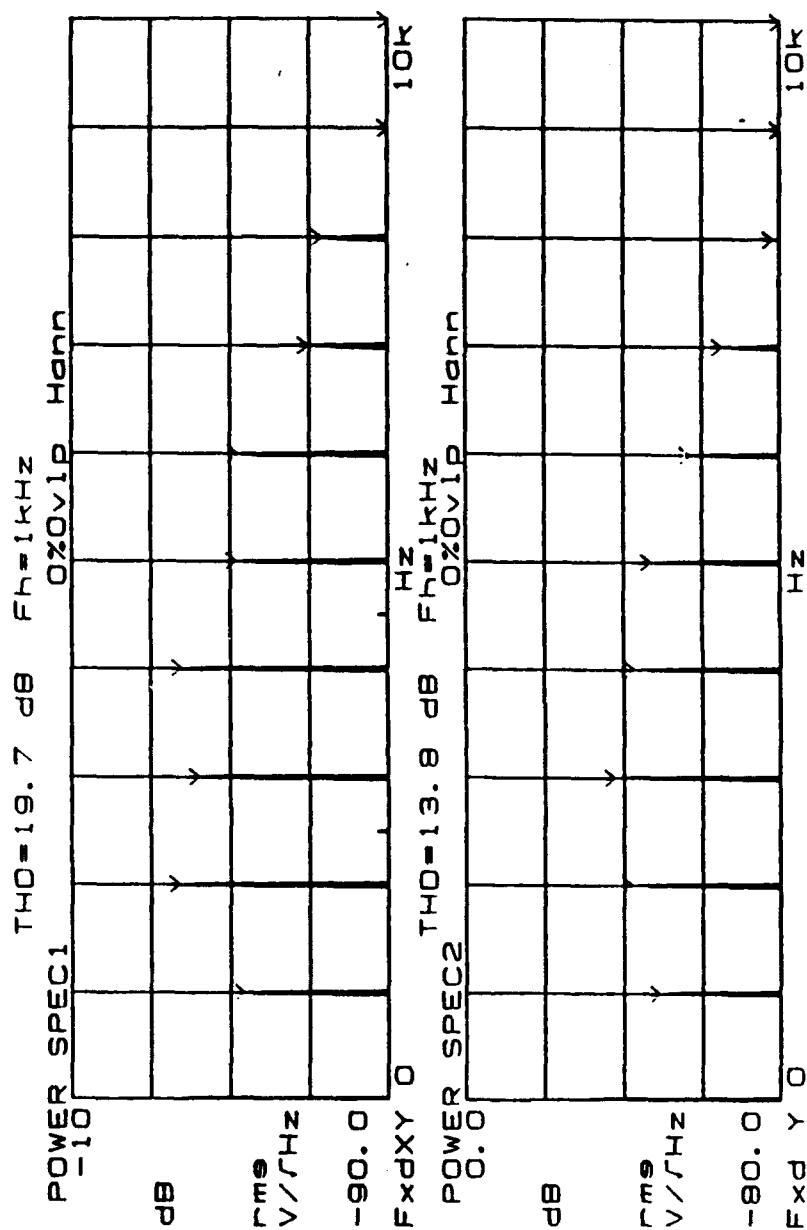
Figure C8. Spectrum of signals of Figure C7 (with wavelength modulation); baseband interferometric signal (top) and spectrum of demultiplexed version of same interferometric signal (bottom).

APPENDIX D. MISCELLANEOUS

This appendix contains the following:

- MATLAB™ routines written by the author for this thesis.

- THB292 22 kHz integrated active filter response.

- Operating curves and data sheets for lasers used in this thesis.

- Benchtop Interferometer Figure.

- ORTEL™ information sheet on device linearity specifications.

- Noisefloor Figures for Analog Interferometric Simulator and Mixing circuit.

The MATLAB™ routines are provided with no guarantee of results obtained i.e., the author disclaims any errors in the code reproduced.

MATLAB™ routine used for Chapter II figures.

```
% Thesis - Mixing of interferometric signal simulation
clear;clg;

fs1=1000;phis1=3*pi/2;phid1=pi/4;
fs2=600;phis2=pi;phid2=0;
fm1=40000;
fm2=60000;
phis=pi;

% phid is the drift phase term for the difference in optical path length
% between the two legs of the interferometer
%phid=input('Enter phid (in radians)  ');
t=0:(10/(fs1*32767)):(10/fs1);
%t=0:(10/(fs*32767)):(10/fs);
m=0.75;
I1=(1+(cos(phis1*sin(2*pi*fs1*t)+phid1))).*(1+(m*sin(2*pi*fm1*t)));
I2=(1+(cos(phis2*sin(2*pi*fs2*t)+phid2))).*(1+(m*sin(2*pi*fm2*t)));
I3=(I1+I2);
I=I3.*sin(2*pi*fm1*t);

F=fft(I,32768);
f=0:1/max(t):32767*1/max(t);
fk=f./1000;

subplot(211),plot(fk(1:1200),20*log10(abs(F(1:1200)))),grid
xlabel('Frequency (kHz)'),ylabel('Magnitude (dB)')
axis([0 fk(1200) 0 100]);
```

MATLAB™ routine used for Chapter III figures.

```
%Thesis calculations for MxN array

clear;clg;
N=input('Enter # of sensors N ');
M=input('Enter # of sensors M ');

for i=1:N

        I(i)=((1-1/N)*(1-(i)/N)+1/N)/ 1.230268770812;
        c(i)=((1-1/N)/N)/((1-1/N)*(1-i/N)+1/N);
        pk(i)=I(i)*c(i);
        pk1(i)=0.003*I(i)*c(i);
end
c'
fdB=10*log10(ones(N,1)-c')
pkdb=10*log10(pk);pk1db=10*log10(pk1);
%c1=flipud(c(1:length(c)-1)');
%I1(1)=pk(1);

%for j=2:length(c)-1
%       I1(j)=(c1(j-1)*I1(j-1));
%end

for i=1:M

        Im(i)=((1-1/M)*(1-(i)/M)+1/M)/1.145512941446;
        cm(i)=((1-1/M)/M)/((1-1/M)*(1-i/M)+1/M);
        %pk(i)=I(i)*c(i);
        %pk1(i)=0.003*I(i)*c(i);
end
cm'
fdBm=10*log10(ones(M,1)-cm')
%pkdb=10*log10(pk);pk1db=10*log10(pk1);
c1=flipud(cm(1:length(cm)-1)');
I1(1)=pk1(1);

for i=2:length(cm)
        I1(i)=(c1(i-1)*I1(i-1));
end
I1dB=10*log10(I1);

figure(1)
plot(I,'o')
ylabel('Fractional Power Input Pin/Ptotal')
xlabel('Sensor # N'),grid
```

```
figure(2)
plot(c,'o'),ylabel('Coupler Ratio')
xlabel('Coupler # (N-1  total)'),grid
axis([0 N 0 0.6])

figure(3)
plot(fdB,'o'),ylabel('Coupler Ratio (dB)')
xlabel('Coupler # (N-1 total)'),grid
axis([0 N -5 0])

figure(4)
plot(pkdb,'o')
ylabel('Power to Sensor N Pn/Ptotal (dB)')
xlabel('Sensor # N'),grid

figure(5)
plot(pk1db-2.04,'o'),ylabel('Power from Sensor N Po=3mW (dBm)')
xlabel('Sensor # N'),grid

figure(6)
plot(c1,'o'),grid
ylabel('Coupling Ratio'),xlabel('Coupler # (M-1 total)')

figure(7)
plot(l1dB-2.04,'o'),grid
ylabel('Power at Sensor M (dB)'),xlabel('Sensor # M')
```

MATLAB™ routine used for figure A2.

```matlab
% Interferometric Signal Simulation
%
% for A/B=1 I(t)=1+cos[ phis (sin[omegas t] + phid) ]
%
clear,clg;
fs=1000;

% phis is the amplitude of the signal of interest

phis=input('Enter phis (in radians) ');
%phis1=input('Enter phis1 (in radians) ');
%phis2=input('Enter phis2 (in radians) ');

% phid is the drift phase term for the difference in optical path length
% between the two legs of the interferometer
phid=input('Enter phid (in radians) ');
phid1=input('Enter phid (in radians) ');
phid2=input('Enter phid (in radians) ');

t=0:(10/(fs*32767)):(10/fs);
I=1+(cos(phis*sin(2*pi*fs*t) +phid));
I1=1+(cos(phis*sin(2*pi*fs*t) +phid1));
I2=1+(cos(phis*sin(2*pi*fs*t) +phid2));

F=fft(I,16384); F1=fft(I1,16384); F2=fft(I2,16384);
f=0:2/max(t):16383*1/max(t);

subplot(221),plot(t(1:length(t)/1000:length(t)/5),I(1:length(t)/1000:length(t)/5)),grid
xlabel('Time (sec)'),ylabel('Intensity')
axis([0 f(70) 0 100]);
subplot(222),plot(f(1:400),20*log10(abs(F(1:400)))),grid
xlabel('Frequency (Hz)'),ylabel('Magnitude (dB)')
subplot(223),plot(t(1:length(t)/1000:length(t)/5),I1(1:length(t)/1000:length(t)/5)),grid
xlabel('Time (sec)'),ylabel('Intensity')
axis([0 f(70) 0 100]);
subplot(224),plot(f(1:200),20*log10(abs(F1(1:200)))),grid
xlabel('Frequency (Hz)'),ylabel('Magnitude (dB)')
pause
clg;

subplot(221),plot(t(1:length(t)/1000:length(t)/5),I2(1:length(t)/1000:length(t)/5)),grid
xlabel('Time (sec)'),ylabel('Intensity')
pause
axis([0 f(70) 0 100]);
subplot(222),plot(f(1:4000),20*log10(abs(F2(1:4000)))),grid
xlabel('Frequency (Hz)'),ylabel('Magnitude (dB)')
```
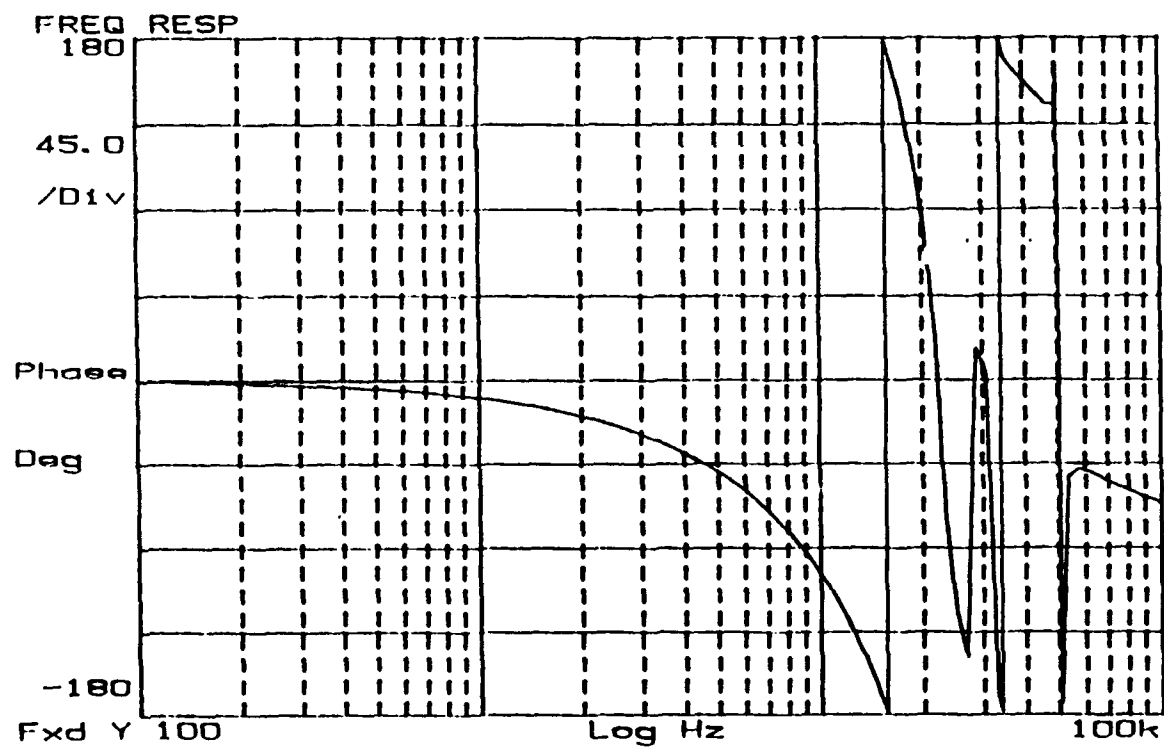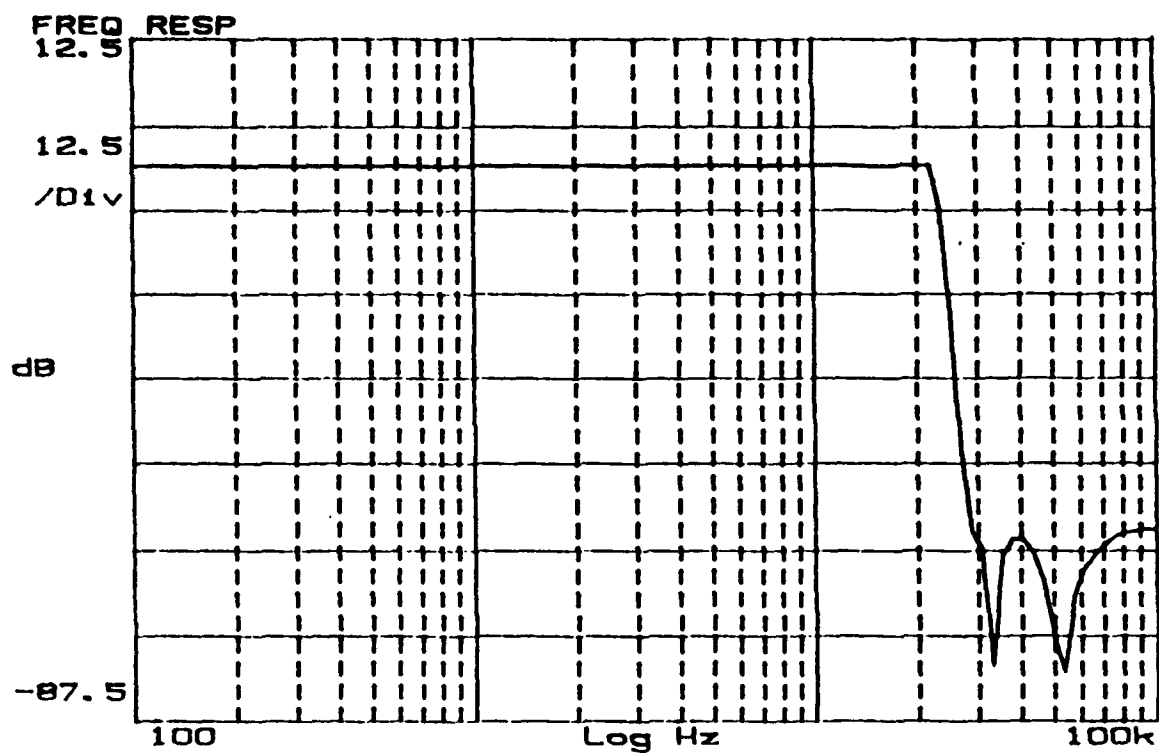
Figure D1. Frequency response of integrated active lowpass filter type THB292
[Reference 13, page 118].

88

SEASTAR OPTICS INC

LASER DIODE TEST DATA

Model No.: PT450L930

Serial No.: SP2676

Wavelength: 833 nm

Laser Type: SHARP LT015MDO

Rated Po: 3435 micro W

Date tested: Aug 21, 1992

Tested by: _[signature]_

POWER OUTPUT VS. FORWARD CURRENT

PIN CURRENT VS. OUTPUT POWER
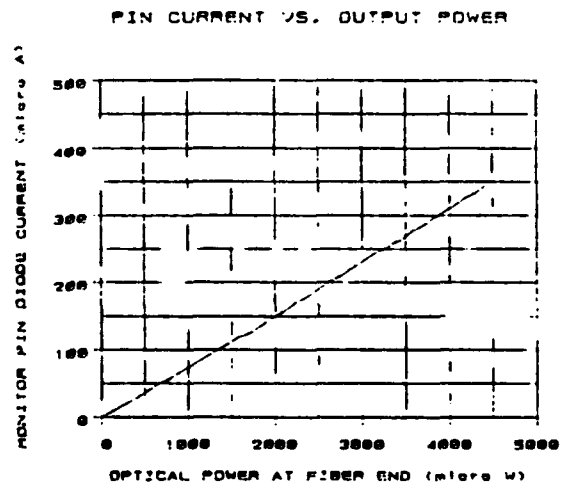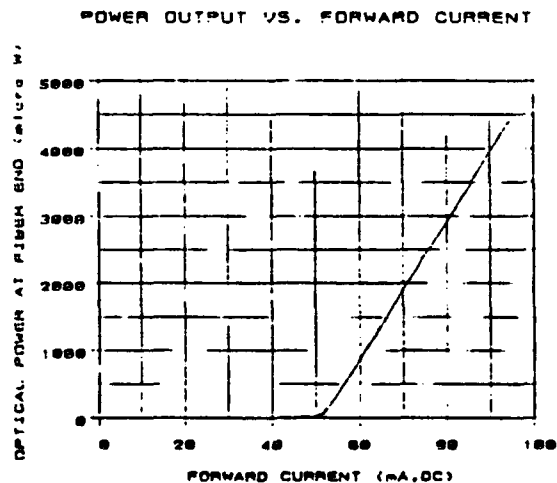
Figure D2. Seastar Laser #SP2676 Manufacturer's test data.

89

Seastar Laser #SP2676
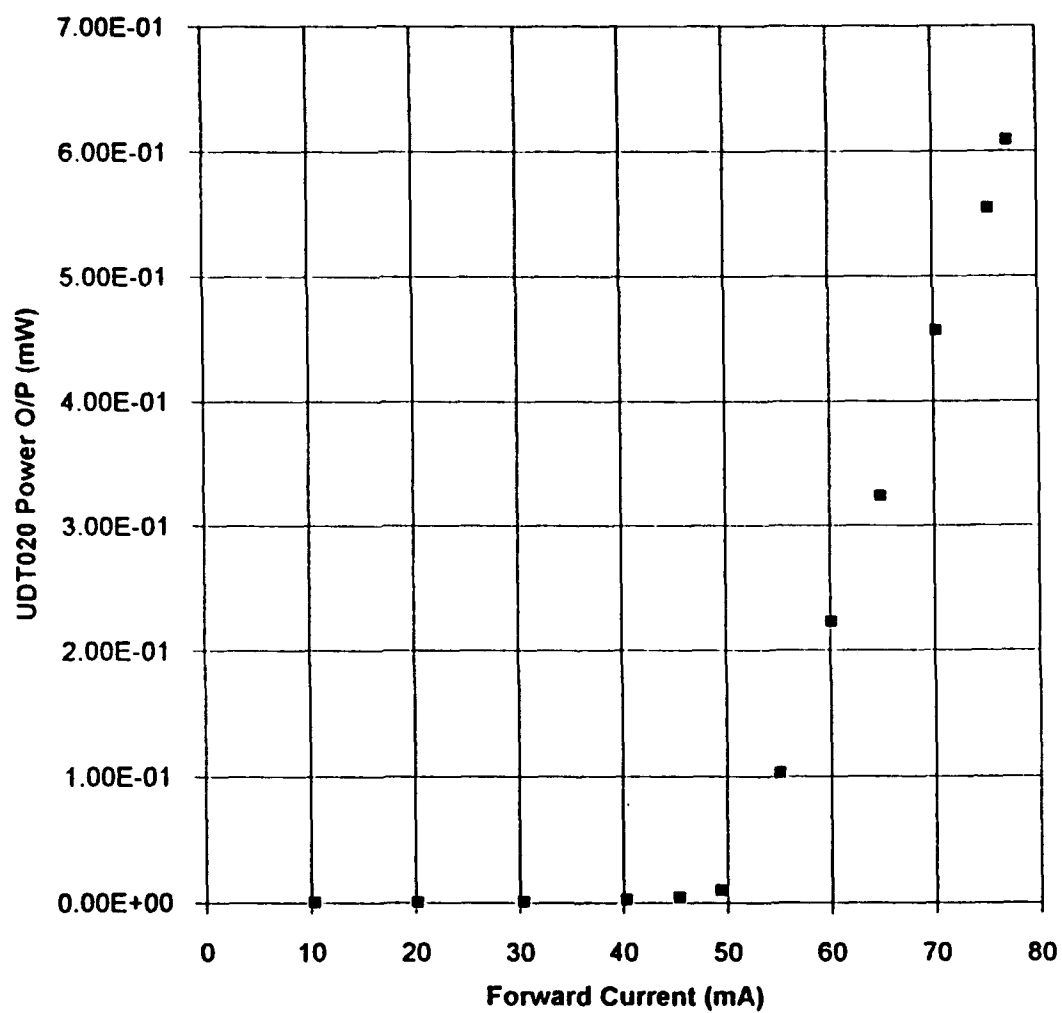
Figure D3. Seastar Laser #SP2676 measured operating curve.

90

LASER DIODE TEST DATA

Model No.: PT-450

Serial No.: 1320

Wavelength: 830 nm

Laser Type: HITACHI HL8312G

Rated Po: 1437 micro W

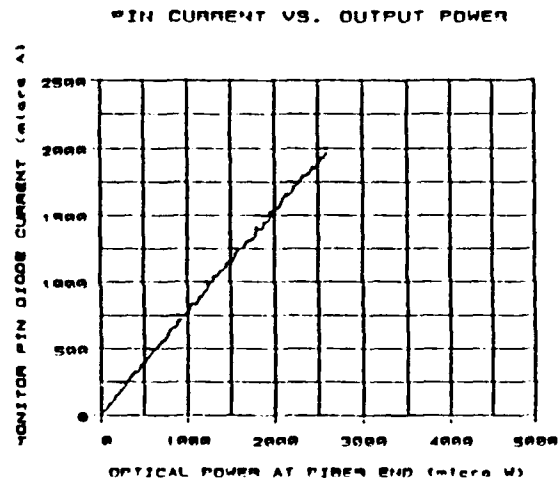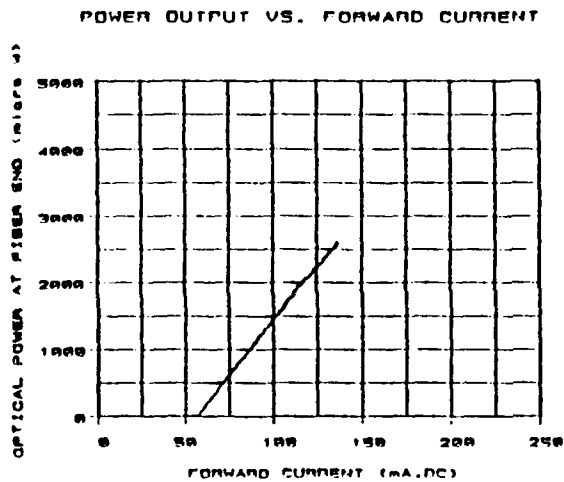Date tested: Nov 7, 1989

Tested by: *Howard L.*

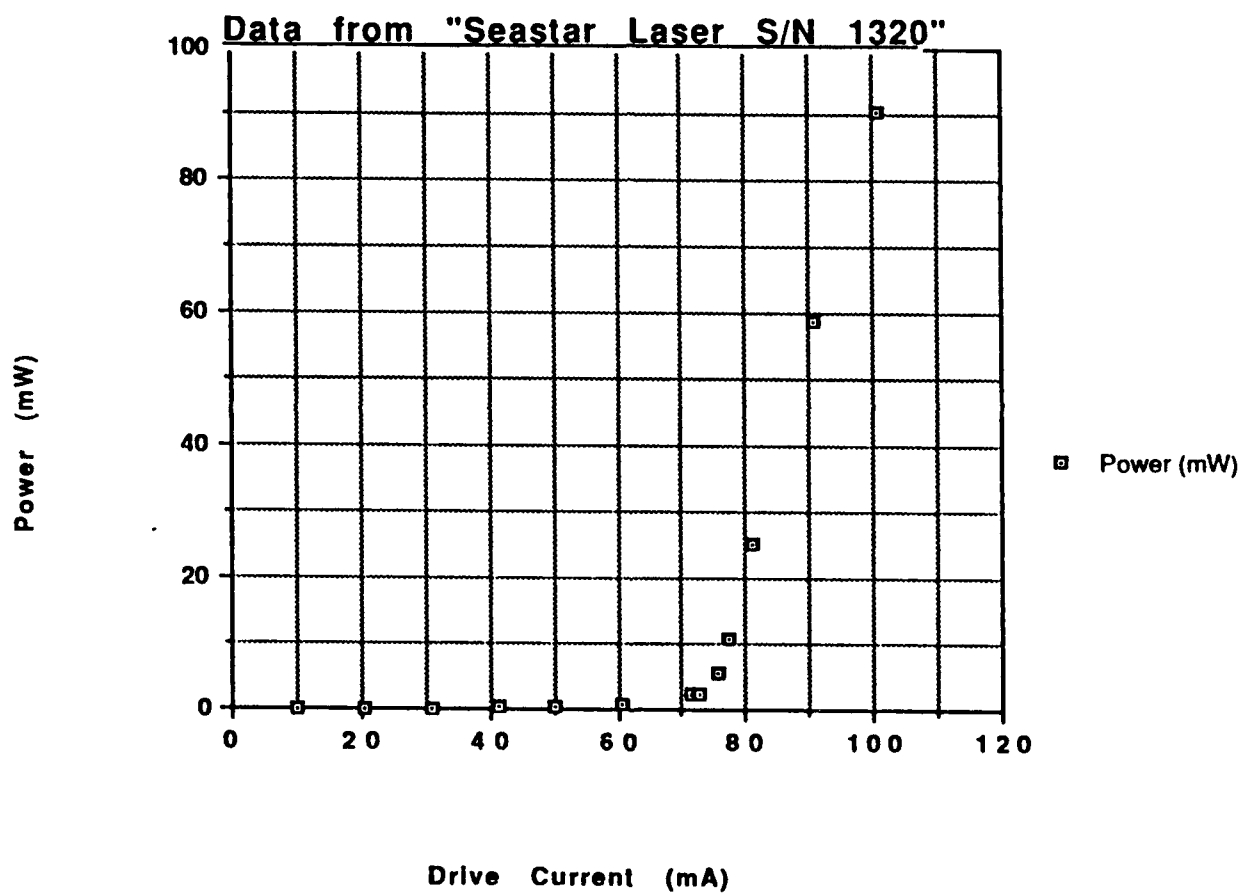Figure D4. Seastar Laser #SP1320 Manufacturer's test data.

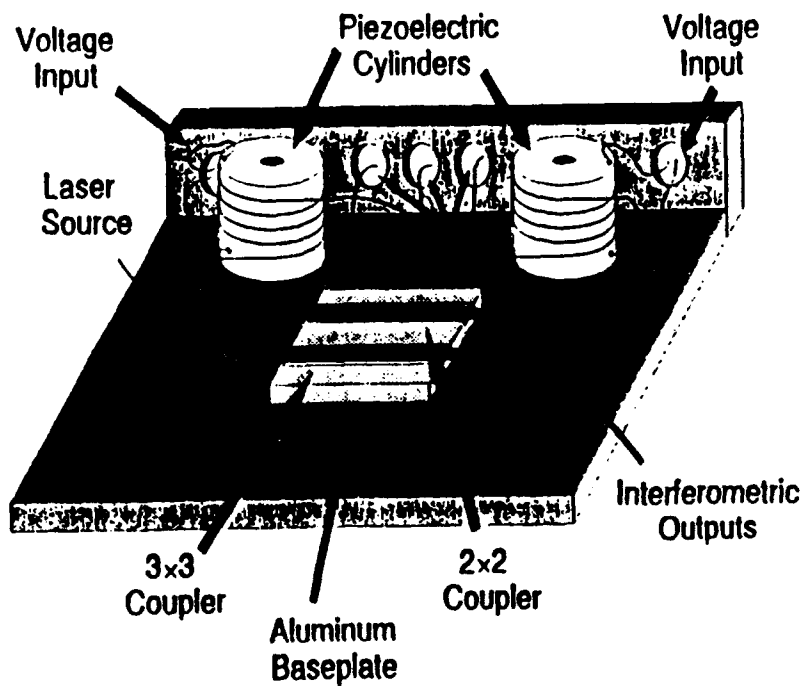**Figure D5. Seastar Laser #SP1320 measured operating curve.**

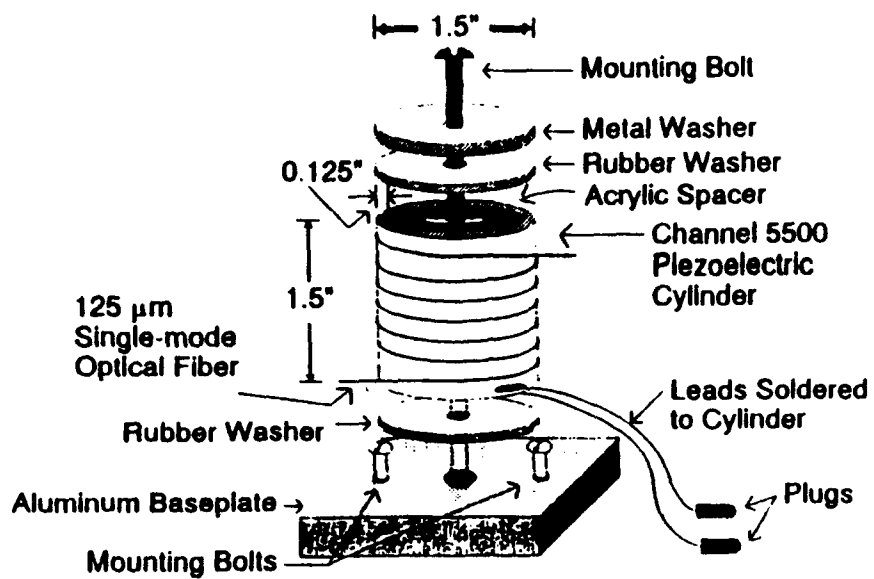**Figure D6. Benchtop Interferometer (after Reference 9).**
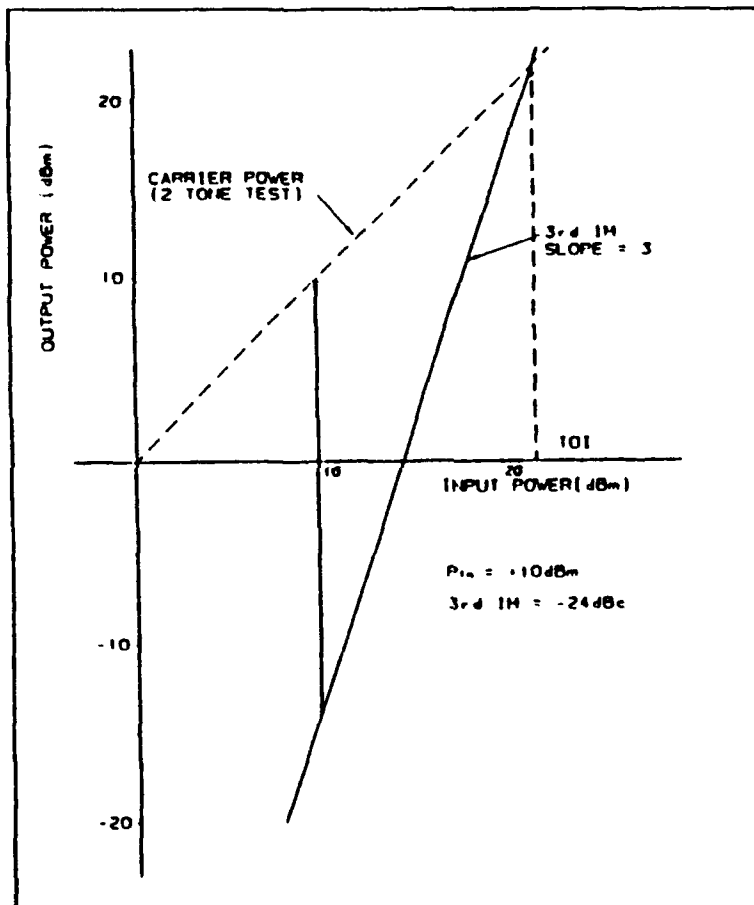
Figure 21
Third Order Intermodulation Products and Third Order Intercept Linearity - Two Tone Test

For a "well behaved" RF device the third order intermodulation products will be twice as much below the carrier level as the carrier is below the input third order intercept point (TOI).

Figure D7. ORTEL™ device linearity specifications.

94

Figure D8. Noisefloor for Analog Interferometric Simulator.

95

Figure D9. Noisefloor for Mixing circuitry (Analog Interferometric Simulator connected).

INITIAL DISTRIBUTION LIST

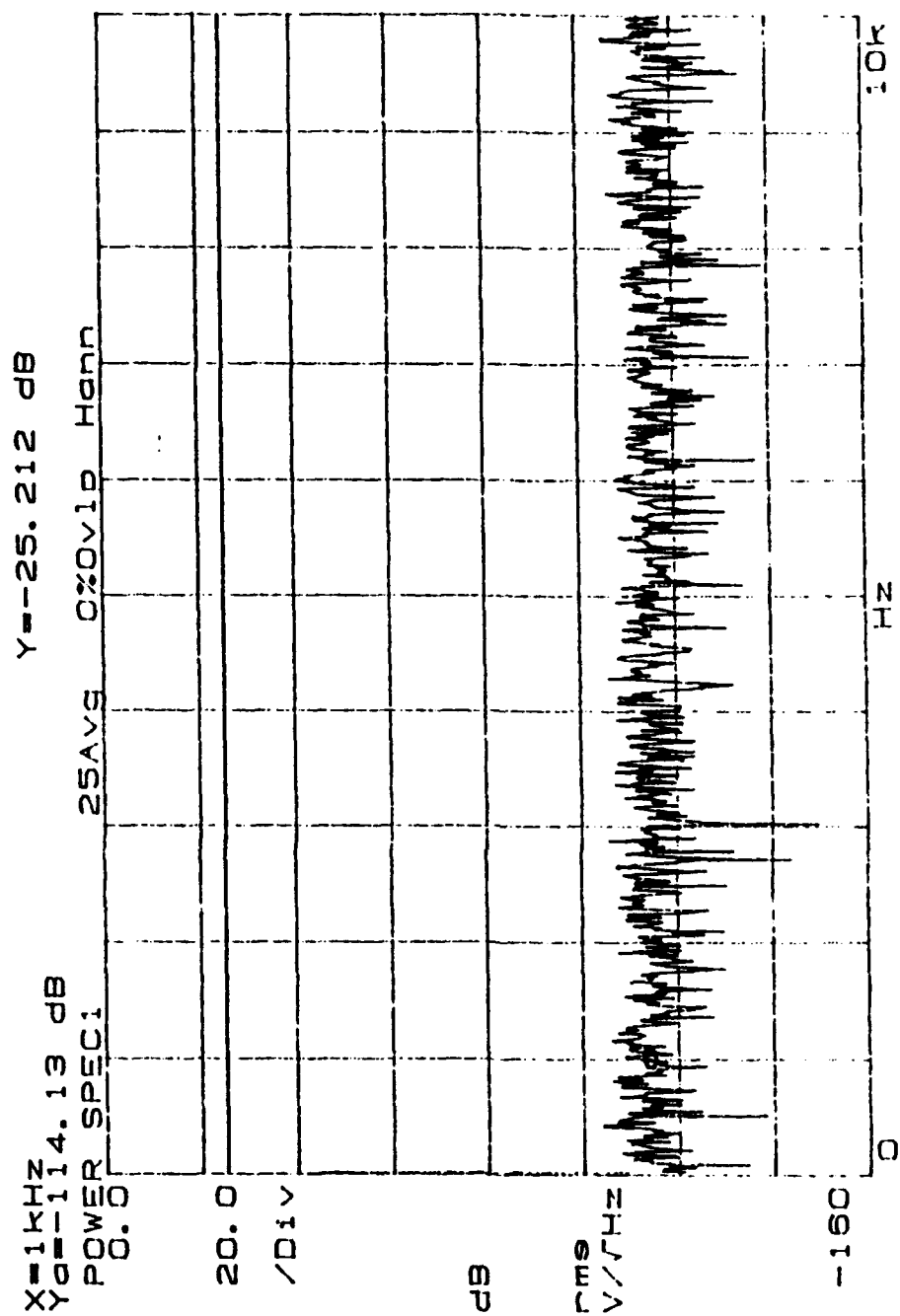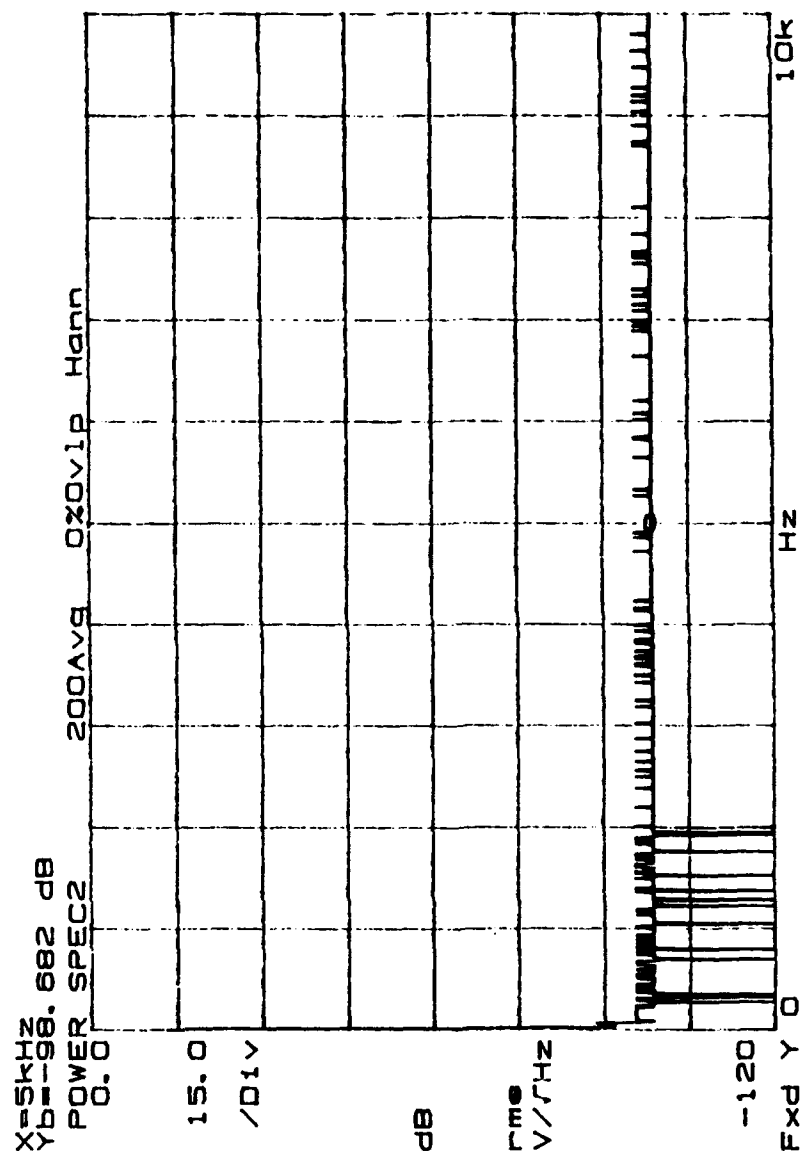1. Defense Technical Information Center   2
   Cameron Station
   Alexandria, VA, 22304-6145

2. Library, Code 52   2
   Naval Postgraduate School
   Monterey, CA 93943-5101

3. Prof. A. A. Atchley, Code PH/Ay   1
   Physics Department
   Naval Postgraduate School
   Monterey, CA 93943-5000

4. Chairman, Code EC   1
   Electrical and Computer Engineering Department
   Naval Postgraduate School
   Monterey, CA 93943-5121

5. Prof. David A. Brown, Code PH/Br   6
   Physics Department
   Naval Postgraduate School
   Monterey, CA 93943-5000

6. Prof. J. P. Powers, Code EC/Po   1
   Electrical and Computer Engineering Department
   Naval Postgraduate School
   Monterey, CA 93943-5121

7. Prof. S. L. Garrett, Code PH/Gx   1
   Physics Department
   Naval Postgraduate School
   Monterey, CA 93943-5000

8. Prof. D. L. Gardner, Code PH/Gd   1
Physics Department
Naval Postgraduate School
Monterey, CA 93943-5000

9. Prof. R. M. Keolian, Code PH/Kn   1
Physics Department
Naval Postgraduate School
Monterey, CA 93943-5000

10. LT Gregory J. Reid   4
c/o 8 Kadigal Place
Beacon Hill, 2085
Australia

11. MOD, DSTO   1
    Attention: Dr. Eric Magi
                88 Labs
                P.O. Box 1500
                Salisbury, South Australia 5108

12. ASTO
Program Executive Office
    ATTN: G. Kamailakis, Code ASTOG   1
                CDR J. Polcari, Code 06KR   1
Washington, DC 20362-5169

13. Commanding Officer
Naval Research Laboratory
    ATTN: Dr. A. Dandridge, Code 6574   1
4555 Overlook Ave.
Washington, DC 20375-5000

14. Commanding Officer
Naval Undersea Warfare Center
    ATTN: R. Maple, Code 2133   1
                B. Buehler, Code 2191   1
                B. Blakely, Code 2141   1
                A. Deus, Code 2141   1
New London, CT 06320-5594

15. Commanding Officer
    Naval Undersea Warfare Center
    ATTN: LCDR John Serocki, Code 422   1
    Operational Test and Evaluation Force
    7970 Diven St.
    Norfolk, VA 23505

16. Litton Guidance and Control Systems
    ATTN: Mr. D. Myer   1
    Advanced Projects Group
    5500 Canoga Ave.
    Woodland Hills, CA 91367-6698

17. Commanding Officer   1
    NRaD
    ATTN: Mr. R. Brininstool, Code 946
    San Diego, CA 91367-6698

18. Alliant TechSystems   1
    ATTN: E. Rissberger
    6500 Harbour Heights Parkway
    Evertt, WA 98204-8899

19. Commanding Officer   1
    Space and Naval Warfare Systems Command
    PMW 180
    ATTN: CAPT Hatcher
    Washington, DC 20363-51007

20. Brown University   1
    Professor T.F. Morse
    Lightwave Technology Lab 4
    Division of Engineering
    Box D
    182 Hope St.
    Providence, RI 02912